METAMORPHISM AND FLUID-ROCK INTERACTION IN THE ALTA, UTAH CONTACT AUREOLE: IDENTIFICATION OF FORSTERITE REACTION PATHWAYS, EVALUATION OF REACTION OVERSTEPPING, AND TRACE ELEMENT CHARACTERIZATION

by

Patrick C. Loury

A thesis submitted to the faculty of
The University of Utah
in partial fulfillment of the requirements for the degree of

Master of Science

in

Geology

Department of Geology and Geophysics

The University of Utah

August 2015

The University of Utah Graduate School

STATEMENT OF THESIS APPROVAL

The thesis of **Patrick C. Loury**

has been approved by the following supervisory committee members:

John R. Bowman	, Chair	**1/14/2014** Date Approved
Erich U. Petersen	, Member	**6/24/2013** Date Approved
Diego P. Fernandez	, Member	**6/24/2013** Date Approved

and by **John M. Bartley** , Chair/Dean of

the Department/College/School of **Geology and Geophysics**

and by David B. Kieda, Dean of The Graduate School.

ABSTRACT

Forsterite (Fo) is developed extensively in dolomite marbles in the Alta, Utah contact aureole. Through the Fo zone and much of the periclase (Per) zone, the number of forsterite (Fo) crystals/mol Fo increases and the average Fo grain size decreases as the Alta Stock intrusive contact is approached. Excluding the innermost Per zone, $\Delta^{18}O$ (Carbonate-Fo) values increasingly depart from equilibrium values with increased metamorphic grade. These textural and oxygen isotope trends reflect progressively greater reaction affinity (A_r) driven by the combined effects of elevated temperatures, faster heating rates, and decreasing $X(CO_2)$ in infiltrating fluids toward the igneous contact.

Significant variation exists in the number of Fo crystals/mol Fo, $\delta^{18}O$ (carbonate), and $\Delta^{18}O$ (Carbonate-Fo) between strata within individual outcrops at several locations. At most sites, the number of Fo crystals/mol Fo and $\delta^{18}O$ value of carbonate matrix are negatively correlated, suggesting that increased infiltration of low $X(CO_2)$ and low $\delta^{18}O$ fluid drives A_r higher. In the outer Fo zone, neither $\Delta^{18}O$ nor $\delta^{18}O$ (carbonate) correlate with Fo crystals/mol Fo values because infiltrating fluids have largely exchanged isotopically with the marble in this part of the aureole.

A suite of trace elements were analyzed in samples from the Alta Stock, skarns, Alta aureole marbles, and the carbonate protolith. To detect concentration anomalies element concentrations are normalized to Al, which is demonstrated to be immobile in

the marbles of the aureole. Positive concentration anomalies are documented for Ba, Cu, Pb, Zn, Sr, Rb, and K to varying distances from the intrusive contact. Fe and Mn anomalies are absent, suggesting that crystallizing skarn minerals effectively exhausted the Fe and Mn supply of infiltrating fluids before they reached significant distance in the aureole.

Within the zone of $^{18}O/^{16}O$ depletion (< 400 m from the igneous contact), negative correlations are observed between concentrations and $\delta^{18}O$ (carbonate) for Cu, Pb, Zn, and Ba, suggesting a link between elevated fluid flux and the addition of these elements to the carbonate protolith. These results demonstrate that integrated isotopic and trace element data have potential applications in the exploration for skarn deposits and other intrusion-centered, carbonate-hosted metallic deposits.

TABLE OF CONTENTS

LIST OF TABLES

LIST OF FIGURES

ACKNOWLEDGEMENTS

I would like to thank John Bowman for sharing his advice, expertise, and enthusiasm throughout the entirety of this study; without his help this project would not have been possible. Many thanks are also due to Erich Petersen for his help in collecting and interpreting QEMSCAN data and for his support for the Society of Economic Geologists student chapter, which provided me numerous learning opportunities and the chance to meet some truly fantastic people in the process. Diego Fernandez was instrumental in the ICP-MS data interpretation, and his help has greatly increased my ability to think critically about analytical processes and data quality. I would like to thank John Valley and Mike Spicuzza at the University of Wisconsin for their assistance in generating oxygen isotope data as well. I am incredibly grateful for the support provided through the Society of Economic Geologists Graduate Student Fellowship Program, and I would like to thank Borden Putnam and Stephen J. Piercey of the SEG Foundation and Rael Lipson of Gold Fields Exploration for the support provided through the Fellowship. Their support and enthusiasm for students and their willingness to share their experience is truly unmatched and greatly appreciated. I would also like to thank Quintin Sahratian for his help in sample preparation and for providing the best polished thin sections that I have ever seen. Finally, I would like to thank my family and friends for providing love and support throughout the entire process.

CHAPTER 1

IDENTIFICATION OF FORSTERITE REACTION PATHWAYS AND EVALUATION OF REACTION OVERSTEPPING

1.1 Introduction

The product and reactant minerals (forsterite[Fo], diopside[Di], calcite[Cal], dolomite[Dol]) present within siliceous dolomite strata in contact aureoles generally maintain relatively simple chemical compositions, and have been well-characterized in terms of their thermodynamic properties. In addition, the reactions responsible for the formation of forsterite and other minerals in carbonate rock protoliths during metamorphism are functions of fluid composition (e.g., $X[CO_2]$) and are therefore sensitive to fluid infiltration. As a result, these minerals have developed as important standards for the study of the mechanisms driving metamorphic reactions and the kinetics of these reactions.

Fo-forming reactions are of particular interest because a wide variety of forsterite textures are often produced and stable isotopes are distributed between products and reactants differently as a result of varying fluid compositions and thermal conditions in these systems (Roselle et al., 1997; Müller et al., 2004; Ferry, et al., 2011). A number of recent studies have suggested that Fo can be produced through several different reaction pathways, depending on pore fluid composition, time integrated fluid flux, thermal

gradients, and timescales of heating. For example, the presence of coexisting Tr + Dol +Fo + Cal or Di + Dol + Fo + Cal mineral assemblages in the Ballachulish, Ritter Range Pendant, Monzoni, and Predazzo aureoles provides direct evidence that Fo and Cal are produced from the isochemical (excluding volatiles) reaction of Dol + Tremolite (Tr) or Dol + Di:

$$11\text{Dol} + \text{Tr} = 8\text{Fo} + 13\text{Cal} + 9\text{CO}_2 + \text{H}_2\text{O} \quad (1\text{-}1)$$

$$3\text{Dol} + \text{Di} = 2\text{Fo} + 4\text{Cal} + 2\text{CO}_2 \quad (1\text{-}2)$$

in these aureoles (Ferry, 1996, Ferry et al. 1998, 2002). Furthermore, calcite-dolomite thermometry results for rocks from these locations often fall within the stability range of reactions 1-1 and 1-2, suggesting that these reactions proceed under near-equilibrium conditions (Ferry et al., 2011).

However, other studies have suggested that Fo-forming reactions may be significantly overstepped in situations were metamorphism occurs under steep thermal gradients and short timescales of heating, with textural and isotopic evidence being cited to support this interpretation. Roselle et al. (1997) report that in the Ubehebe Peak aureole, the number of Fo crystals increases and the size of these crystals decrease as the intrusive contact is approached. The authors interpret this trend to indicate progressive reaction overstepping with increased temperature because crystal nucleation rates increase at a greater rate with increased temperature than do growth rates (Ridley and Thompson, 1986).

Müller et al. (2004) measured $\delta^{18}O$ values of Fo, Cal, and Dol in marble samples

from the Ubehebe Peak aureole, California. They found that Fo and Cal maintain isotopic exchange equilibrium with one another at the estimated temperature of contact metamorphism (600-620 °C; Roselle et al., 1997), but none of the 52 dolomite analyses yield a $\delta^{18}O$ value consistent with equilibrium calcite-dolomite fractionation. Thus the reaction products are out of oxygen isotope exchange equilibrium with reactant dolomite. Müller et al. (2004) note that reaction 1-1 results from the combined effects of three local reactions (1-1i through 1-1iii) involving dissolution and precipitation where gb indicates species transport through grain-boundary diffusion:

$$0.021Tr + 0.064Cal + 0.15CO_2 = 0.105Dol + 0.02H_2O + 0.171SiO_2^{gb} \quad (1\text{-}1i)$$

$$0.342Dol = 0.342Cal + 0.342MgO^{gb} + 0.342CO_2 \quad (1\text{-}1ii)$$

$$0.342MgO^{gb} + 0.171SiO_2^{gb} = 0.171Fo \quad (1\text{-}1iii)$$

One of these reactions (1-1i) produces Dol. This newly formed dolomite should form in oxygen isotope exchange equilibrium with the other reaction products (Fo + Cal). Because Dol is not in oxygen isotope exchange equilibrium with Fo and Cal, the authors conclude that Fo in the Ubehebe Peak aureole formed through metastable reaction 1-3:

$$2Dol + SiO_2 = 2Cal + CO_2 \quad (1\text{-}3)$$

In reaction 1-3, Fo and Cal are produced directly from Dol and SiO_2 supplied either in

aqueous form through infiltrating fluids or present *in situ* as quartz within the original, unmetamorphosed dolomite strata (Müller, et al., 2004; see also Ferry, et al., 2011).

Ferry et al. (2011) measured oxygen isotope compositions of texturally coexisting Cal, Dol, and Fo by ion microprobe analyses in four marble samples from the Twin Lakes Pendant, California and Beinn an Dubhaich aureole, Scotland. Previous work (Davis and Ferry, 1993; Ferry and Rumble, 1997) indicated that these samples had experienced infiltration-driven reaction 1-3. Ferry et al. (2011) measured variable extents of oxygen isotope disequilibrium among Fo, Cal, and Dol between the four samples. Increasing oxygen isotope exchange disequilibrium (smaller $\Delta^{18}O_{Cal\text{-}Fo}$ fractionation factors) correlated with lower $X(CO_2)$ of infiltrating fluids, higher Fo crystal number density, smaller average Fo grain size, and more equigranular Fo crystal morphology. These textural changes and increasing extent of oxygen isotope disequilibrium were interpreted to reflect increased overstepping of the Fo-producing reaction. Such overstepping, or reaction affinity (A_r), can be produced by increases in temperature or decreases in $X(CO_2)$ in the infiltrating fluid. Ferry et al. (2011) proposed that variations in A_r between these four samples are explained by the variations in $X(CO_2)$ of the infiltrating fluid.

It is possible that Fo in the Alta Stock contact aureole may be similarly produced from kinetic overstepping of the stable Fo-forming reaction 1-1, or perhaps from a metastable reaction pathway (reaction 1-3) as well, and these possibilities have yet to be tested. The studies of Roselle et al. (1997), Müller, et al. (2004), and Ferry et al. (2011) suggest that there are textural and oxygen isotope indicators for the extent of reaction overstepping, including increasing numbers of Fo crystals per mole Fo, decreasing average Fo grain size, and increasingly large departures from oxygen isotope exchange

equilibrium between and among reactant and product phases. As a result, the primary objective of this study is to evaluate reaction overstepping in the Alta aureole through an integrated mineralogical, textural, mineral mode, and oxygen isotope study of the forsterite and periclase zones. The results should therefore provide further insight into reaction mechanisms and processes of fluid-rock interaction responsible for the contact metamorphism of siliceous dolomite rocks.

In order to evaluate the textural characteristics of inner aureole samples, Fo modes, crystal size distribution, average crystal size, and number of Fo crystals/mol Fo were measured for each sample by quantitative evaluation of minerals by scanning electron microscopy (QEMSCAN) at the University of Utah. Forsterite was separated from this same suite of marbles and the $\delta^{18}O$ values of Fo, Cal, and Dol were measured. Measured $\Delta^{18}O_{Cal\text{-}Fo}$ and $\Delta^{18}O_{Dol\text{-}Fo}$ factors were compared with the equilibrium oxygen isotope fractionation values at temperatures determined for the inner aureole from calcite-dolomite thermometry (Cook and Bowman, 1994). If the measured differences in $\delta^{18}O$ are inconsistent with the expected equilibrium fractionation values at the temperatures produced in the inner Alta aureole, it can reasonably be assumed that the minerals did not form through equilibrium processes, but rather through significant overstepping of the forsterite-forming reaction. The resulting data will therefore provide important information regarding the reaction pathways responsible for forsterite development and the significance of reaction overstepping in the development of forsterite in the Alta aureole. On a broad scale, the findings presented in this study will provide insights regarding the roles of reaction kinetics in infiltration-driven metamorphism of carbonate rocks and the nature of fluid infiltration and mechanisms of fluid-rock interaction in the shallow crust.

1.2 Geologic Setting and Contact Metamorphism

1.2.1 The Alta Stock

The 34 ± 1.5 Ma Alta Stock is an approximately 10 km^2 granodioritic intrusion (Figure 1-1), and is one of several mid-Tertiary stocks in the Wasatch Range of central Utah, including the nearby Little Cottonwood quartz monzonite (30 ± 0.5 Ma) and the 35.5 ± 1.5 Ma Clayton Peak granodiorite (Vogel et al., 2001). In a detailed mineralogical and textural study of these stocks, Hanson (1995) identified two major groups that generally define an east-trending belt of intrusive rocks, with the western group (Alta, Clayton Peak, and Little Cottonwood stocks) being identified by their felsic composition and phaneritic texture, while the eastern group stocks (Flagstaff Mountain, Glencoe, Ontario, Mayflower, Pine Creek, and Valeo) are more mafic and porphyritic. The trend is coincident with a suture between the Archean Wyoming Craton and the Proterozoic Yavapai province known as the Uinta arch, and it has been suggested that the suture may have provided some degree of spatial control for these intrusions (John, 1989). The stocks become progressively younger and more deeply exposed from east to west, and magmatism is eventually expressed to the east of Park City, Utah by the Keetley Volcanic field (John, 1989).

The Alta Stock is dominated by quartz and plagioclase feldspar, although significant amounts of potassium feldspar, biotite, and hornblende are also present, and apatite, titanite, magnetite, and zircon occur as accessory minerals (Wilson, 1961; Hanson, 1995). Wilson (1961) identified two major phases of the stock (Figure 1-1) that are differentiated based on textural differences, with the border phase being intruded by the more porphyritic central phase. Johnson (2009) noted that the contact between the phases is more clearly defined in the southeastern portion of the Alta Stock, and tends to

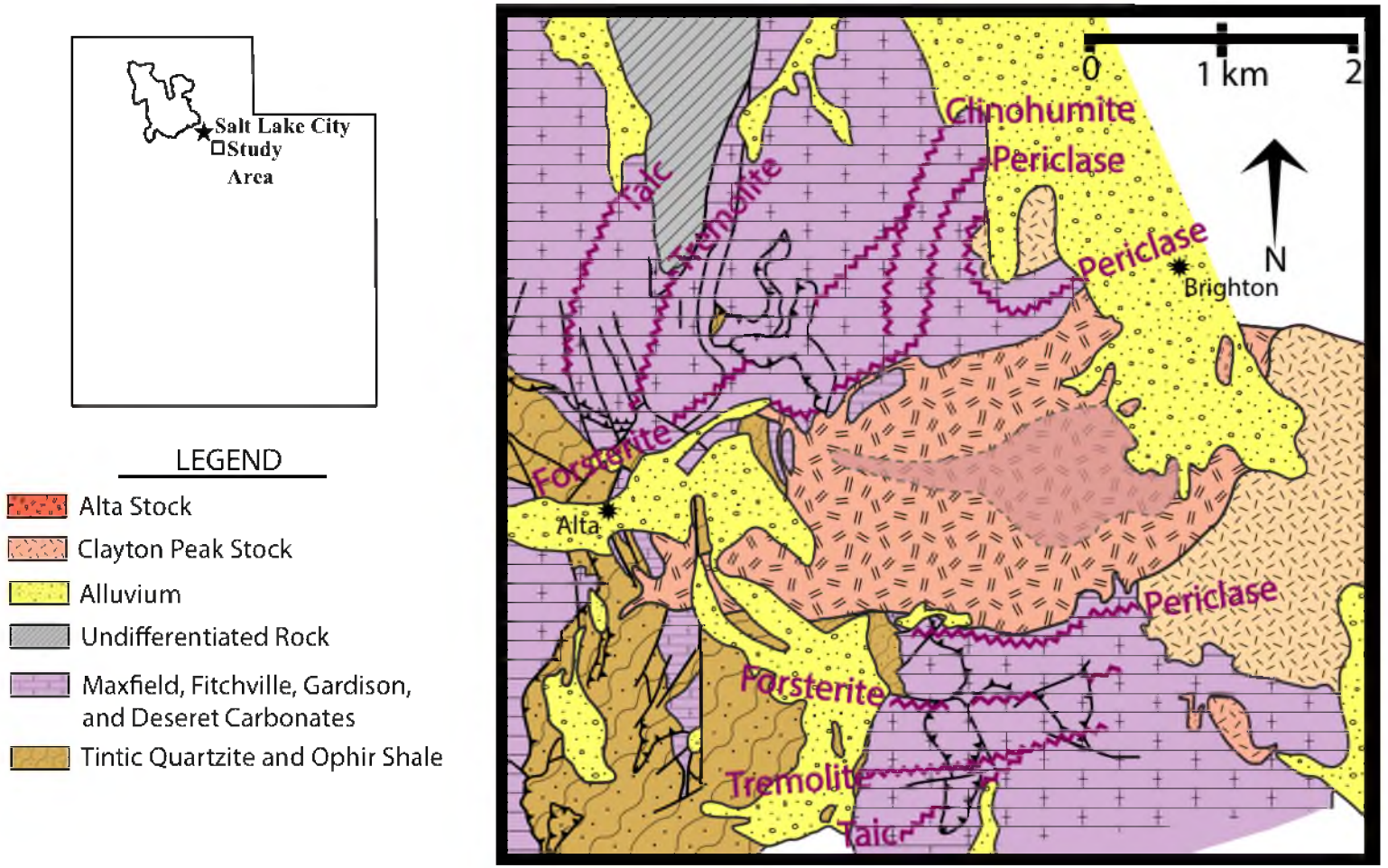

Figure 1-1. General geology of the Alta Stock and aureole. Study area location and simplified geologic map of the Alta Stock and contact aureole. The contact between the central and border phases of the Alta Stock is also denoted with a dashed line. Modified from Baker et al. (1996), Moore and Kerrick (1976), and Chadwell (2005).

be more gradational in the north and west. Prior to emplacement of the Alta Stock, the Cambrian and Mississippian strata in the area were subjected to thrusting (the Alta Grizzly thrust zone) associated with the Sevier orogeny, which has placed the Cambrian Maxfield Formation and younger Paleozoic strata over the Mississippian Deseret and Gardison Formations (Baker et al., 1966). Cenozoic faulting has resulted in an eastward tilting of the Alta Stock, causing deeper exposures in the southwestern portion when compared to the eastern region, and the westernmost portion of the stock is cut by the Silver Fork fault (Crittenden, 1965; John, 1989).

The depth of emplacement of the Alta Stock has been estimated to be 3.5-7 km (1.0-2.2 Kb) based on stratigraphic reconstructions and contact metamorphic mineralogy (Wilson, 1961; Kemp, 1985). However, significant debate exists about the mechanisms and timespan responsible for emplacement of the stock. Cook et al. (1997) assumed an essentially instantaneous emplacement of the stock for their heat and mass ($^{18}O/^{16}O$) transport modeling of the thermal structure and $^{18}O/^{16}O$ depletion patterns in the Alta aureole. Independent of any assumptions of mode and timespan of stock emplacement, the observed locations of the periclase and tremolite isograds and width of the $^{18}O/^{16}O$ depletion zone constrain total heat and fluid flux into the aureole. If prograde metamorphism and fluid infiltration are contemporaneous, the coupled heat and oxygen isotope constraints require advective heat and fluid flow of relatively short duration (5,000 to 10,000 years), which implies but does not require a similarly short timescale of pluton emplacement. The authors further note if the observed mass of the Alta Stock is the sole source of heat for the aureole, the lateral width of the aureole (~2 km) would be much smaller than observed if emplacement of the stock occurred incrementally over a large (~10^6) time scale.

Bartley et al. (2007), however, propose that the Alta Stock was indeed emplaced incrementally as a series of dikes over a long (~10^6 year) time scale. The Alta stock was most likely emplaced under conditions of extensional tectonics (Vogel et al., 2001). If dilation is the primary space-making mechanism, the size of the Alta Stock (~1km radius) coupled with time-averaged extension rates of roughly 1mm/yr, typical for continental extension (Vogel et al., 2001), would require an approximately 10^6 year timescale for emplacement. Evidence cited by Bartley et al. (2008) to support this interpretation also includes the tabular shape of the stock, its spatial association with parallel dike swarms, and wall-parallel lithologic sheeting within the stock. Additionally, features such as fractured feldspars, kinked biotite grains, and offset dikes in the stock support its syn-kinematic emplacement, compatible with the hypothesis of incremental emplacement. In order to explain the large lateral extent of the metamorphic aureole, Bartley et al. (2008) proposed additional heat input from another, deeper intrusive body, and suggest that the Alta Stock may indeed be much larger than the exposed portion. However, this is problematic in that there is little surface expression of this additional intrusive material. Available topographic relief indicates that the southern igneous contact is subvertical (Cook and Bowman, 1994) and metamorphic isograds and zones are subparallel with the southern igneous contact, with the exception of the talc isograd (Moore and Kerrick, 1976; Cook and Bowman, 2000). These observations do not support a lateral expansion of the Alta Stock with increased depth beneath the southern aureole.

1.2.2 Contact Metamorphism and Fluid-Rock Interaction

Country rocks surrounding the Alta Stock (Figure 1-1) range from Precambrian to Mississippian in age, and are dominated by quartzites (Precambrian Big Cottonwood and

Cambrian Tintic Formations) and carbonates (Cambrian Maxfield and Mississippian Fitchville, Deseret, and Gardison Formations), with one pelitic unit (Cambrian Ophir Formation) present immediately below the carbonate sequence (Baker et al., 1966). The carbonate strata primarily consist of siliceous dolomites that contain either massive dolomite (Dol) and only sparsely disseminated quartz, or chert nodules in a massive Dol matrix (Moore and Kerrick, 1976). Unmetamorphosed massive dolomite strata generally contain relatively minor (<10% each) quartz (Qz) and calcite (Cal) (Cook and Bowman, 2000). These strata have been subjected to contact metamorphism resulting from heat input and fluid infiltration associated with the emplacement of the Alta Stock, which has produced a prograde assemblage (Figure 1-1) defined by the appearance of the index minerals talc (Tlc), tremolite (Tr), forsterite (Fo), and periclase (Per) as the stock contact is approached (Moore and Kerrick, 1976). Contact metamorphic effects, as reflected by the appearance of metamorphic minerals, extend ~2km from the southern igneous contact. As this study focuses on the development of Fo in the inner aureole, only the Fo and Per zones will be described.

The appearance of forsterite in the Alta aureole has been ascribed to the breakdown of Dol and tremolite to form Fo and Cal (reaction 1-1), which is supported by the observed progression from the assemblage Tr + Dol + Cal to the assemblage Fo + Cal + Dol moving inward toward the periclase isograd (Moore and Kerrick, 1976; Cook and Bowman, 2000). The rarity of the univariant assemblage of Tr + Dol + Fo + Cal in marbles of the forsterite zone reflects the general absence of fluid buffering by the Fo marbles because of significant infiltration of H_2O-rich fluids that drive the Fo-forming reaction (Cook and Bowman, 2000). The general absence of tremolite throughout the forsterite zone of the Alta aureole indicates either that reaction 1-1 proceeded to

completion within the forsterite zone, or that Fo was formed through reaction 1-3. The distal portions of the forsterite zone tend to show larger, more tabular Fo grains and a greater abundance of nonreacted Dol than the inner forsterite zone, which is characterized by smaller, more equant forsterite and a substantial decrease in Dol content (Chadwell, 2005).

The periclase zone is characterized by the prograde assemblage Per + Cal within massive dolomite strata, and the periclase isograd occurs at an average distance of 200 m from the stock contact in marbles below the Alta-Grizzly thrust. Dolomite-bearing strata above the Alta-Grizzly thrust in the southern aureole do not contain Per, even within several meters of the igneous contact. Reaction 1-4 is responsible for producing periclase; this reaction has gone to completion, and no primary Dol remains in these periclase marbles (Cook and Bowman, 2000). The periclase is completely replaced by pseudomorphs of brucite produced by reaction 1-5 or through retrograde reaction (1-6) at the Per-Brc-Cal-Dol invariant point where X_{IP} is the $X(CO_2)$ value of the fluid at this invariant point:

$$Dol = Per + Cal + CO_2 \quad (1\text{-}4)$$

$$Per + H_2O = Brc \quad (1\text{-}5)$$

$$Per + X_{IP}Cc + X_{IP}CO_2 + (1\text{-}X_{IP})H_2O \rightarrow (1\text{-}X_{IP})Brc + X_{IP}Do \quad (1\text{-}6)$$

In some periclase-zone samples, Dol is preferentially associated with brucite

pseudomorphs, suggesting that this Dol was formed as a result of a retrograde reaction such as 1-6. Forsterite is generally not present with periclase; rather, Per-bearing marbles contain clinohumite (Chm) which is interpreted to form by the reaction 1-7 (Cook and Bowman, 2000):

$$Dol + 4Fo + H_2O + HF = Chm + Cal + CO_2 \quad (1\text{-}7)$$

However, throughout the Per zone, Fo occurs in calcite marbles lacking periclase or primary dolomite.

Small garnet-pyroxene skarns are developed in the south aureole at the main igneous contact, on margins of granodiorite sills intruded into the marble wallrocks, and less commonly along subvertical fractures in the Per zone marbles (Cook, 1982). Detailed relationships in outcrop (Root et al., 2012) show that the sill tips are mantled by garnet-pyroxene skarns, which in turn are mantled by marble with abundant ludwigite, an Fe-Mg borate mineral. Ludwigite-bearing periclase marbles extend beyond these sill/skarn tips into the wallrocks. These relationships indicate that boron-bearing, H_2O-rich hydrothermal fluids flow from the intrusion (and sills) into the marble wallrocks, initially forming skarn, then precipitating B in the form of ludwigite, and then continuing to flow along marble strata to form periclase marbles.

Cook and Bowman (1994) utilized calcite-dolomite solvus thermometry to define the thermal structure of the aureole. The results indicated that temperatures increase from approximately 400 °C in the talc zone up to ~625 °C at the igneous contact. Cook and Bowman (1994) fitted a second order polynomial equation to this calcite-dolomite solvus thermometry data, which allows temperature to be determined at a given distance from

the igneous contact:

$$T(°C) = 626.43 - 0.329442x + 0.0001354x^2 \quad (1\text{-}8)$$

where x is the distance (m) from the igneous contact with the Alta Stock. This polynomial fit yields temperatures of < 420, 420 ± 50, 470 ± 50, 580 ± 25, and 625 ± 25 °C for the Tlc, Tr, Fo, and Per isograds, and igneous contact, respectively. Coupled with phase equilibria, these calcite-dolomite thermometry results constrain the prograde T-$X(CO_2)$ path for metamorphism of the marble as a path of increasingly water rich fluids at higher metamorphic grades, which Cook and Bowman (2000) show is consistent with down-temperature infiltration of H_2O-rich fluids into the marble wallrocks.

Bowman et al. (1994) documented $^{18}O/^{16}O$ depletion in the marbles of the south aureole out to 300-400 m from the intrusive contact, indicating that these marbles have experienced significant infiltration of low $\delta^{18}O$ fluids. The pattern of $^{18}O/^{16}O$ depletion in the aureole defines a dispersed oxygen isotope exchange front centered at ~350 m from the igneous contact; the geometry of this exchange front requires that fluid flow was outward from the intrusion and down-temperature (Bowman et al., 1994). Detailed patterns of $^{18}O/^{16}O$ depletion at the outcrop scale and across bedding boundaries suggest that flow was largely bedding controlled (Bowman et al., 1994).

$^{18}O/^{16}O$ depletion is restricted to marbles beneath the Alta-Grizzly thrust, suggesting a horizontal permeability barrier above the thrust and Alta Stock (Cook et al., 1997). Cook et al. (1997) demonstrate that heat and mass ($^{18}O/^{16}O$) transport models with such horizontal permeability barriers force fluid flow and heat transfer laterally away from the upper flanks of the stock into the marble wallrocks and are capable of

reproducing the observed thermal and $\delta^{18}O$ profiles in the southern aureole. The simulation of the observed temperature profile by these models requires a permeability of at least 2 x $10^{-16}m^2$ for the infiltrated marbles (Cook et al., 1997). The authors demonstrate that fluid flow on timescales of about 5,000 to 6,000 years and time integrated fluid fluxes of approximately 3,000 m^3/m^2 are capable of simultaneously producing the observed width of the periclase zone, the temperatures in the inner aureole, and the observed advance of the oxygen isotope exchange front into the south aureole.

1.3 Methods

1.3.1 Sample Selection and Thin Section Preparation

A suite of forsterite-bearing samples from the forsterite (Fo) and periclase (Per) zones of the Alta aureole was selected from existing sample collections made by Steve Cook and Lori Chadwell, former graduate students, and Dr. John R. Bowman (Figure 1-2). In addition, a stratigraphic section in the inner Fo zone (site 11-III) was measured and described, and a detailed suite of samples was collected at that location (Figure 1-3). Samples were selected in part to form a sampling traverse with roughly equal sample spacing from the outermost forsterite zone to the igneous contact. Because Fo abundance and texture vary significantly throughout the inner aureole, this sampling strategy is important in that it ensures that systematic variations in texture or abundance with changing distance (i.e., temperature) will be accurately identified if such variations exist.

Since weathering, alteration, and veining are often indications of interaction between the original marble and retrograde, potentially $^{18}O/^{16}O$-depleted metamorphic fluids, special care was taken in every stage of sample selection to avoid areas that displayed these characteristics. It is likely that the original oxygen isotope composition

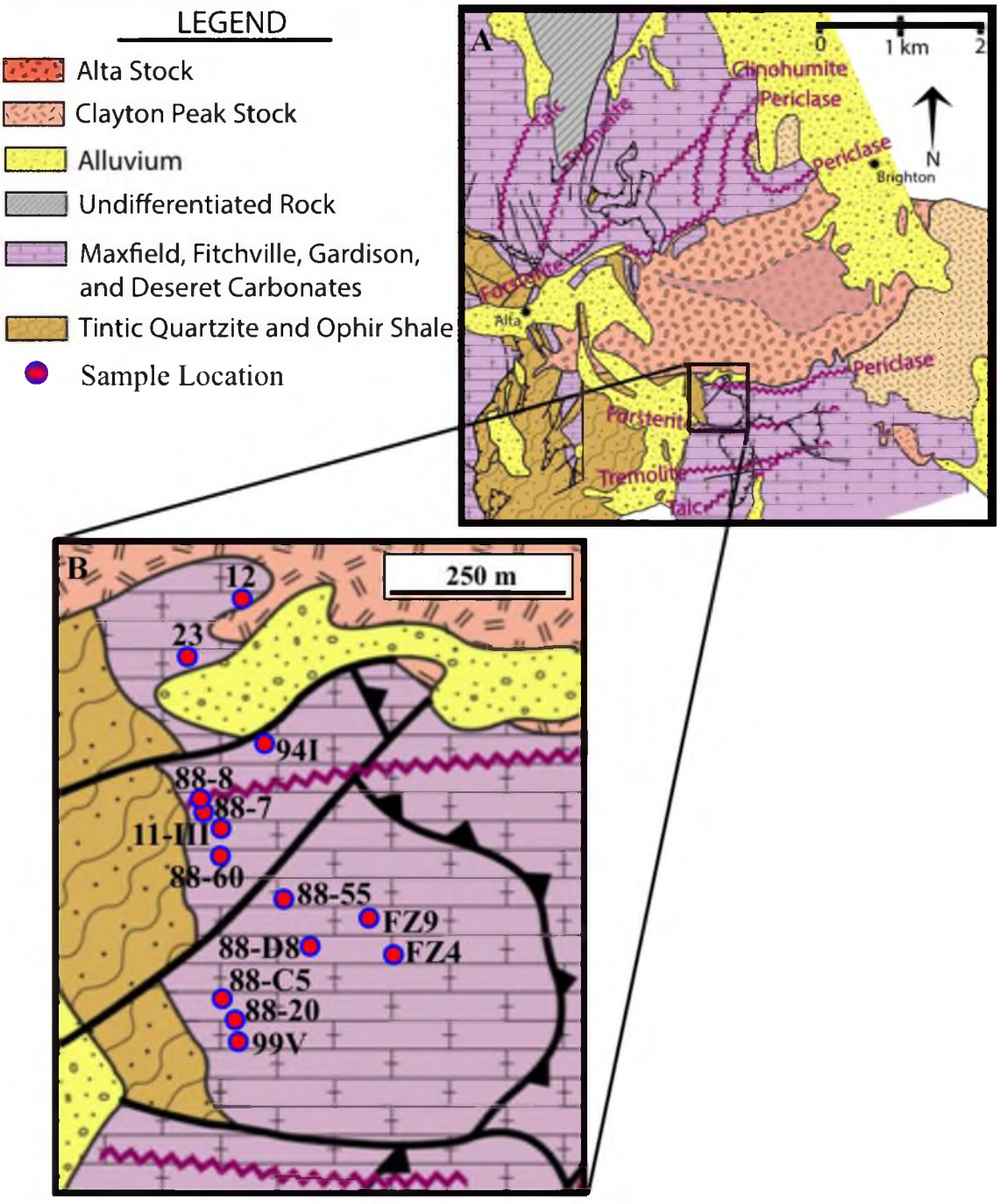

Figure 1-2. Forsterite sample locations. **(A)** Simplified geologic map of the Alta Stock and contact aureole. **(B)** Detailed map of the forsterite and periclase zones with locations of sample sites from which textural and oxygen isotope data were collected. Modified from Baker et al. (1966) and Chadwell (2005).

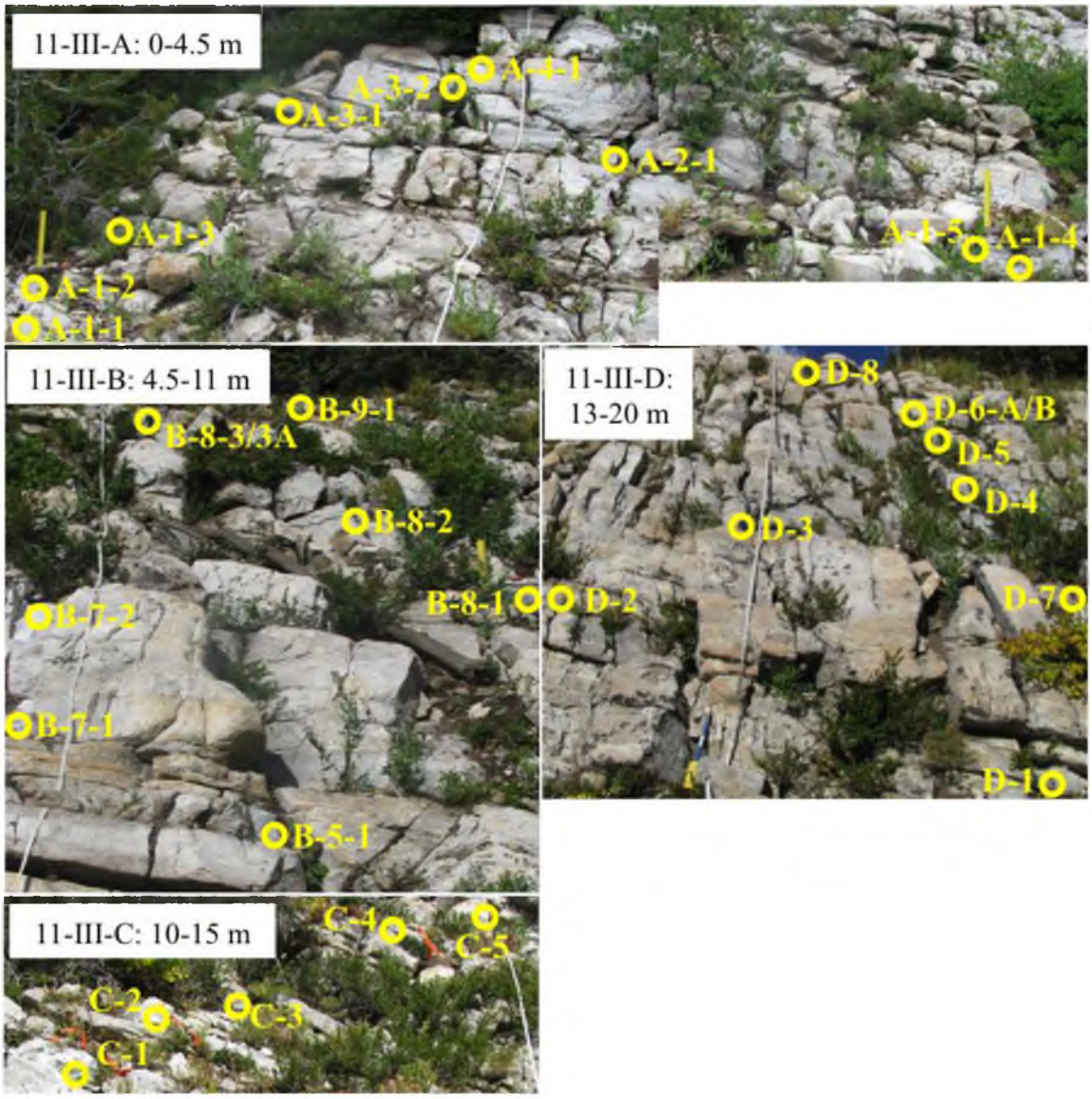

Figure 1-3. Outcrop photographs showing individual segments of Traverse 11-III (A, B, C, D) and their corresponding ranges in stratigraphic height. All stratigraphic height measurements are in reference to the stratigraphically lowest sample (A-1-1 = 0 m). Sample locations are marked by yellow circles, with the corresponding sample numbers identified in yellow text.

of the metamorphic minerals (particularly calcite) would not be preserved in areas affected by these processes (Bowman et al., 2009), and the inclusion of such samples would therefore affect the results and interpretations presented in this study. Slabs oriented normal to original stratigraphic layering were cut from each sample. Each slab was evaluated in terms of its physical characteristics, including the degree of alteration, weathering, veining, grain size variations, and mineral abundances. If heterogeneities existed with respect to these characteristics, each individual domain was treated independently in all analytical procedures.

Billetts were prepared from each slab, with texturally or mineralogically distinct domains being represented either by a separate billett or by a single billett spanning the boundary between adjacent domains. Billetts were stained with alizarin red to distinguish calcite from dolomite, and polished thin sections were prepared with staining preserved. Each domain was inspected in thin sections with a petrographic microscope to determine mineralogy, to estimate the abundance of Fo, Cal, and Dol, and to evaluate the extent of retrograde alteration. These characteristics are described for all samples in Table 1-1.

1.3.2 Textural Characterization of Forsterite

Samples were selected for quantitative textural analysis of forsterite to represent a wide range of forsterite abundance and overall grain size of the marble samples. Mineral modes, average Fo grain area, average Fo long axis, and the number of Fo crystals (N_A) were measured in representative areas (approximately 1 cm^2) from each thin section using QEMSCAN analysis. Appendix A provides a detailed description of QEMSCAN procedures and data. In order to account for variations in the modal abundance of forsterite between samples (variations in bulk composition), the number of

Table 1-1. Sample locations and descriptions

Sample	Zone[1]	Distance from Intrusion (m)	Mineralogy[1]	Alteration[2]	Matrix Grain Size[3]
12-1b	Per	10	Cal+Fo	Moderate	Intermediate
12-2	Per	10	Cal+Chm (?)	Moderate	Coarse
23-B(l)	Per	25	Cal+Dol+Fo	Minor	Fine
23-B(u)	Per	25	Cal+Dol+Fo	Minor	Fine
94I-9-2-a	Per	175	Cal+Fo+Py	Moderate	Coarse
94I-9-2-b	Per	175	Cal+Fo	Moderate	Coarse
88-8	Fo	220	(Cal>Dol)+Fo	Moderate	Coarse
88-7	Fo	230	Cal+Fo	Moderate	Coarse
A-1-1	Fo	300	Cal+Fo	Minor	Fine
A-1-4	Fo	300	Cal+Fo	Minor	Fine
A-3-1	Fo	300	Cal+Fo	Minor	Intermediate
A-4-1	Fo	300	Cal+Fo+Py	Minor	Intermediate
B-7-1 coarse	Fo	300	Cal+Fo	Moderate	Coarse
B-7-1 fine	Fo	300	Cal+Fo	Minor	Fine
B-8-1 lower	Fo	300	Cal+Fo	Moderate	Fine
B-8-1 mid	Fo	300	Cal+Fo+Py	Moderate	Fine
B-8-3A	Fo	300	Cal+Fo	Minor	Fine
D-6-B coarse	Fo	300	Cal+Fo+Phl	Minor	Coarse
D-6-B fine	Fo	300	Cal+Fo+Phl	Minor	Fine
88-60	Fo	315	(Cal>Dol)+Fo	Moderate	Coarse
88-55	Fo	370	Cal+Fo	Moderate	Intermediate
88-D8	Fo	455	Dol+Fo	Moderate	Intermediate
FZ9-18	Fo	455	(Dol>Cal)+Fo	Minor	Fine
FZ4-4a	Fo	475	Dol+Fo	Minor	Fine
88-C5	Fo	550	(Dol>Cal)+Fo	Minor	Intermediate
88-20	Fo	570	Dol+Cal+Fo+Py	Minor	Fine
99V-12c	Fo	615	Dol+Fo	Moderate	Fine
99V-3	Fo	615	(Dol>Cal)+Fo	Minor	Coarse
99V-5a	Fo	615	Dol+Cal+Fo	Minor	Coarse

[1]Cal: Calcite; Chm: Clinohumite; Dol: Dolomite; Fo: Forsterite; Per: Periclase; Phl: phlogopite; Py: pyrite

[2]Retrograde alteration (e.g., the presence of serpentinized olivine and turbid calcite (Bowman et al., 2009)) estimated qualitatively as minor, moderate, significant, or severe.

[3]Grain size of the carbonate matrix of the marble samples estimated qualitatively as fine, intermediate, or coarse.

Fo crystals was normalized to the moles of Fo present in the sample using procedures described in Appendix A.

1.3.3 Stable Isotope Analyses

Millimeter-scale samples of carbonate matrix were collected using a dental drill from each slab from areas in which thin section analysis showed were free of retrograde alteration. Approximately 100 μg aliquots from each powdered sample were placed in sample vials, which were flushed with Ultra High Purity (UHP) Helium for approximately 5 minutes at 50 ml/min He to remove atmospheric CO_2 before analysis. The samples were then reacted with anhydrous phosphoric acid (H_3PO_4) for 1 hour at 75 °C to generate CO_2 gas for mass spectrometric analysis. The $\delta^{13}C$ and $\delta^{18}O$ values of these samples were measured using the Finnigan-MAT Gas Bench II interface coupled with a Delta Plus Isotope Ratio Mass Spectrometer (IRMS) in the University of Utah's Stable Isotope Ratio Facility for Environmental Research (SIRFER). A detailed description of the Gas Bench II interface analysis method for carbonate samples is provided by Breitenbach and Bernasconi (2011). NBS19, NBS18, LSVEC, and Carrara marble were used as standards for these isotope analyses.

A suite of samples was selected to prepare Fo separates for oxygen isotope analysis. These samples were selected to define a systematic traverse across both the Fo and Per zones, and to include a wide range of Fo textures and abundances. Forsterite grains were separated from the carbonate matrix by acid (1M HCl) dissolution in order to preserve the original shapes and size distribution of the Fo crystals. The insoluble material (mostly Fo with minor but variable amounts of sulfide and phlogopite) was cleaned and sieved into five different crystal size fractions (>853 μm, 853-420 μm, 420-

178 μm, 178-106 μm, and 106-75 μm). Each size fraction was then subjected to an HF treatment to remove serpentine (detailed in Appendix B). Laser fluorination techniques (Sharp, 1990; Crowe et al., 1990; Valley et al., 1995) were used to liberate O_2 from the Fo separates at the University of Wisconsin's Stable Isotope Laboratory. The O_2 gas was converted to CO_2 by reaction with graphite at 800 °C and the oxygen isotope composition of the CO_2 was analyzed with the laboratory's Finnigan-MAT 251 mass spectrometer. The $\delta^{18}O$ (SMOW) values of Fo samples were determined by regular analysis of the Gore Mountain Garnet (UWG-2) standard (Valley et al., 1995). Each size fraction was treated independently in order to identify any relationships between $\delta^{18}O_{Fo}$ and grain size.

1.4 Results

1.4.1 Forsterite Textures

The Fo textural data for all analyzed samples are compiled in Table 1-2. The number of forsterite crystals per mole forsterite and mean forsterite area (average grain size, mm^2) are plotted against the distance of the sample from the intrusive contact with the Alta Stock in Figures 1-4 and 1-5, respectively. Also shown in Figures 1-4 and 1-5 are the $\delta^{18}O$ values of the carbonate matrix from each sample; these results will be discussed in detail in following sections. From these data, several trends are evident. First, the number of forsterite crystals per mole forsterite increases substantially as distance from the intrusive contact with the Alta Stock decreases (Figure 1-4); a >3 order of magnitude difference is observed between samples nearest to the contact (2.7×10^7 Fo crystals/mol Fo) and those farthest from the contact (as low as 2.4×10^4 crystals/mol). Furthermore, the mean forsterite crystal area (≃average grain size) generally decreases as distance from the intrusive contact is decreased (Figure 1-5), ranging from 0.004 mm^2 (10 m

Table 1-2. Forsterite (Fo) textural data from QEMSCAN measurements and Chadwell (2005).

Scan	Distance From Intrusion (m)	Total Scan Area (mm^2)	[3]Average Area (mm^2) per Fo Crystal	Mean Fo Length (mm)	[4]Number of Fo Crystals /cm^2	Number of Fo Crystals /cm^3	Total Fo Area (mm^2)	[5]Total Moles Fo /cm^3	[5]Number of Fo Crystals /mol Fo
12-1b	10	96	0.004	0.085	449	9513	1.78	3.90E-04	2.44E+07
23B (1)	25	108	0.012	0.135	1130	37967	14.11	2.97E-03	1.28E+07
23B (2)	25	100	0.005	0.094	1830	78285	8.49	2.01E-03	3.89E+07
94I-9-2-a	175	100	0.010	0.134	744	20294	7.48	1.64E-03	1.24E+07
94I-9-2-b	175	108	0.015	0.151	337	6188	5.42	1.09E-03	5.70E+06
88-8	220	100	0.019	0.192	397	7910	7.60	1.66E-03	4.78E+06
88-7[1]	230	100	0.056	0.394	-	-	-	-	7.00E+05
A-1-1	300	100	0.013	0.156	460	9866	6.00	1.31E-03	7.55E+06
A-3-1	300	100	0.021	0.182	138	1621	2.86	6.24E-04	2.60E+06
B-8-3A	300	100	0.028	0.127	40	253	1.12	2.45E-04	1.03E+06
88-60 (1)	315	36	0.012	0.119	264	4287	1.12	6.70E-04	6.40E+06
88-60 (2)	315	108	0.013	0.129	220	3271	2.98	6.01E-04	5.45E+06
FZ9-18[1]	455	100	0.013	0.180	-	-	-	-	3.36E+06
FZ4-4a[1]	475	100	0.024	0.274	-	-	-	-	1.10E+06
88-C5	550	108	0.218	0.482	24	118	6.10	1.23E-03	9.59E+04
88-20[2] (1)	570	84	0.042	0.200	394	7821	16.72	5.45E-03	1.43E+06
88-20[2] (2)	570	100	0.046	0.165	650	16572	29.78	6.84E-03	2.42E+06
88-20[2] (3)	570	108	0.022	0.081	1646	66780	36.16	7.44E-03	8.98E+06
99V-3	615	108	0.041	0.235	44	296	2.98	6.28E-04	4.72E+05
99V-5a[1]	615	100	0.490	1.110	-	-	-	-	2.40E+04

[1]Data from Chadwell (2005) [2]Not utilized in plots due to difficulty in correcting data for a high abundance of skeletal Fo
[3]Measure of average grain size [4]The 20μm scan interval allows for reliable inventory of Fo grains 20μm in diameter or larger; smaller grains may not be reliably detected [5]See Appendix I for methods of calculation

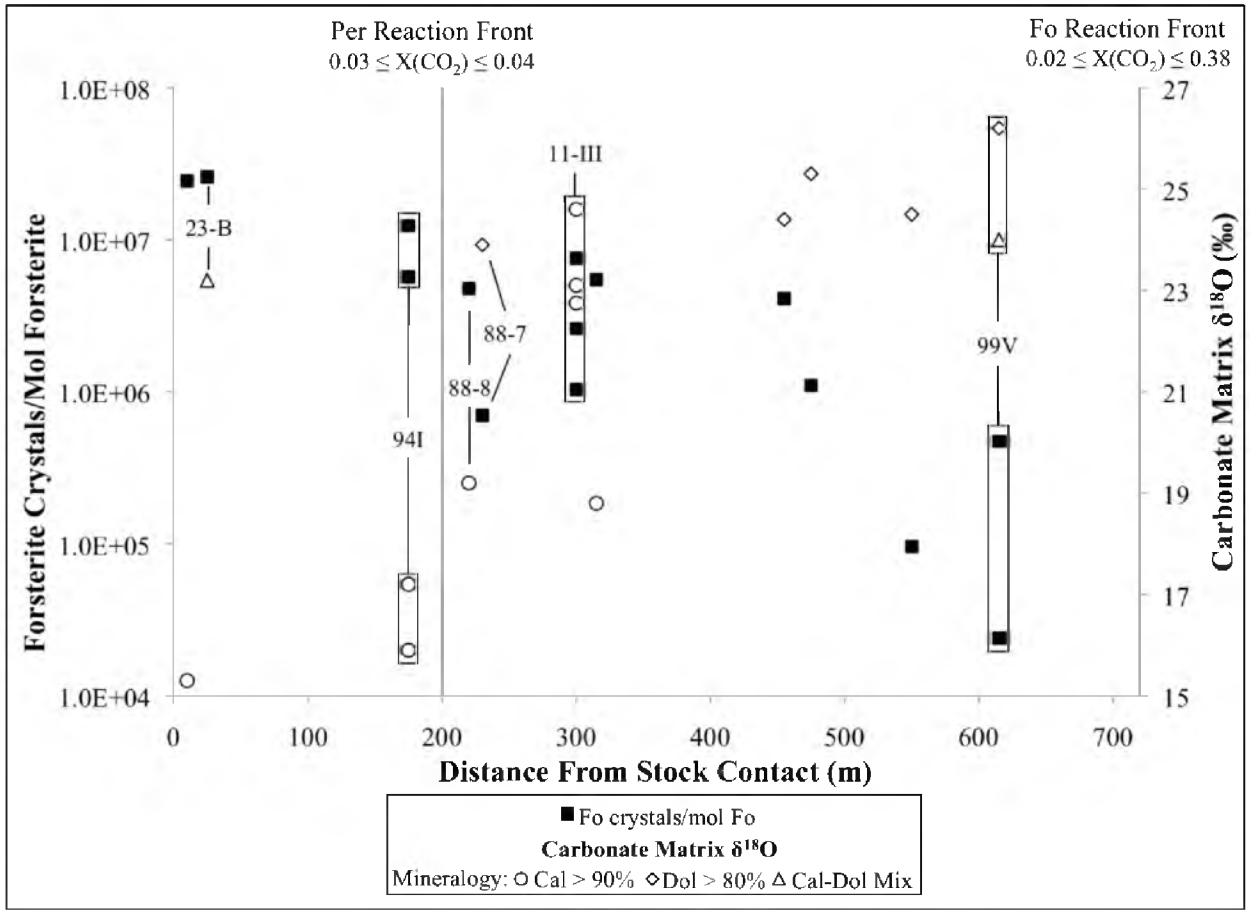

Figure 1-4. Forsterite crystals per mole forsterite and the $\delta^{18}O$ value of the carbonate matrix plotted against distance from the intrusive contact with the Alta Stock for each sample. The locations of the forsterite and periclase isograds, with range of $X(CO_2)$ at each isograd from Cook and Bowman (2000) are present for reference. A general trend of increasing number of Fo crystals per mole Fo with decreasing distance from the stock contact is observed. There is also a tendancy for the carbonate matrix to have a lower $\delta^{18}O$ value with decreasing distance from the contact (23-B is an exception).

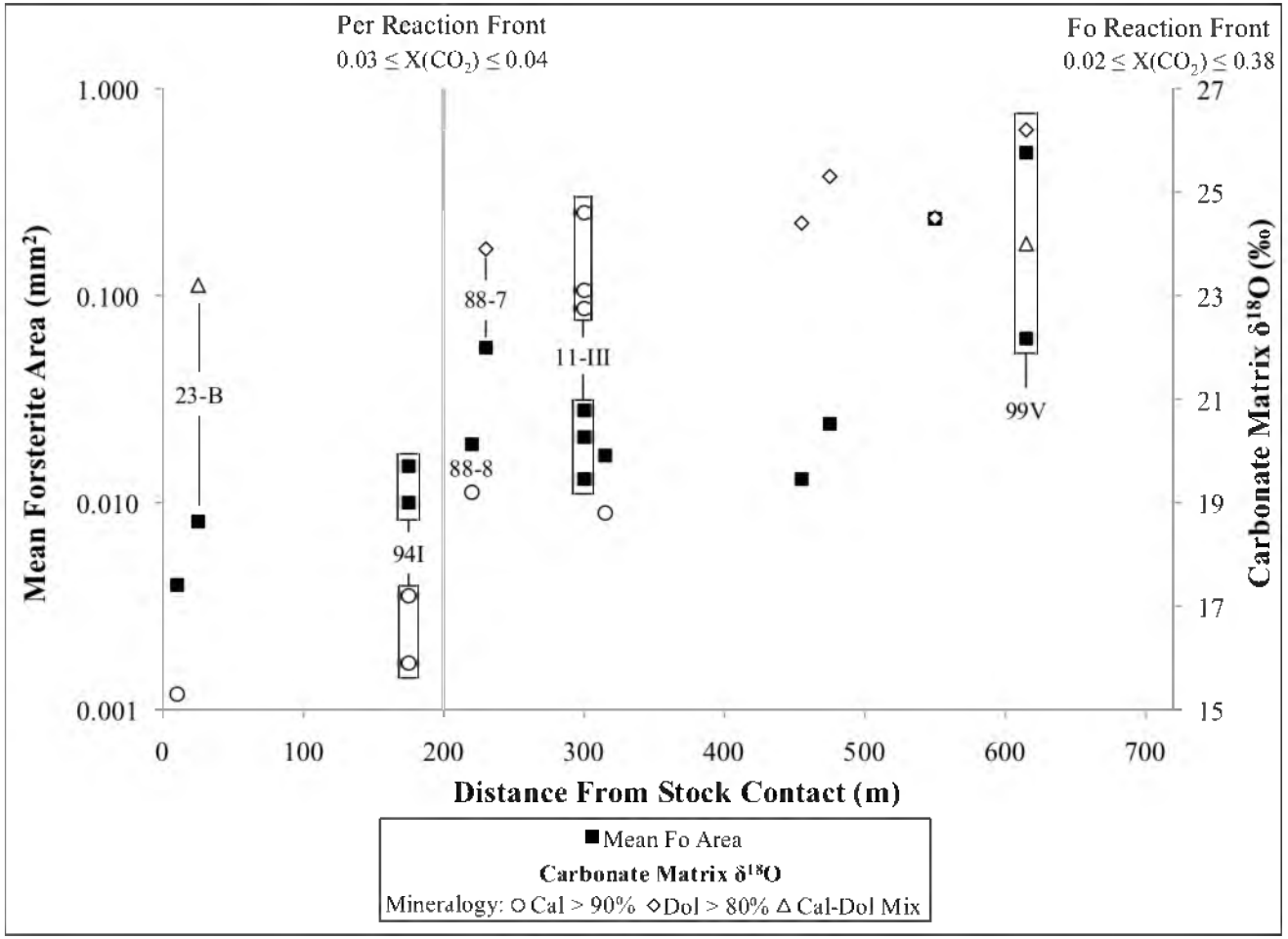

Figure 1-5. Mean area (average grain size in mm^2) of forsterite grains and the $\delta^{18}O$ of the carbonate matrix plotted against distance from the intrusive contact. Symbols and reaction front locations are as in Figure 1-4. Average grain size decreases substantially as the stock contact is approached; the average grain size of the sample nearest to the Alta Stock is more than two orders of magnitude smaller than the sample farthest from the Alta Stock.

from the igneous contact) to as high as 0.490 mm^2 (615 m from the igneous contact). However, significant variation often exists in the number of Fo crystals/mol Fo and average crystal area at any given distance from the intrusive contact with the Alta Stock (for example, sites 99V and 11-III in Figures 1-4 and 1-5).

A strong negative correlation is observed between the number of Fo crystals per mol Fo and mean Fo grain size (Figure 1-6). In addition, there is a strong positive correlation between the average Fo crystal length (longest axis) and the average Fo crystal area (Figure 1-7). QEMSCAN measurements also show that the habit of Fo crystals tends to change with distance from the igneous contact (i.e., with metamorphic grade). QEMSCAN field images for four representative samples at varying distances from the igneous contact are presented in Figure 1-8 (all QEMSCAN images used in this study are compiled in Appendix A). These images document in a qualitative sense that the habit of Fo crystals tends to change from smaller numbers of coarse, generally tabular grains at greater distances from the igneous contact to more numerous, but smaller, acicular grains at intermediate distances, and finally to abundant numbers of small, more equigranular crystals at locations near the intrusive contact. Additionally, Fo crystals present in the lowest grade samples occasionally show euhedral cores with skeletal rims or halos (Figure 1-9), and while the domains do not always show direct contact with one another, optical continuity between domains is generally observed. This suggests that the Fo domains represent the growth of a single skeletal crystal (in three dimensions) or at minimum epitaxial growth of these skeletal halos on grain cores. Primary Dol is usually present in the Fo zone samples, and Fo crystals are often surrounded by well-defined Cal halos (Figure 1-8). Fo-bearing samples from the Per zone generally do not contain primary dolomite.

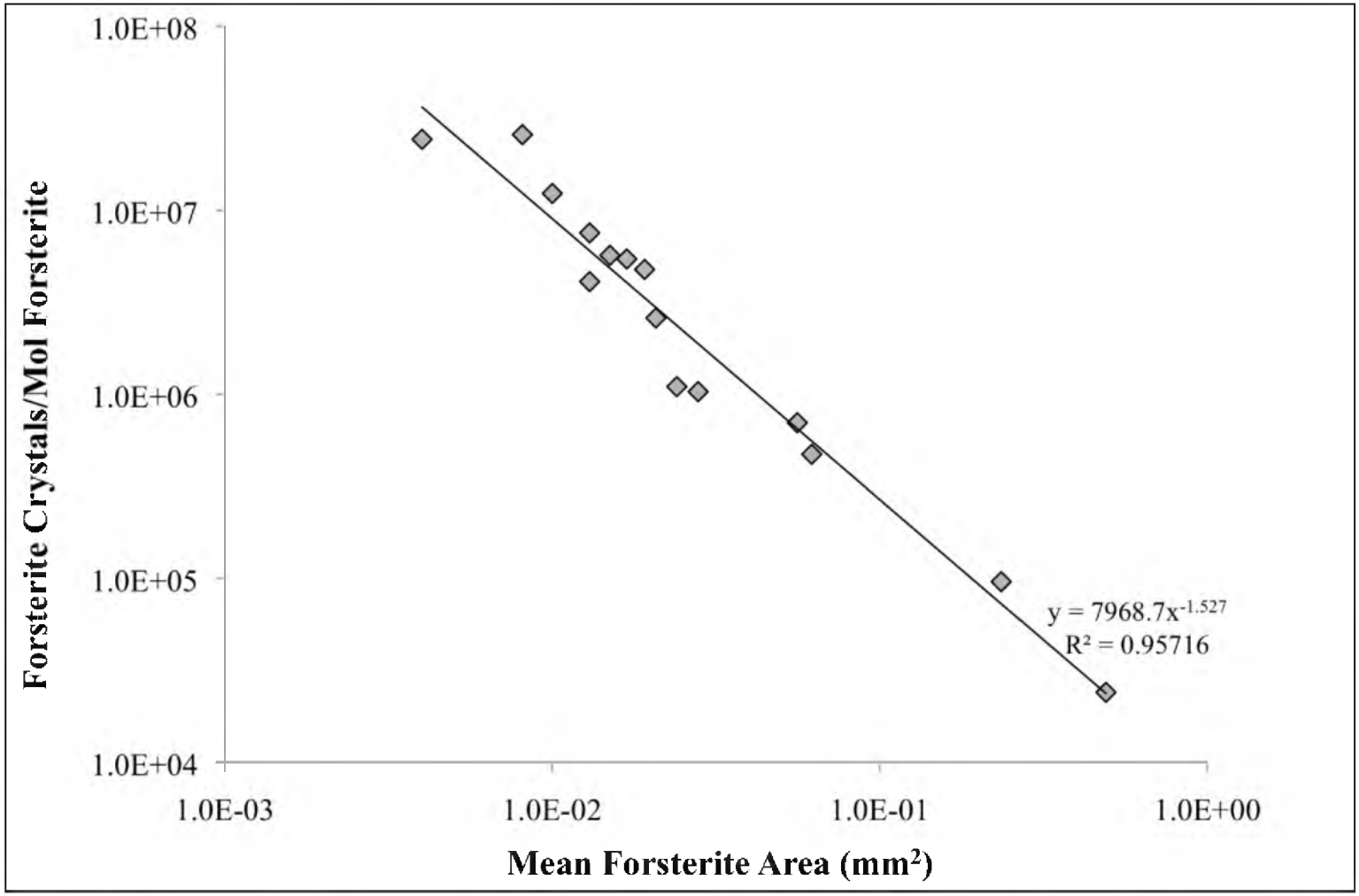

Figure 1-6. Forsterite crystals per mole forsterite plotted against the average crystal area determined through QEMSCAN field images. As the average area of crystals increase, the number of crystals per mole forsterite decreases at an exponential rate.

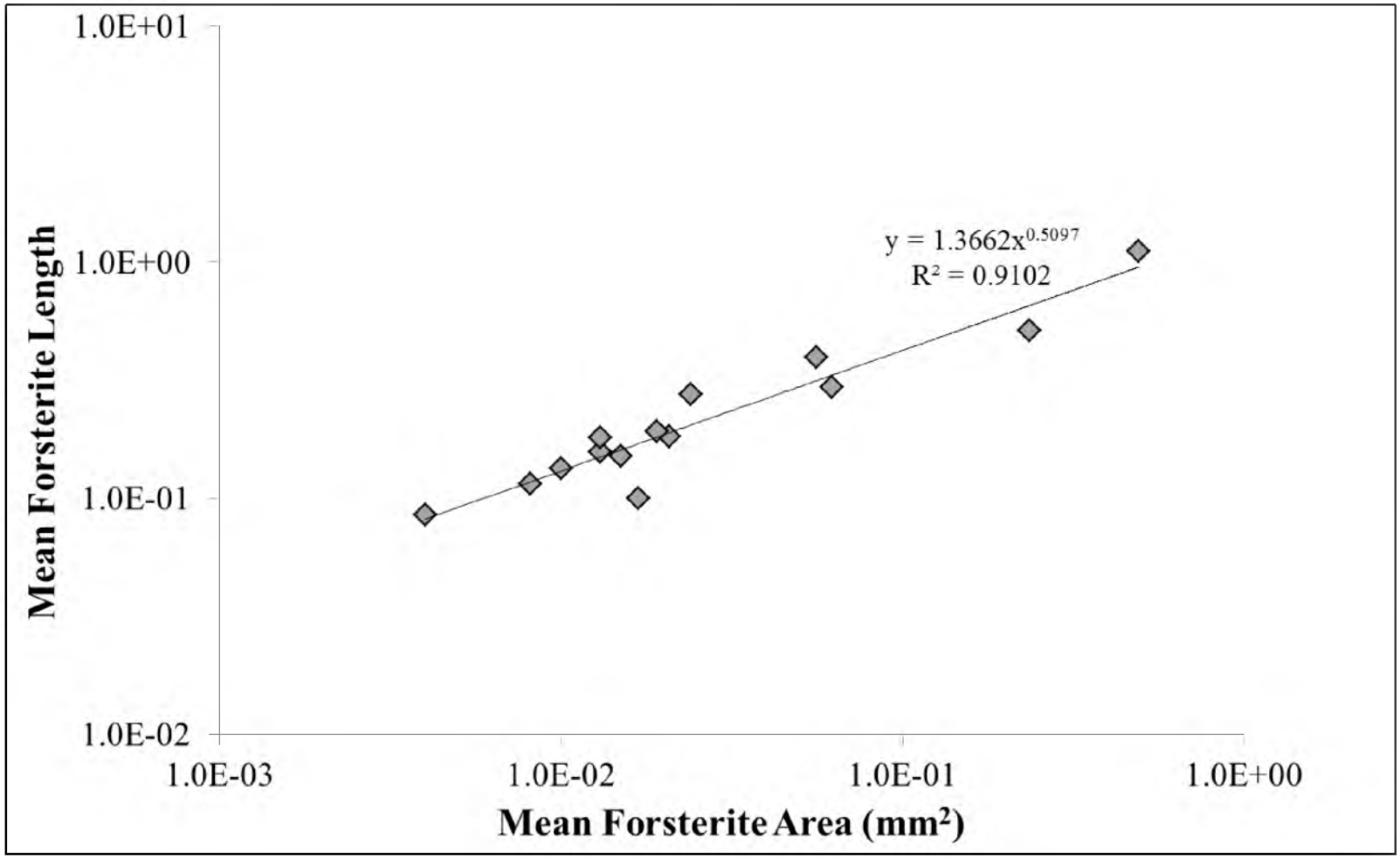

Figure 1-7. Mean forsterite area plotted against mean forsterite length (longest axis) for each sample, as measured through QEMSCAN analysis. A strong correlation exists between the two values, with large grain sizes corresponding to longer lengths.

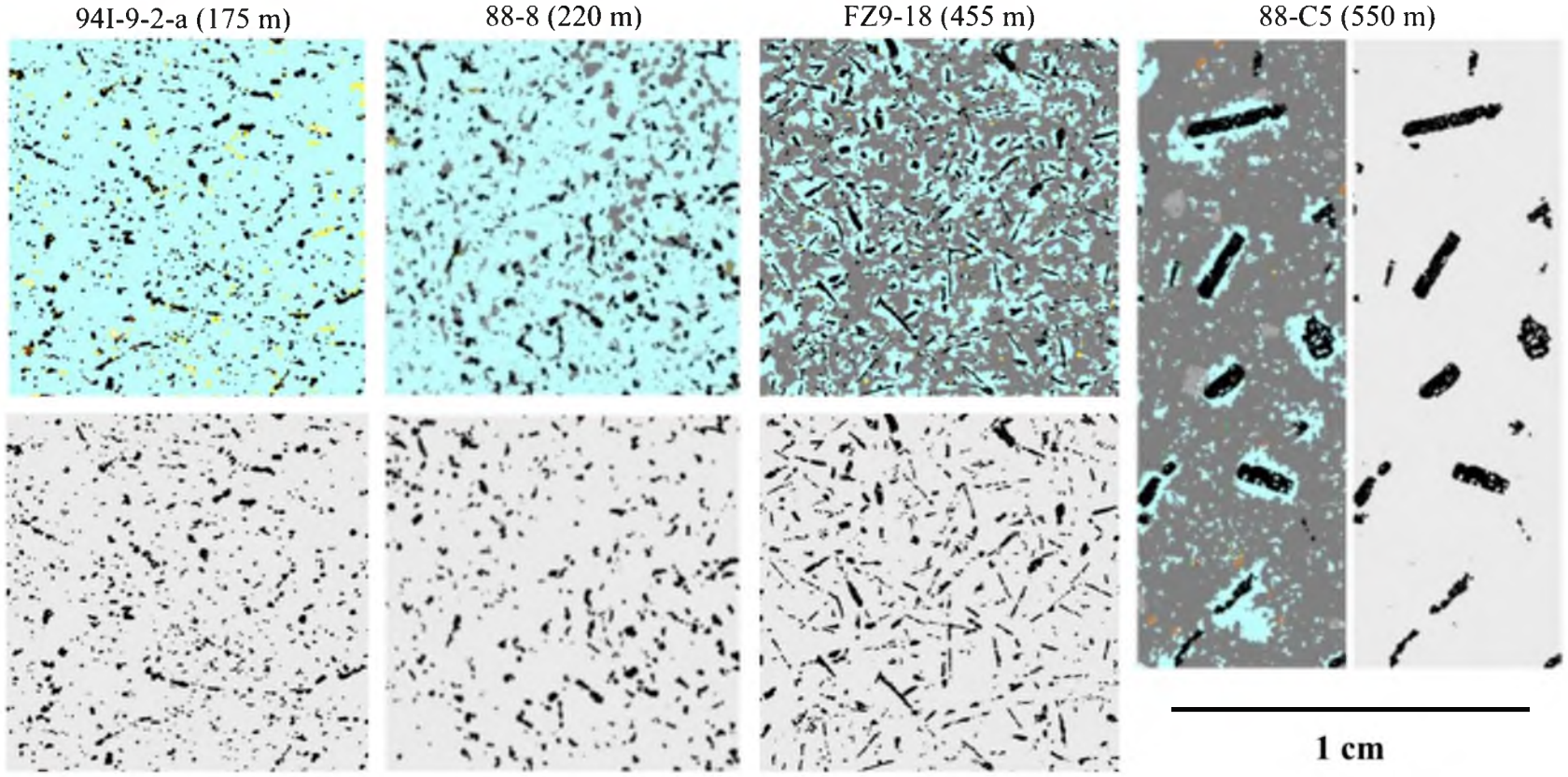

Figure 1-8. Paired QEMSCAN field images in color (showing mineralogy) and black/grey (Fo crystals as black, all other minerals as grey) to illustrate Fo textures for four samples at varying distances from the intrusive contact with the Alta Stock. All images are shown at identical scale, with each scan area equal to 1 cm^2 aside from 88-C5, which has a total scan area of 108 mm^2.

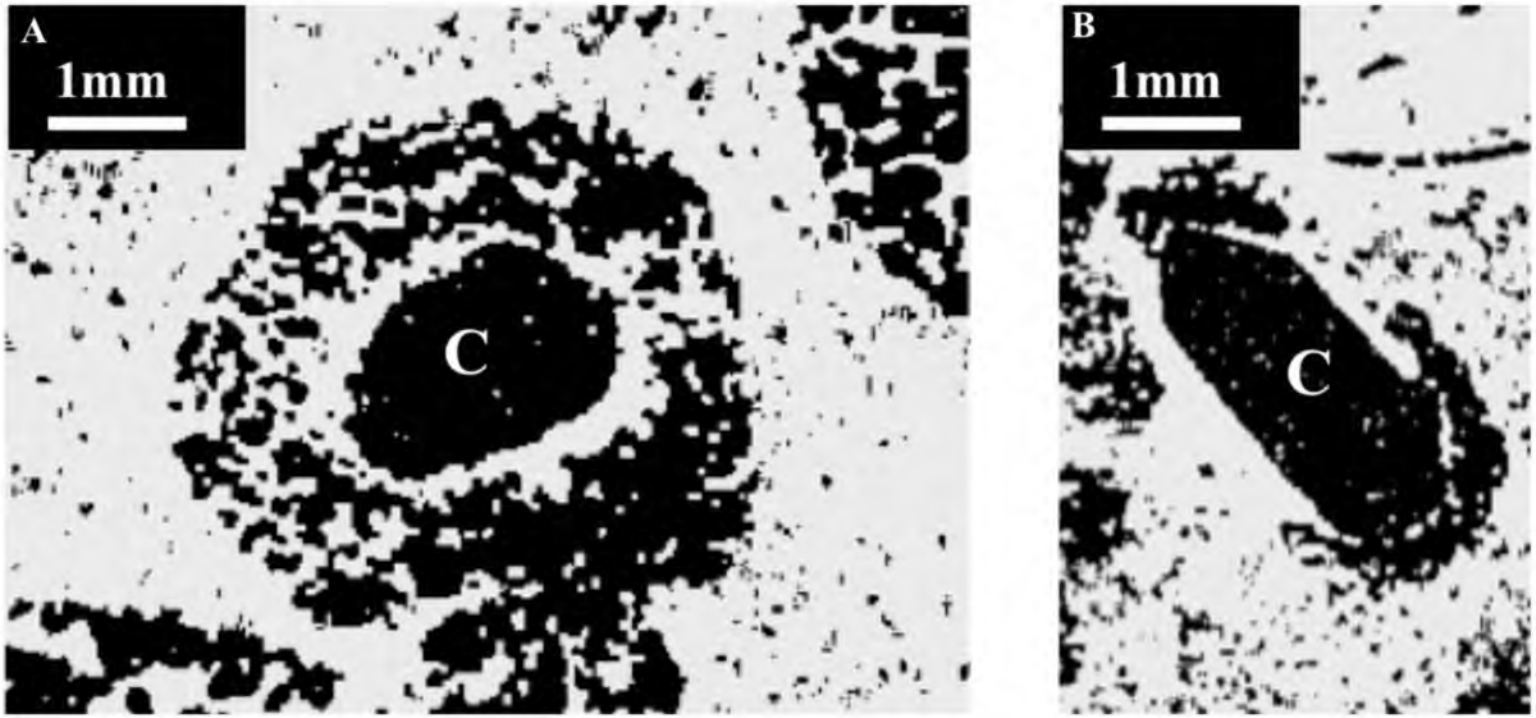

Figure 1-9. QEMSCAN field images showing skeletal Fo (black) halos surrounding and in optical continuity with Fo cores (denoted by C) in sample 88-20 (d = 570 m from the intrusive contact). **(A)** Subhedral equant Fo core with halo. **(B)** Euhedral tabular Fo core with halo.

1.4.2 Oxygen Isotope Compositions of Forsterite and Carbonate Matrix

Measured $\delta^{18}O$ values for carbonate and the various size fractions of forsterite are compiled in Table 1-3. Samples of Fo that experienced excessively low oxygen yields (<60%) during laser fluorination have significantly lower $\delta^{18}O_{Fo}$ values compared to other analyses of the same sample with normal yields (>80%). These low-yield analyses are considered unreliable and are not incorporated when calculating the mean $\delta^{18}O$ value of Fo. Excluding these unreliable analyses, the measured $\delta^{18}O$ values of all size fractions of Fo from a given sample are within two standard deviations of the mean $\delta^{18}O$ value, with the exception of sample FZ9-18 (Table 1-3). Therefore, the analyses provide no evidence for systematic variation in $\delta^{18}O$ value with Fo grain size.

Measured $\delta^{18}O$ values of carbonate matrix and the average $\delta^{18}O$ values of the various size fractions of Fo for each sample are plotted in Figure 1-10. Temperatures defined by calcite-dolomite thermometry range from 500 °C for the forsterite isograd to as high as 650 °C for the igneous contact (Cook and Bowman, 1994). For this temperature range, equilibrium $\Delta^{18}O_{Cal\text{-}Fo}$ should fall between 3.86 and 5.50 ‰, $\Delta^{18}O_{Cal\text{-}Dol}$ should fall between -0.13 and -0.36 ‰, and $\Delta^{18}O_{Dol\text{-}Fo}$ should fall between 3.99 and 5.86 ‰ (Chiba, et al., 1989; Sheppard and Schwarz, 1970). The majority of Fo-carbonate pairs do not conform to these equilibrium $\Delta^{18}O$ values, however, and for most samples measured fractionation factors yield apparent temperatures substantially higher than the upper limit (650 °C) for contact metamorphism defined by calcite-dolomite thermometry (Figure 1-10).

Measured oxygen isotope fractionation factors for the carbonate-Fo pairs are plotted vs. distance from the igneous contact in Figure 1-11. Also shown in Figure 1-11 are the variations in equilibrium $\Delta_{Cal\text{-}Fo}$ (solid line) and $\Delta_{Dol\text{-}Fo}$ (dashed line) factors with

Table 1-3. Oxygen isotope data for forsterite and carbonate in each sample.

Sample	Distance From Intrusion (m)	$\delta^{18}O_{carbonate}$ (‰)	$\delta^{18}O_{Fo}$ (‰) By Size Fraction (μm)[1]						$\Delta^{18}O_{Carbonate\text{-}Fo}$ (‰)
			>853	853-420	420-178	178-106	106-75	Mean	
12-1b	10	15.3	11.4	11.3	11.3	11.4	11.0	11.4	3.9
12-2	10	12.2	-	-	-	5.7	8.0	6.8	5.4
23-B(l)	25	23.2	-	20.3	20.0	20.0	20.1	20.1	3.1
23-B(u)	25	23.7	-	20.2	20.2	20.2	20.0	20.2	3.5
94I-9-2-4	175	15.9	-	15.5	14.6	13.7	13.7	14.4	1.5
94I-9-2-C	175	17.2	-	14.7	15.5	15.2	14.8	15.0	2.2
88-8	220	19.2	15.5	-	-	-	15.4	15.4	3.8
88-7	230	23.9	22.0	-	-	-	21.4	21.7	2.2
A-1-1	300	23.1	21.0	21.0	21.0	20.9	20.8	20.9	2.2
A-1-4 (1)	300	23.9	21.9	-	-	-	21.9	21.9	2.1
A-1-4 (4)	300	24.5	21.7	-	-	-	21.8	21.8	2.8
A-3-1	300	22.8	20.2	20.0	20.1	20.4	19.9	20.1	2.6
A-4-1 (2)	300	23.9	20.1	20.7	-	20.8	20.6	20.7	3.2
A-4-1 (4)	300	23.9	21.3	21.1	-	21.7	21.7	21.5	2.4
B-7-1 coarse	300	23.4	20.7	20.4	21.2	20.9	19.9	20.6	2.8
B-7-1 fine	300	24.4	21.2	21.9	21.8	21.9	21.9	21.7	2.7
B-8-1 lower	300	22.3	20.0	20.3	20.6	19.8	19.2	20.3	2.0
B-8-1 mid	300	22.5	20.1	20.3	20.2	19.8	19.5	20.2	2.3
B-8-3A	300	24.6	21.3	-	-	-	21.4	21.3	3.3
D-6-B coarse	300	20.0	15.2	15.9	-	15.9	15.4	15.6	4.4
D-6-B fine	300	19.4	15.6	-	-	-	15.4	15.4	4.0
88-60	315	18.8	16.3	-	-	-	15.9	16.1	2.7
88-55	370	24.0	20.1	-	-	-	-	20.1	3.9
88-D8	455	22.2	19.7	-	-	-	19.6	19.6	2.6
FZ9-18	455	25.7	-	21.3	20.9	20.1	20.6	21.3	4.5
FZ4-4a	475	26.4	21.1	21.6	21.7	20.9	20.9	21.2	5.2
88-C5	550	24.5	21.8	20.2	20.3	20.4	19.9	20.5	4.0
88-20	570	22.6	19.8	-	-	-	21.2	20.5	2.1
99V-12c	615	24.1	18.9	19.1	18.4	18.2	18.4	18.7	5.4
99V-5a	615	24.0	20.2	20.0	20.4	20.4	20.0	20.2	3.8

[1]Grey values indicate low oxygen yield (<60%). These values are not considered in calculating the mean $\delta^{18}O$ value of forsterite.

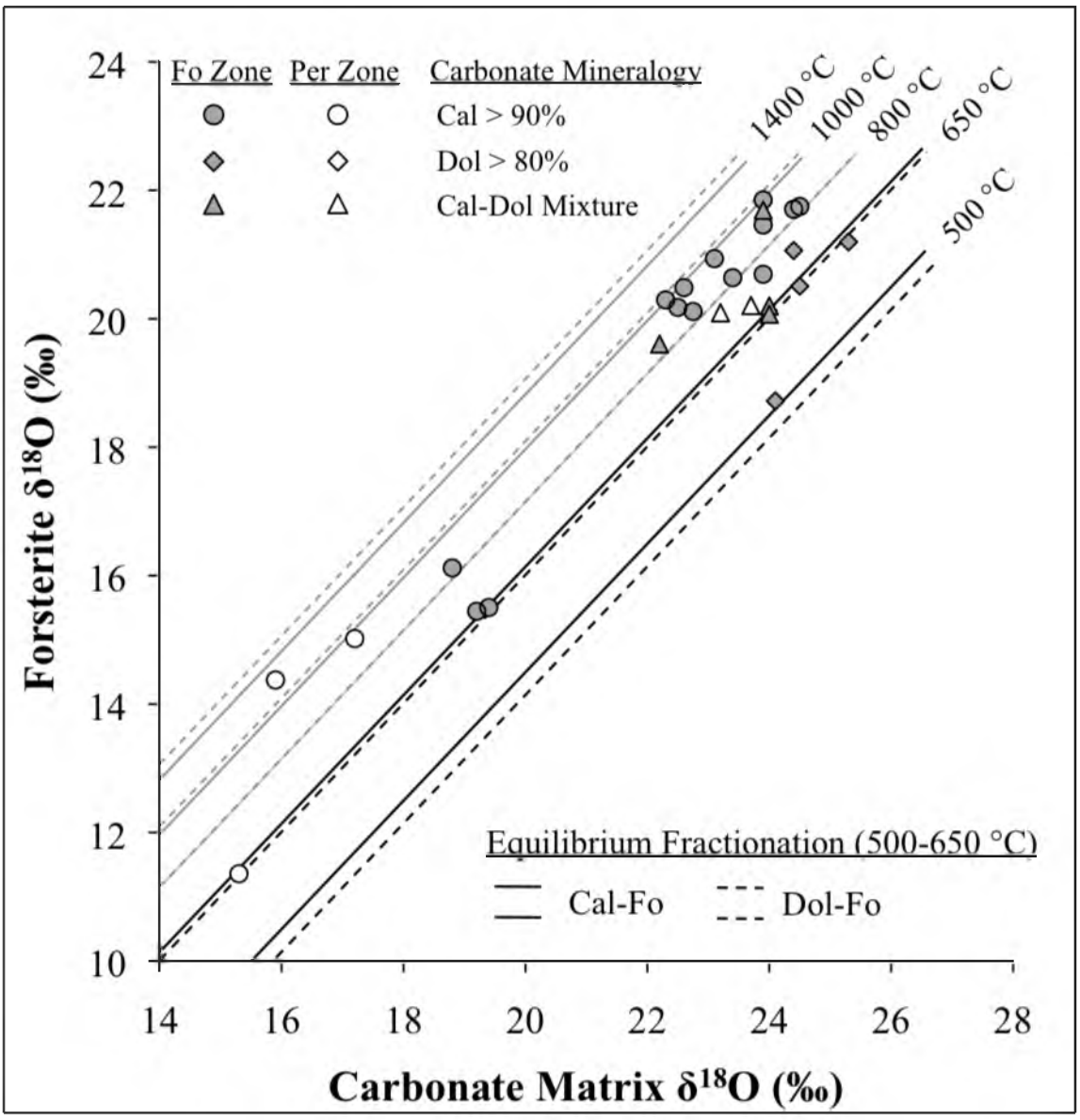

Figure 1-10. Measured $\delta^{18}O$ values for forsterite and carbonate from samples taken throughout the forsterite and peiriclase zones of the Alta aureole. Lines of equilibrium fractionation ($\Delta^{18}O_{carbonate\text{-}Fo}$) as a function of temperature are shown for reference, where solid lines represent equilibrium calcite-forsterite fractionation and dashed lines represent equilibrium dolomite-forsterite fractionation. Fractionation factors for calcite-forsterite and dolomite-calcite (used to calculate dolomite-forsterite fractionation) are from Chiba et al. (1989) and Sheppard and Schwarz (1970). Lines in bold span the range of equilibrium calcite-forsterite and dolomite-forsterite fractionation factors for the temperature range defined for the inner aureole (500-650 °C) by calcite-dolomite thermometry (Cook and Bowman, 1994).

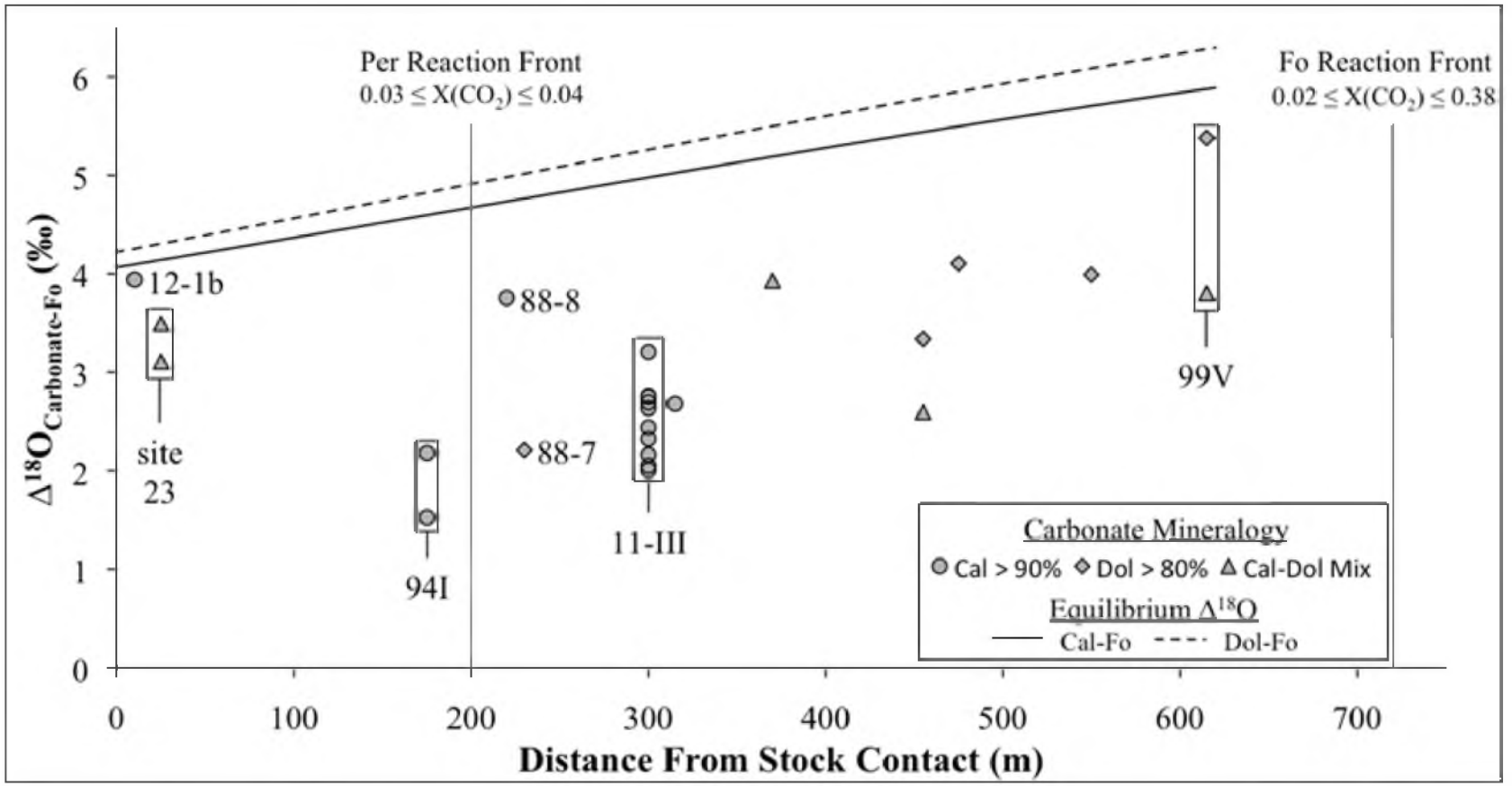

Figure 1-11. Measured $\Delta^{18}O_{Carbonate\text{-}Fo}$ values plotted against distance from the contact with the Alta Stock. Locations of the forsterite and periclase isograds are provided for reference, and site locations are noted where multiple samples were taken from a single outcrop. The equilibrium fractionation factors for calcite-forsterite (solid line) and dolomite-forsterite (dashed line) are shown as a function of distance from the Stock contact, where the temperature at a given distance is defined by calcite-dolomite thermometry results (Cook and Bowman, 1994). All measured fractionation values are smaller than the expected equilibrium fractionation, with the departure from that value generally increasing upgrade across the forsterite zone into the periclase zone. Measured fractionation factors more closely approach equilibrium factors in the inner periclase zone.

distance from the igneous contact, based on results of calcite-dolomite thermometry (Cook and Bowman, 1994). Measured Cal-Fo and Dol-Fo fractionation factors for almost all samples are significantly smaller (often > 1‰) than the equilibrium value at a given position in the aureole. In addition, values of $\Delta^{18}O_{Carbonate\text{-}Fo}$ generally decrease with decreasing distance from the stock contact from the Fo zone into the outer Per zone (Figure 1-11). This trend is shown more clearly in Figure 1-12, where the percent departure from the equilibrium value is defined by equation 1-9:

$$\%Departure = \frac{\Delta^{18}O^{equilibrium}_{carbonate\text{-}Fo} - \Delta^{18}O^{measured}_{carbonate\text{-}Fo}}{\Delta^{18}O^{equilibrium}_{carbonate\text{-}Fo}} \times 100 \qquad (1\text{-}9)$$

is plotted against distance from the intrusive contact. However, sample 88-8 and the samples within the innermost periclase zone are exceptions to these trends, and have $\Delta^{18}O_{Carbonate\text{-}Fo}$ values much closer to the expected equilibrium fractionation factors. Figures 1-11 and 1-12 also show that $\Delta^{18}O_{Cal\text{-}Fo}$ values can vary with the stratigraphy at a given outcrop. Samples from different strata within site 11-III, for example, have $\Delta^{18}O_{Cal\text{-}Fo}$ values ranging from 2.0 to 3.2 ‰, corresponding to an apparent temperature range of 740 - 1007 °C (Chiba et al., 1989) and hundreds of degrees higher than calcite-dolomite thermometry results. The $\delta^{18}O$ value of the carbonate matrix can also vary at a given outcrop location, for example at site 11-III. Figure 1-13 is a plot of the $\delta^{18}O$ values of calcite against the stratigraphic height of samples within Traverse 11-III. The measured $\delta^{18}O$ value of calcite often differs substantially between adjacent stratigraphic layers, and even between distinct textural or mineralogical domains within individual samples. Sample 11-III-B-9-1 (h = 10.5 m), for example, is comprised of two domains

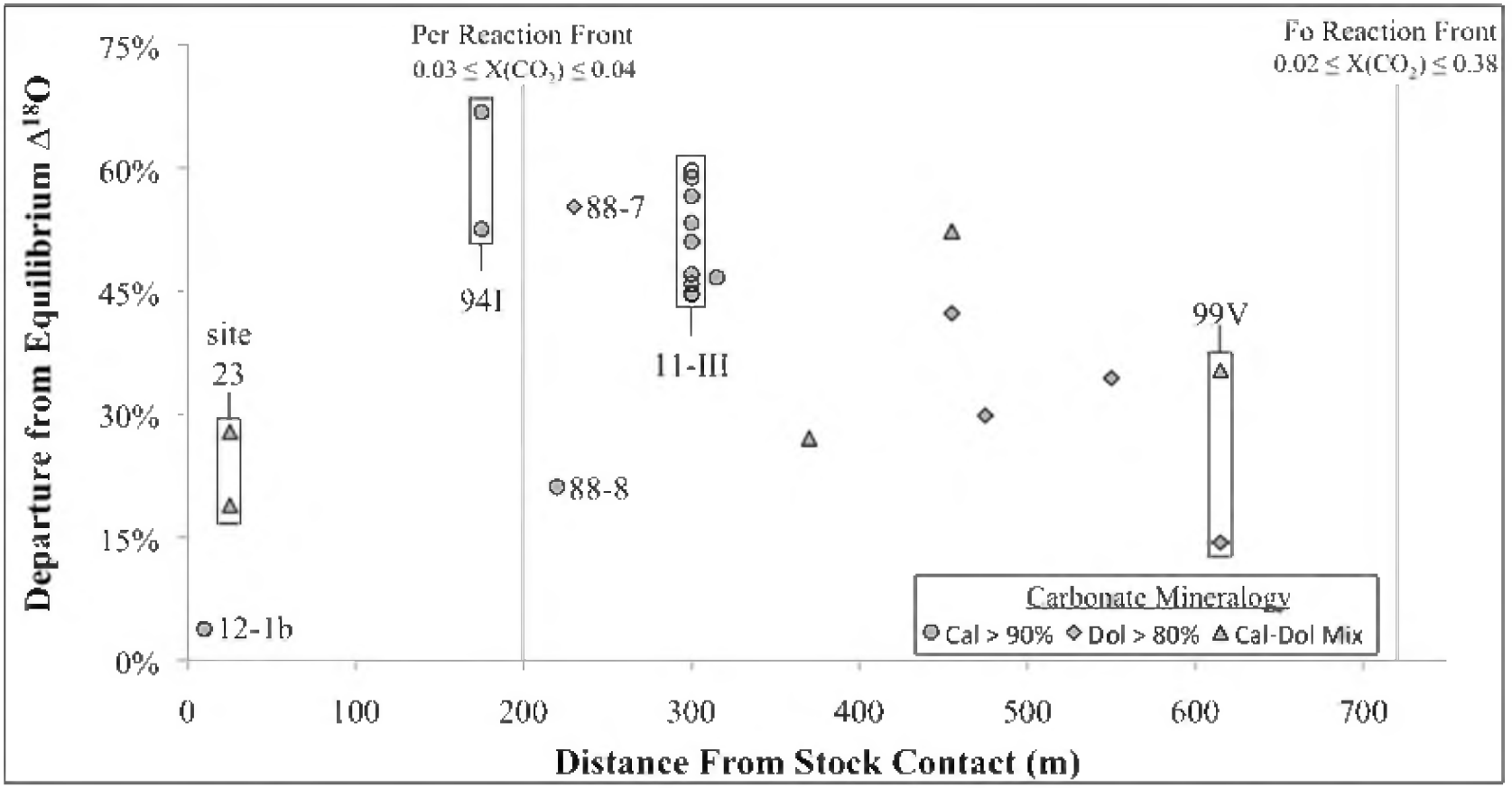

Figure 1-12. Calculated departure of measured calcite-forsterite and dolomite-forsterite fractionation factors from equilibrium calcite-forsterite and dolomite-forsterite $\Delta^{18}O$ values (solid and dashed lines in Figure 1-11, respectively) for each sample plotted against distance from the contact with the Alta Stock. Samples where carbonate analyses reflect calcite-dolomite mixtures are only plotted if the relative proportions of these minerals are known. Locations of the forsterite and periclase isograds are provided, and site locations are noted where multiple samples were taken from a single outcrop. Excluding sample 88-8, departure from the equilibrium fractionation factor generally increases moving upgrade from the forsterite zone into the outer periclase zone, and measured fractionation factors more closely approach equilibrium factors in the inner periclase zone.

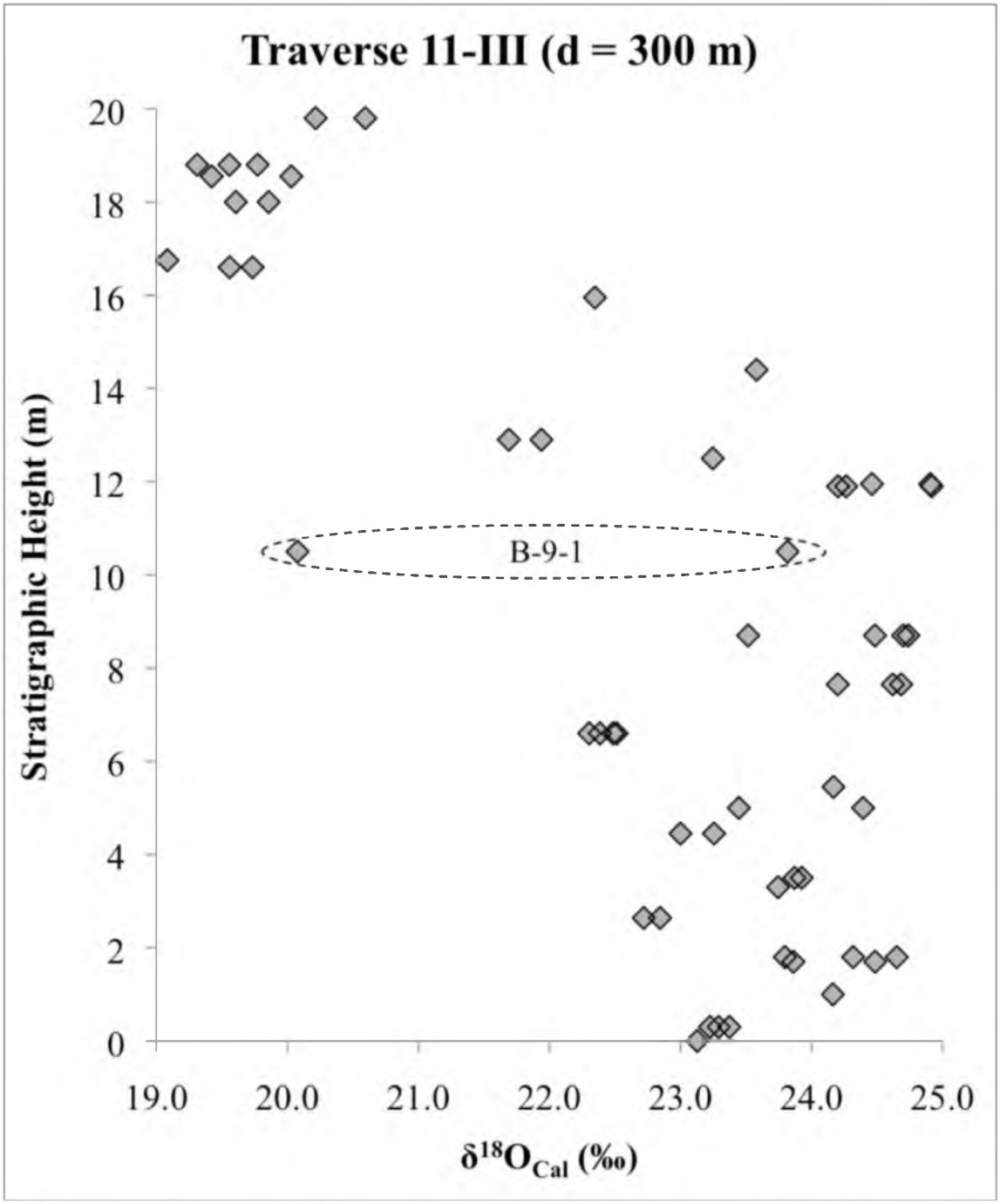

Figure 1-13. Measured $\delta^{18}O$ values for calcite in samples from stratigraphic traverse 11-III plotted against their corresponding stratigraphic height. Sample 11-III-A-1-1 corresponds to h = 0 m, and all other samples are measured in reference to the stratigraphic layer from which A-1-1 was collected. Substantial variation in $\delta^{18}O_{Cal}$ occurs throughout the traverse and often between adjacent layers. Sample B-9-1 is an example in which values vary significantly between domains (the distance between measurements is approximately 10 cm).

with measured values of 20.1 and 23.8 ‰ where the distance between measurements is approximately 10 cm. The $\delta^{18}O$ and $\delta^{13}C$ values for all carbonate samples are presented in Appendix C.

1.5 Discussion

1.5.1 Comparison of Isotopic Data and Forsterite Textures

Some degree of disequilibrium or overstepping of equilibrium reaction boundaries (positive reaction affinity, A_r) is needed to drive all metamorphic reactions. The magnitude of A_r changes according to temperature, pressure, the composition ($X[CO_2]$) of infiltrating fluids, and the flux of these infiltrating fluids in contact metamorphosed carbonate rocks. Previous studies suggest that larger A_r values are produced by elevated temperatures, rapid heating rates, greater relative fluid flux, increasingly H_2O-rich infiltrating fluids, or some combination of these factors (Roselle et al., 1997; Müller et al., 2009; Ferry et al., 2011). Variations in reaction affinity (overstepping) result in systematic changes in both the growth rate and nucleation rate of Fo, which have a different functional dependence on A_r (Ridley and Thompson, 1986). At small degrees of reaction overstepping (low A_r), the growth rate increases more rapidly than the nucleation rate (Figure 1-14), resulting in relatively few large crystals and a low Fo crystals/mol Fo value. However, at sufficiently high degrees of reaction overstepping, the nucleation rate is enhanced relative to the growth rate, and larger numbers of smaller grains are produced. As a result, the Fo crystals/mol Fo value is a monitor of the degree of reaction overstepping (A_r) because it is proportional to the ratio of the time-integrated nucleation rate to the time-integrated growth rate (Roselle et al., 1997).

In the inner Alta aureole, the number of Fo crystals/mol Fo increases and the

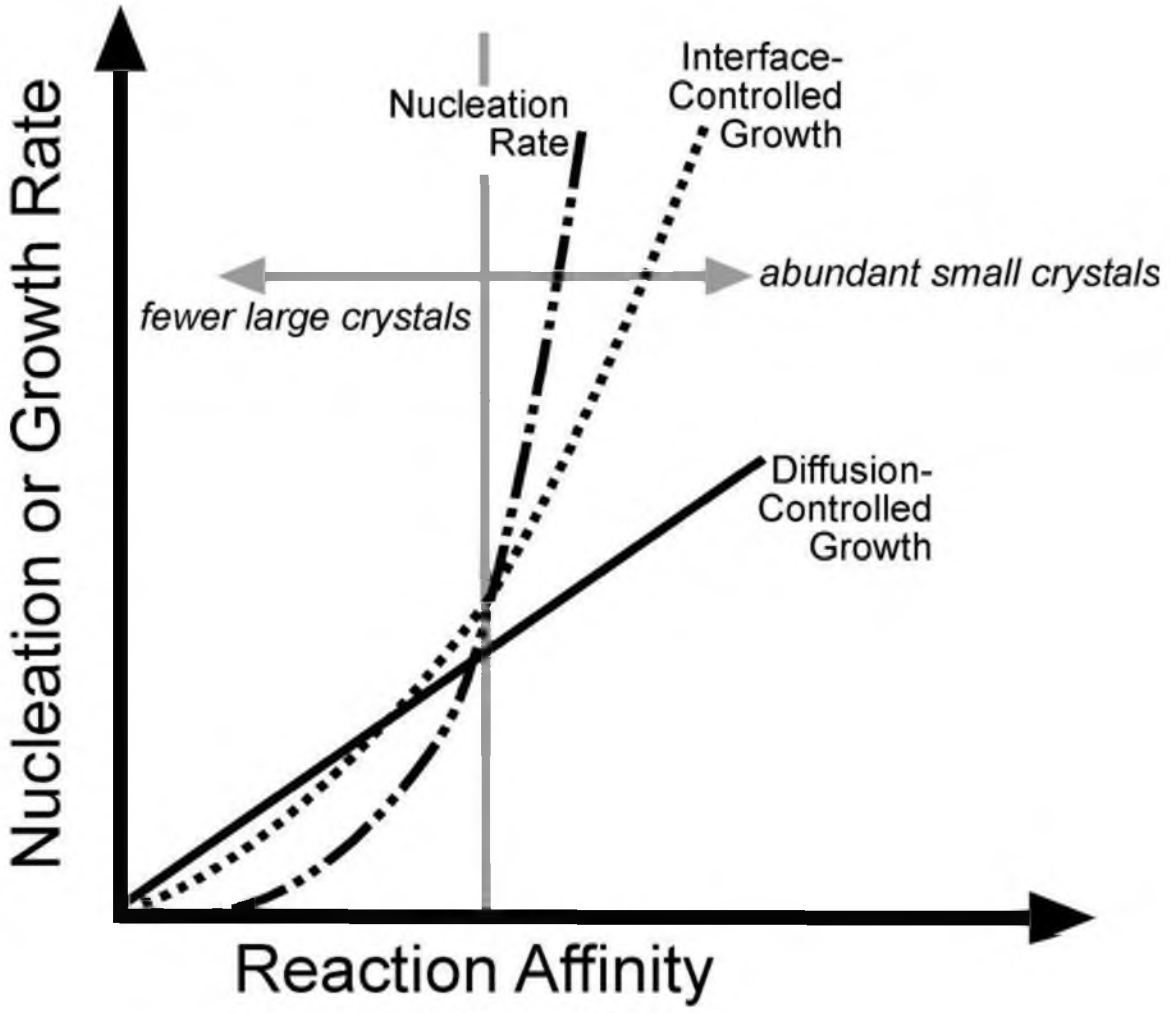

Figure 1-14. Plot showing relative crystal nucleation and crystal growth rates as a function of reaction affinity (A_r). Crystal growth rates increase more rapidly than nucleation rate at low A_r, which produces small numbers of Fo crystals/mol Fo values and a larger average grain size. At sufficiently high reaction affinity, the nucleation rate is enhanced relative to the growth rate, resulting in a greater number of Fo crystals per mole Fo and a smaller average grain size. Modified from Roselle et. al. (1997).

average Fo grain area decreases with decreased distance (increasing temperature) from the intrusive contact (Figures 1-4 and 1-5, respectively). Roselle et al. (1997) measured similar trends in the forsterite marbles of the Ubehebe Peak. Those authors interpreted these textural changes to result from increased reaction overstepping produced by an increase in temperature and/or heating rates closer to the intrusion, as nucleation rates increase faster than crystal growth rates with increased reaction affinity (increased temperature) (Ridley and Thompson, 1986). Ferry et al. (2011) suggest that lower $X(CO_2)$ in infiltrating fluids is associated with greater reaction affinity in samples of Fo marble from the Twin Lakes Pendant, California and the Beinn an Dubhaich aureole, Scotland. T-$X(CO_2)$ phase equlibria and calcite-dolomite thermometry data for the Alta aureole indicate that infiltrating fluids are very H_2O rich ($X(CO_2) \leq 0.04$) closer to the igneous contact and have higher $X(CO_2)$ values down-grade (Figure 1-4; see also Figure 3 in Cook and Bowman, 2000). Therefore, the ~3 order of magnitude increase in the number of Fo crystals/mol Fo from the outer Fo zone into the inner Per zone could reflect increased reaction affinity from the combined effects of elevated temperatures, more rapid heating rates, and lower $X(CO_2)$ in infiltrating fluids as the igneous contact is approached.

The general lack of attainment of oxygen isotope exchange equilibrium among forsterite, calcite, and dolomite across the Fo zone and much of the Per zone (Figures 1-11 and 1-12) also suggests that persistent reaction overstepping was associated with the formation of forsterite in the Alta aureole. The increasing departure from exchange equilibrium between forsterite and carbonate (Figure 1-12) suggests that the reaction overstepping (reaction affinity) increases across the forsterite zone into the outer periclase zone.

However, at any given location within the Alta aureole, significant variation can exist in the Fo crystals/mol Fo value and average grain area (for example sites 99V and 11-III in Figures 1-4 and 1-5) and in percent departure from oxygen isotope exchange equilibrium (Figure 1-12). Samples taken from different stratigraphic intervals within a given outcrop have presumably experienced identical thermal histories because their distances from the intrusive contact are equivalent. Thus the variation in Fo textures and extent of oxygen isotope disequilibrium within sites 94I, 11-III, 88-7/88-8, and 99V (Figures 1-4, 1-5, and 1-12) cannot be explained by differences in temperature or heating rates.

The oxygen isotope data provide some insights into these variations. Fo crystals/mol Fo values are plotted against measured $\delta^{18}O_{Carbonate}$ in Figure 1-15. Low $\delta^{18}O$ values generally correspond with elevated values of Fo crystals/mol Fo from the middle Fo zone ($d < 460$ m) into the periclase zone. Aside from site 99V (615 m), this negative correlation is also observed within strata at several outcrops within the inner aureole. Examples include sites 94I, 11-III, and samples 88-7 and 88-8 from different outcrops but very similar distances from the igneous contact (220 and 230 m, respectively). In the inner Alta aureole, the $\delta^{18}O$ value of the carbonate matrix reflects relative fluid flux, with lower $\delta^{18}O$ marbles resulting from greater fluid flux (Bowman et al., 1994, 2009). The association between elevated numbers of Fo crystals/mol Fo and low measured $\delta^{18}O$ of carbonate minerals at these locations therefore suggests that the degree of reaction overstepping in strata at sites 94I, 88-7/88-8, and 11-III is driven at least in part by the relative fluxes of infiltrating low $X(CO_2)$ fluids; the strata more depleted in $^{18}O/^{16}O$ have experienced a greater fluid flux, are more overstepped, and have a higher number of forsterite crystals per mole forsterite.

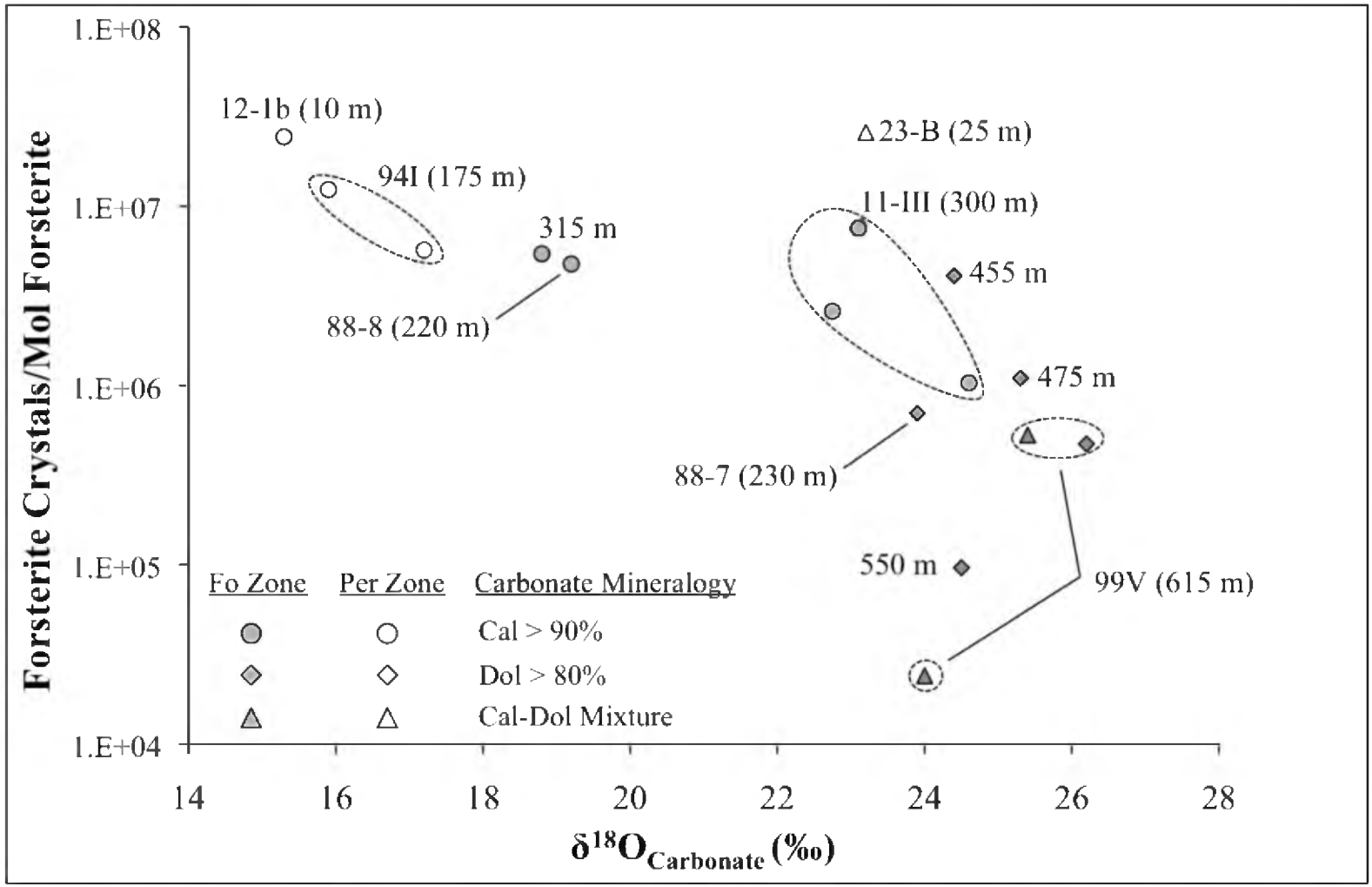

Figure 1-15. Forsterite crystals per mole forsterite plotted against the measured $\delta^{18}O$ value of the carbonate matrix for each sample. Carbonate matrix mineralogy is denoted by symbol shape, and the color of the symbol indicates the zone from which the sample was collected (white for periclase zone, grey for forsterite zone).

Sample 23-B, however, is an exception to this trend in that it has both a high $\delta^{18}O_{Carbonate}$ value (23.2 ‰) and an elevated number of Fo crystals/mol Fo. The carbonate matrix measured in 23-B is a mixture of calcite and dolomite, as it was not possible to isolate either mineral with the dental drill used to collect carbonate powders. As sample 23-B is located close to the igneous contact (d =35 m), its high $\delta^{18}O_{carbonate}$ value indicates that it was subjected to relatively low fluid flux and limited fluid-rock interaction. The higher measured $\delta^{18}O$ for the dolomite-calcite mixture in this sample may therefore reflect the residual dolomite retaining (or partly retaining) its initially high ($\geq$ +26 ‰) $\delta^{18}O$ value. If this is the case, overstepping in this sample, as reflected by the high calculated Fo crystal/mol Fo value, is driven primarily through elevated temperatures and/or heating rates. To evaluate this hypothesis further, however, it will be necessary to obtain separate oxygen isotope analyses for calcite and dolomite in this sample.

Furthermore, all samples in the outer Fo zone (d > 460 m), including those at site 99V, have high $\delta^{18}O_{Carbonate}$ values between 24.0 and 26.2 ‰, yet the Fo crystals/mol Fo ratio varies by over two orders of magnitude with no systematic change in $\delta^{18}O$ (Figures 1-4 and 1-15). Previous studies (Bowman et al., 1994; Cook et al., 1997; Cook and Bowman, 2000) demonstrate that the pathway for metamorphic fluid flow in the Alta aureole is down-temperature and laterally away from the intrusive contact, producing significant $^{18}O/^{16}O$ depletion in infiltrated strata within ~300 m of the igneous contact. However, as a result of continued $^{18}O/^{16}O$ exchange between the infiltrating fluid and marble along these flow paths, an oxygen isotope exchange front is developed 300-400 m from the igneous contact (Bowman et al., 1994). These samples from the outer Fo zone are located beyond (i.e., downstream from) this oxygen isotope exchange front, so fluid infiltration did not produce significant $^{18}O/^{16}O$ depletion in these marbles. As a result,

oxygen isotope values of the carbonate matrix are no longer sensitive to variations in fluid flux, and are not reliable isotopic guides to reaction overstepping induced by fluid infiltration in the outer Fo zone. The lack of correlation between textural data and $\delta^{18}O_{Carbonate}$ in the outer forsterite zone may therefore be explained by the exchanged $\delta^{18}O$ composition of the infiltrating fluid in this part of the Alta aureole.

The relationship between measured carbonate-forsterite $\Delta^{18}O$ fractionation factor and number of Fo crystals/mol Fo also depends on the location within the aureole (Figure 1-16). Within 460 m of the igneous contact, the carbonate-forsterite fractionation factors generally decrease with increasing Fo crystals/mol Fo values, and this relationship is also observed on the outcrop scale at sites 94I and 11-III. The general correlation between these two values suggests that variations in reaction overstepping are consistently expressed both in Fo textures and in the degree of oxygen isotope exchange disequilibrium throughout most of the middle Fo zone and outer Per zone. Exceptions to this relationship include samples in the inner periclase zone (12-1b and 23-B) and samples 88-7 and 88-8 (Figure 1-16); their significance will be discussed in following sections.

In the outer Fo zone (d > 460 m) measured $\Delta^{18}O_{Carbonate\text{-}Fo}$ fractionation factors are larger (> 3.8 ‰) and relatively consistent, whereas values of Fo crystals/mol Fo increase considerably over the distance interval 615 to 475 m. As the infiltrating fluids have largely exchanged with the marbles at these distances, their infiltration will not produce significant $^{18}O/^{16}O$ depletion in these marbles. If the infiltrating fluid has approached exchange equilibrium with the reactant dolomite, it may be that reaction products (forsterite and calcite) will not be as extensively out of equilibrium with each other and with dolomite.

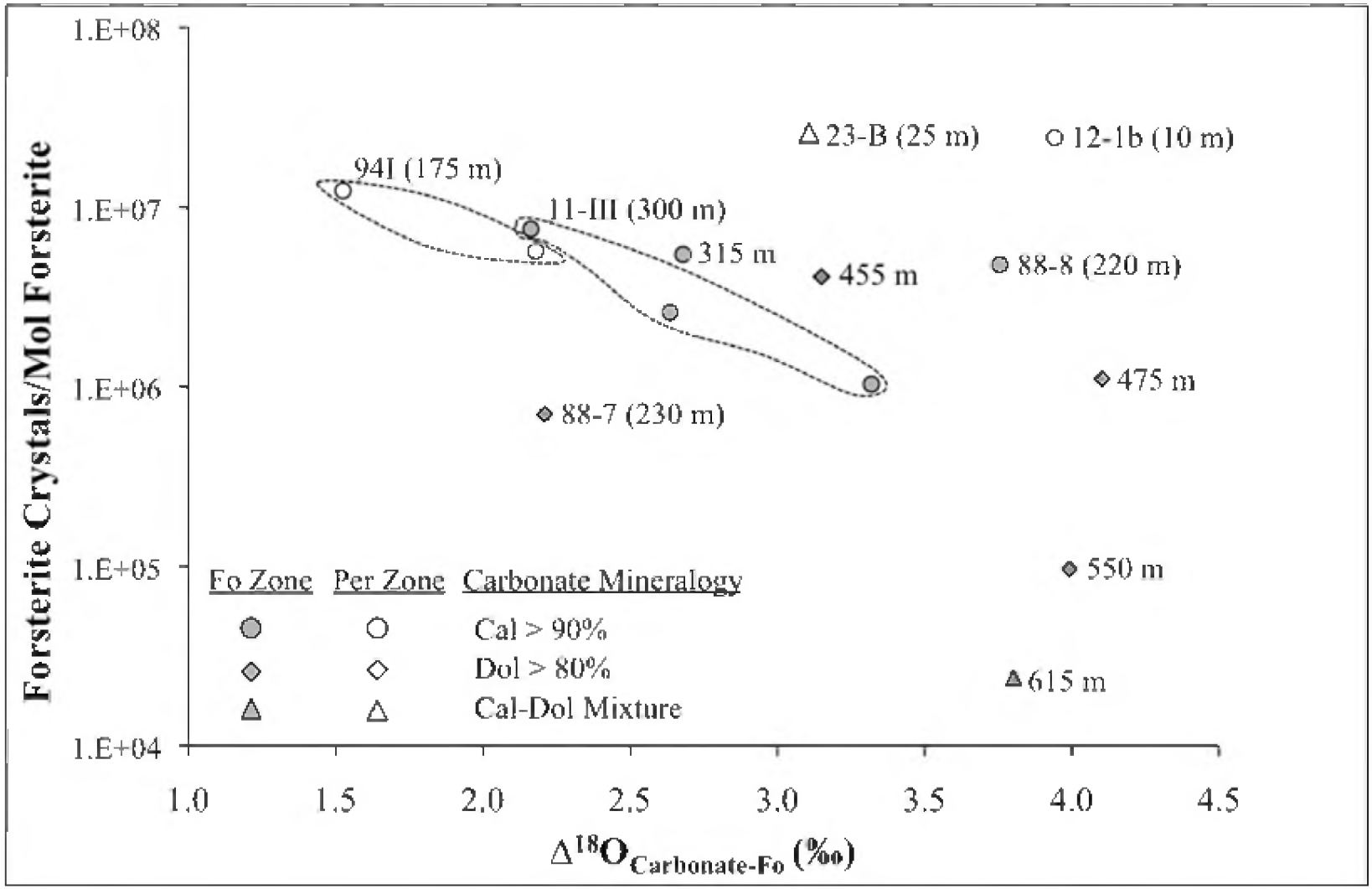

Figure 1-16. Forsterite crystals per mole forsterite plotted against measured carbonate-forsterite $\Delta^{18}O$ fractionation factor.

Inner Per zone samples (12-1b and 23-B) and samples 88-8 and 88-7 are notable exceptions to the trends of increasing number of Fo crystals/mol Fo and decreasing $\Delta^{18}O_{Carbonate\text{-}Fo}$ factors at distances less than 460 m from the Alta Stock. If dolomite in 23-B has indeed retained an initially high $\delta^{18}O$ value as discussed previously, 23-B would have a larger than expected measured $\Delta^{18}O_{Carbonate\text{-}Fo}$ value given its high Fo crystals/mol Fo ratio, which is the highest measured value in the sample suite. Samples 88-8 and 12-1b are similarly characterized by both high numbers of Fo crystals/mol Fo and high $\Delta^{18}O_{Carbonate\text{-}Fo}$ values, but differ from 23-B in that their carbonate mineralogy is dominated by low $\delta^{18}O$ calcite.

Sample KP1L from the Twin Lakes Pendant, California studied by Ferry et al. (2011) is similar to 88-8 and 12-1b in that the measured $\Delta^{18}O_{Cal\text{-}Fo}$ values in all three samples reflect the equilibrium values at the inferred temperatures of the Fo-forming reaction. Furthermore, all three samples have low $\delta^{18}O$ values, indicating that all have experienced significant fluid infiltration. However, KP1L is characterized by a low number of Fo crystals/mol Fo, while 12-1b and 88-8 maintain elevated numbers of Fo crystals/mol Fo. The large $\Delta^{13}C_{Cal\text{-}Dol}$ value measured by Ferry et al. (2010) for KP1L suggests that while this sample was subjected to high fluid flux, the infiltrating fluid was CO_2-rich. The agreement between textural and oxygen isotope monitors for equilibrium in KP1L therefore suggests that A_r is small in this sample as a result of the high $X(CO_2)$ in infiltrating fluids. This is in contrast to 12-1b and 88-8, where textural and oxygen isotope data give apparently conflicting signals of overstepping (A_r).

The calcite matrices of KP1L and the two Alta samples 88-8 and 12-1b have low $\delta^{18}O$ values, indicating that all three samples experienced substantial fluid flux. Ferry et al. (2011) suggest that the infiltrating fluid for KP1L is relatively CO_2-rich, based on the

carbon isotope evidence presented above. In contrast, applications of phase equilibria and calcite-dolomite solvus thermometry in the inner Alta aureole indicate that infiltrating fluids in the inner aureole have low $X(CO_2)$ values of ≤ 0.04 (Cook and Bowman; 1994, 2000).

The Fo textures in samples 12-1b and 88-8 suggest considerable reaction overstepping. One possible explanation for the larger than expected $\Delta^{18}O_{Cal\text{-}Fo}$ fractionation factors in these two samples is that the combination of high flux of H_2O-rich fluid and high temperature promotes fluid-rock interaction and isotope exchange. The presence and flow-through of H_2O-rich, high temperature fluids promotes dissolution, precipitation, and crystallization rates of minerals (Baumgartner and Valley, 2001; Cole and Chakroborty, 2001). Such conditions would allow forsterite and calcite to more closely approach exchange equilibrium with the infiltrating fluid; if both minerals approach exchange equilibrium with the fluid, they must also approach exchange equilibrium with one another. The combination of near-equilibrium $\Delta^{18}O_{Cal\text{-}Fo}$ values and high numbers of Fo crystals/mol Fo in samples 12-1b and 88-8 may therefore be explained by the combination of high fluid flux, low $X(CO_2)$ in the infiltrating fluids, and high temperatures experienced by these samples. Because Ferry et al. (2011) demonstrate that KP1L has also experienced high fluid flux and high temperature (595 °C), variations in reaction affinity between 12-1b and KP1L (as suggested by textural evidence) could be explained by varying $X(CO_2)$ in infiltrating fluids.

Alternatively, the measured $\Delta^{18}O_{Cal\text{-}Fo}$ values in samples 12-1b and 88-8 may be unusually large, given the high numbers of Fo crystals/mol Fo in these two samples because of the retrograde modification of the $\delta^{18}O$ values of calcite. The time scales of contact metamorphism are limited and temperature may change relatively quickly over

this limited time frame. As a result, fluid infiltration driving metamorphic reaction could occur over a substantial range of temperature and could continue past peak temperatures during retrograde cooling. Continued oxygen isotope exchange and recrystallization of calcite at lower temperatures would increase the $\delta^{18}O$ value of the calcite and therefore increase the measured $\Delta^{18}O_{Cal\text{-}Fo}$ fractionation factor, provided the $\delta^{18}O$ value of the infiltrating fluid remains constant. The measured $\Delta^{18}O_{Cal\text{-}Fo}$ fractionation factors in samples 12-1b and 88-8 are about 1.6 ‰ larger than those measured in samples from the outer Per zone. To produce a ~1.6 ‰ increase in the $\delta^{18}O$ value of calcite (and in $\Delta^{18}O_{Cal\text{-}Fo}$), temperatures would have to drop from ~600 °C to 473 °C (Chiba et al., 1989). It is possible that calcite grains could be zoned in $\delta^{18}O$ in response to this retrograde growth and exchange, a possibility that could be tested with ion microprobe measurements.

Sample 88-7 is characterized by a relatively low value of Fo crystals/mol Fo and high $\delta^{18}O$ value of the Cal matrix, suggesting limited reaction affinity due to limited fluid infiltration. However, the low measured value of $\Delta^{18}O_{Cal\text{-}Fo}$ suggests much higher reaction affinity. One possible explanation for this apparent discrepancy is that retrograde infiltration of lower $\delta^{18}O$ fluid lowered the $\delta^{18}O$ value of the Cal matrix to 24 ‰, resulting in an anomalously low $\Delta^{18}O_{Cal\text{-}Fo}$ value.

1.5.2 Summary: Forsterite Formation and Reaction Overstepping

From the middle forsterite zone to the outer periclase zone, the number of Fo crystals/mol Fo increases, the average area per Fo crystal (average grain size) decreases, and the crystal habit changes from tabular to acicular to equigranular. In addition, there is a general lack of oxygen isotope exchange equilibrium between Dol, Cal, and Fo

across this interval, and the degree to which these minerals depart from oxygen isotope exchange equilibrium increases toward the Alta Stock. These trends track progressive reaction overstepping with increased metamorphic grade in the inner Alta aureole. This progressive overstepping is driven by some combination of increasing temperature, faster heating rates, lower $X(CO_2)$ of infiltrating fluids, and greater flux of infiltrating (H_2O-rich) fluids as distance from the intrusive contact decreases. Several exceptions to these general trends occur within the inner aureole. These exceptions may result from promotion of isotope exchange by extremely high flux of H_2O-rich fluids (samples 88-8 and 12-1b), very limited flux of infiltrating fluid (sample 23-B), or retrograde $^{18}O/^{16}O$ depletion of the Cal matrix (sample 88-7).

Significant variations in these textural characteristics of Fo and in measured $\Delta^{18}O_{Carbonate\text{-}Fo}$ factors can occur in different strata within individual outcrops. At several of these sites in the inner Fo zone (11-III) and Per zone (94I), the number of Fo crystals/mol Fo increases with a decrease in both $\delta^{18}O_{Carbonate}$ and $\Delta^{18}O_{Carbonate\text{-}Fo}$. This negative correlation suggests that the flux of infiltrating H_2O-rich fluids is a controlling factor in driving overstepping of the Fo-forming reaction, as samples within individual sites have experienced the same temperature-time history.

However, in the outer forsterite zone ($d > 460$ m), textural parameters (number of Fo crystals/mol Fo, average area per Fo grain) vary independently of the $\delta^{18}O$ value of the carbonate matrix or the $\Delta^{18}O_{Carbonate\text{-}Fo}$ fractionation factor. These isotopic indicators are not well correlated with the textural indicators of disequilibrium because at the distances of the outer Fo zone from the Alta Stock, the infiltrating fluid has equilibrated isotopically with the marbles (Bowman et al., 1994). As a result, the infiltrating fluid cannot produce $^{18}O/^{16}O$ depletion in the marbles, and the $\delta^{18}O$ value of the marble no

longer identifies variations in fluid flux between strata.

The results and interpretations presented here are consistent with those described in several recent studies (Roselle et al., 1997; Müller et al., 2009; Ferry et al., 2011) concerning the dynamics of forsterite-forming reactions within siliceous dolomites in contact aureoles (Ubehebe Peak, Beinn an Dubhaich, and Twin Lakes Pendant, for example). These results highlight the importance of elevated temperatures, faster heating rates, and water-rich fluid infiltration in enhancing the reaction affinity for decarbonation reactions. The agreement between results presented in this and previous studies demonstrates the importance of reaction overstepping in producing forsterite textures and influencing oxygen isotope distributions between forsterite and carbonate minerals in contact metamorphosed dolomite marbles. This study, therefore, has both reaffirmed the significance of disequilibrium processes in metamorphic reactions and has also contributed greater understanding regarding the role of reaction kinetics in the infiltration-driven metamorphism of carbonate rocks.

CHAPTER 2

TRACE ELEMENT CHARACTERIZATION OF THE ALTA STOCK AND CONTACT AUREOLE

2.1 Introduction

The utility of geochemical anomalies in mineral exploration has been well documented in a number of studies (Boyle, 1967; Korzhinskii, 1968; Rose et al., 1979; Escalante et al., 2010) and for a wide range of mineral deposit types, including various skarns, where anomalous concentrations of pathfinder elements essentially delineate a halo surrounding a deposit. Escalante et al. (2010), for example, described the trace element characteristics of both altered and unaltered marble and limestone surrounding the Antamina skarn in Peru, using the ratio of metals to immobile elements (Al_2O_3 and La) to identify geochemical anomalies within the host rocks. This approach was used to identify elements that have been added to or removed from the host rock and to evaluate the extent of wallrock alteration. This approach is therefore useful in vectoring toward hydrothermal fluid sources in ore deposit systems (MacLean and Barrett, 1993).

However, geochemical alteration halos are often not the most distal features of fluid-rock interaction, and numerous studies (Naito et al., 1995; Vázquesz et al., 1998; Kelley et al., 2006, Barker et al., 2013) have demonstrated that isotopic alteration often defines a more expansive halo than element concentration signatures. Specifically, $\delta^{18}O$

depletion halos have been identified for a variety of deposit types, including skarns, Mississippi Valley-type deposits, and Carlin-type gold deposits (Megaw, 1990; Kesler et al., 1995; Naito et al., 1995; Bowman, 1998; Barker et al., 2013). Additionally, since fluid flux is a controlling factor in both the isotopic alteration of wallrock and the endowment of metals in mineral deposits, rocks experiencing the greatest degree of fluid-rock interaction are likely to be both significantly depleted in $^{18}O/^{16}O$ and rich in metals, particularly in areas proximal to fluid sources or conduits. This relationship is identified by Barker, et al. (2013), who demonstrated that exploration drill holes intersecting mineralization (Au > 0.2 opt) in the Screamer Carlin-type gold deposit in Nevada also had significantly lower $\delta^{18}O$ values when compared to nonmineralized areas. These studies suggest that integrated isotopic and geochemical data provide an effective means for identifying areas that have been subjected to the greatest degree of fluid-rock interaction, and the combined use of these tools may allow for more accurate exploration vectoring in many systems.

While the isotopic variations throughout the Alta Stock and its associated contact aureole (a detailed description of the stock and aureole are presented in Chapter 1, section 1.2) have been extensively studied (e.g., Bowman et al., 1994, 2009; Cook et al., 1997), the major and trace element behavior throughout the system has yet to be evaluated, and the spatial distribution of important skarn pathfinder elements (Cu, Pb, Zn) and their relationship with respect to $\delta^{18}O$ value remains poorly characterized. This study, therefore, will identify and quantitatively evaluate concentrations of pathfinder elements throughout the Alta aureole, characterize the major and trace element composition of the Alta Stock and its associated skarns, and will also seek to identify any correlations between $\delta^{18}O$ values and trace element concentrations throughout the system. On a broad

scale, this study will also provide greater insight regarding the utility of integrated isotopic and geochemical data in the exploration of skarn deposits, and will also aid in establishing the degree to which isotopic and geochemical alteration are linked in hydrothermal mineral deposits.

2.2 Methods

2.2.1 Sample Selection and Analytical Methods

Fifty-nine samples were selected for trace element analysis to provide a comprehensive sample suite of the Alta Stock, contact skarns, all four zones of the aureole, and unmetamorphosed protolith. These samples are documented in Appendix D, and sample locations are shown in Figure 2-1. Trace element analyses were made using an Agilent 7500ce Inductively Coupled Plasma Mass Spectrometer (ICP-MS) at the University of Utah. Details of analytical procedures and data reduction techniques are presented in Appendix D.

2.2.2 Calculation of Threshold Values

The concept of threshold values for trace elements has been used to screen false positive anomalies in previous studies regarding trace element mobility in hydrothermal systems (Escalante et al., 2010). Al is demonstrated to be immobile in the marbles of the Alta aureole (Appendix D), and threshold values for a given element in samples from the Alta aureole are determined by normalizing the concentration of that element in the unaltered protolith to Al concentration. Median host rock element:Al ratios were determined for the protolith, and the threshold range for each aureole sample was calculated using the median ± 2 median absolute deviations (MAD) element:Al ratios of

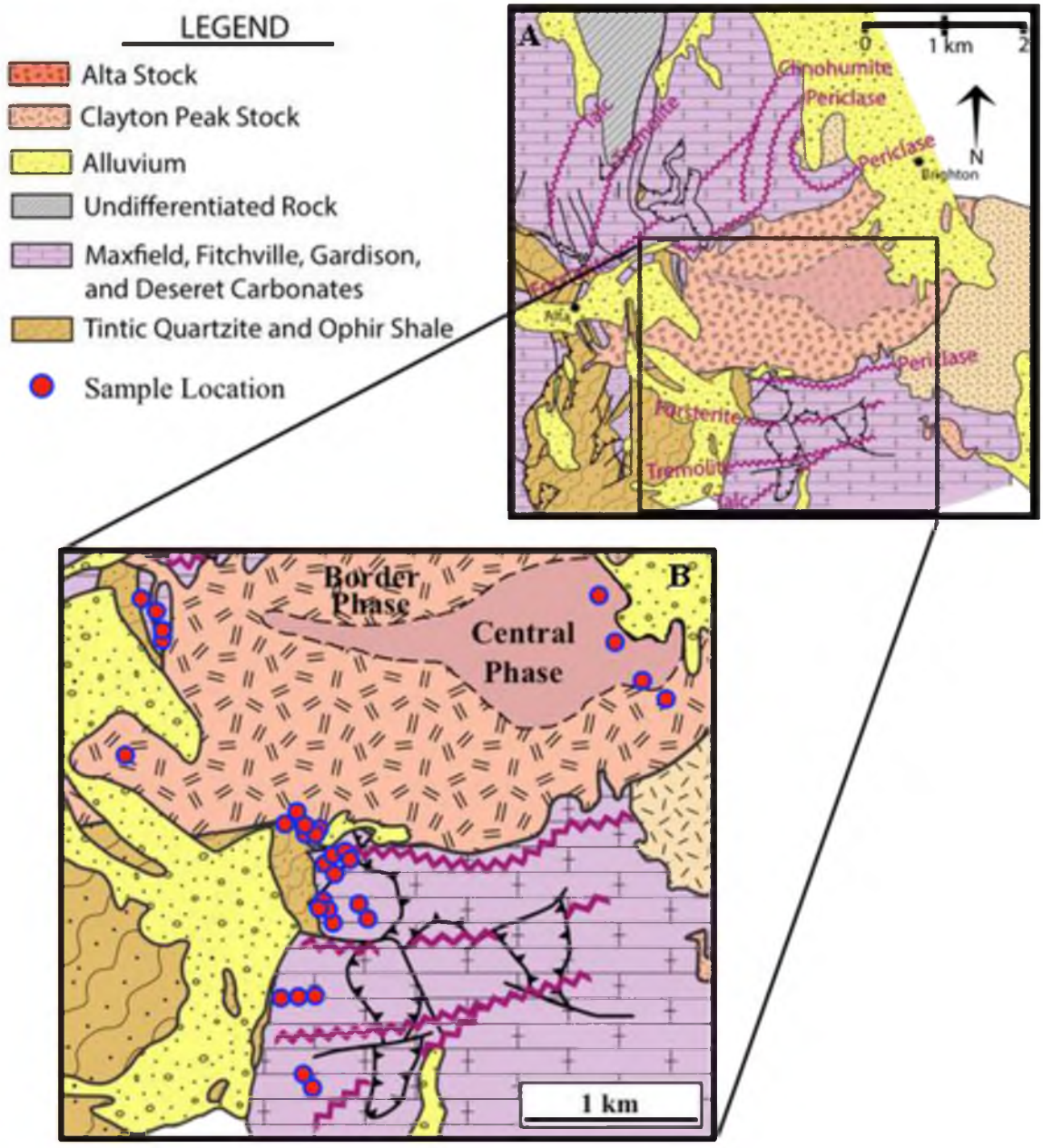

Figure 2-1. Trace element sample locations. **(A)** Simplified geologic map of the Alta Stock and contact aureole. **(B)** Detailed map showing sample locations from which trace element data were collected. Modified from Chadwell (2005) and Johnson (2009).

of the protolith. Details regarding the method for calculating threshold values for trace elements analyzed in this study are included in Appendix D.

2.3 Results

2.3.1 Threshold Ranges

Major and trace element concentrations for all samples are compiled in Appendix D. Evaluation of the mobility of elements in a hydrothermal system requires reliable identification of anomalous concentrations, which requires accurate determination of original concentrations in the protolith. Escalante et al. (2010) calculate threshold values for geochemical alteration by normalizing the concentration of a given element to the concentration of the least mobile element in the system. This method identifies false positive anomalies that may result from passive enrichment of trace elements, which can occur due to volume loss through carbonate dissolution (Escalante et al., 2010).

The strong positive linear correlation between Al concentration and the concentration of other low-solubility elements (detailed in Appendix D) demonstrates that Al is suitable for use as the least mobile element in the Alta aureole. The element:Al range defined by median ± 2MAD values in the unaltered protolith is used to define threshold ranges for the marble samples from the aureole because these values are resistant to outliers. As a result, the median ± 2MAD technique identifies a larger number of anomalies than the threshold defined by the mean ± 2σ (Reimann et al., 2005).

2.3.2 Protolith Characterization

Median values ± 2MAD ranges for major and trace element concentrations (relative to Al) were calculated for the un-metamorphosed carbonate protoliths for the

marbles within the Alta aureole, and are listed in Table 2-1. These ranges are used to define elemental threshold values for each sample throughout the aureole as described in Appendix D. All siliceous dolomite strata in the study area (Cambrian Maxfield and Mississippian Fitchville, Deseret, and Gardison Formations) are included in this carbonate protolith. The grouping of these units into a single set of elemental concentration ranges for the protolith is favorable because it is difficult to accurately identify the protolith of each marble sample, particularly at high metamorphic grades where the original textural and mineralogical characteristics of the protolith are often overprinted by the effects of metamorphism. The median ± 2MAD threshold ranges, therefore, effectively define the range of major and trace element compositions for the marble samples in the aureole prior to any geochemical alteration that these marbles would experience through infiltration-driven metamorphism. These ranges serve as a means for determining concentration anomalies resulting from fluid infiltration associated with the intrusion of the Alta Stock. In the following figures (2-2a to 2-2p), gray dashed lines denote the calculated threshold range for the featured element.

2.3.3 Concentration-Distance Profiles

The element concentrations for each sample along the sampling transect from the interior of the Alta Stock to the unaltered protolith are shown in Figures 2-2a to 2-2p. Measured concentrations (ppb) are plotted against distance (m) along the transect, where d = 0 represents the intrusive contact. Locations of metamorphic mineral isograds are provided for reference, and threshold values (ppb) are indicated by grey dashed lines throughout the aureole. Samples with concentration values less than the limit of detection are not plotted. From the plots, several distinct patterns can be distinguished

Table 2-1. Median and median absolute deviation (MAD) element:Al values for un-metamorphosed protolith samples and the resulting threshold (median ± 2MAD) ranges for each element (excluding Al).

	Median Protolith	MAD Protolith	Upper Threshold	Lower Threshold
Li	3.20E-03	4.89E-03	1.30E-02	1.76E-04
Be	4.08E-04	6.79E-04	1.77E-03	1.34E-04
Ti	8.43E-03	1.55E-02	3.95E-02	5.76E-03
Cu	6.92E-04	1.41E-03	3.50E-03	7.35E-04
Zn	7.34E-02	9.22E-02	2.58E-01	-3.57E-02
Rb	1.20E-04	3.10E-04	7.39E-04	2.60E-04
Sr	1.74E-01	2.85E-01	7.43E-01	4.78E-02
Ba	8.16E-03	1.16E-02	3.13E-02	-1.36E-03
La	5.95E-03	9.20E-03	2.44E-02	5.57E-04
Ce	1.09E-02	1.68E-02	4.45E-02	8.36E-04
Sm	9.98E-04	1.57E-03	4.14E-03	1.53E-04
Lu	4.38E-05	8.72E-05	2.18E-04	4.29E-05
Pb	3.87E-03	5.26E-03	1.44E-02	-1.10E-03
Na	3.13E-01	1.09E+00	2.49E+00	1.24E+00
K	2.67E-02	9.52E-02	2.17E-01	1.10E-01
Mn	6.83E-01	1.02E+00	2.73E+00	-2.23E-03
Fe	3.26E+00	3.73E+00	1.07E+01	-2.33E+00

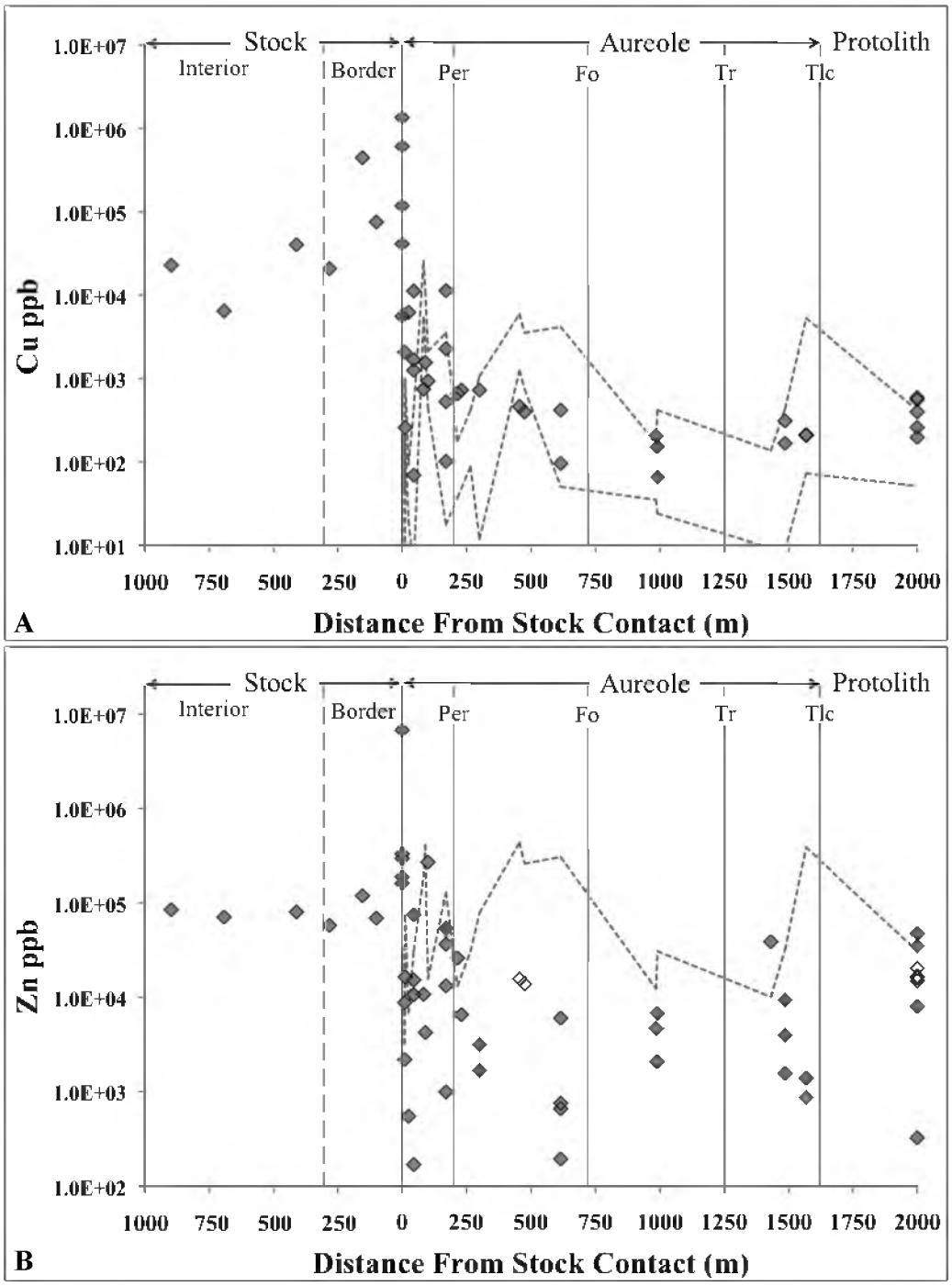

Figure 2-2. Concentration-distance profiles throughout the Alta system. Major lithology changes and isograds are provided, and the threshold range defined by the median protolith value ± 2MAD is shown for each element in the aureole and non-metamorphosed protolith (dashed line). Lower thresholds are not displayed if their values are negative, and a threshold range is not defined for the Alta Stock or skarns because Al immobility cannot be assumed in these environments. Concentration-distance profiles are shown for **(A)** Cu, **(B)** Zn, **(C)** Fe, **(D)** Mn, **(E)** Ti, **(F)** Pb, **(G)** Na, **(H)** K, **(I)** Rb, **(J)** Sr, **(K)** Be, **(L)** Ba, **(M)** La, **(N)** Ce, **(O)** Sm, and **(P)** Lu.

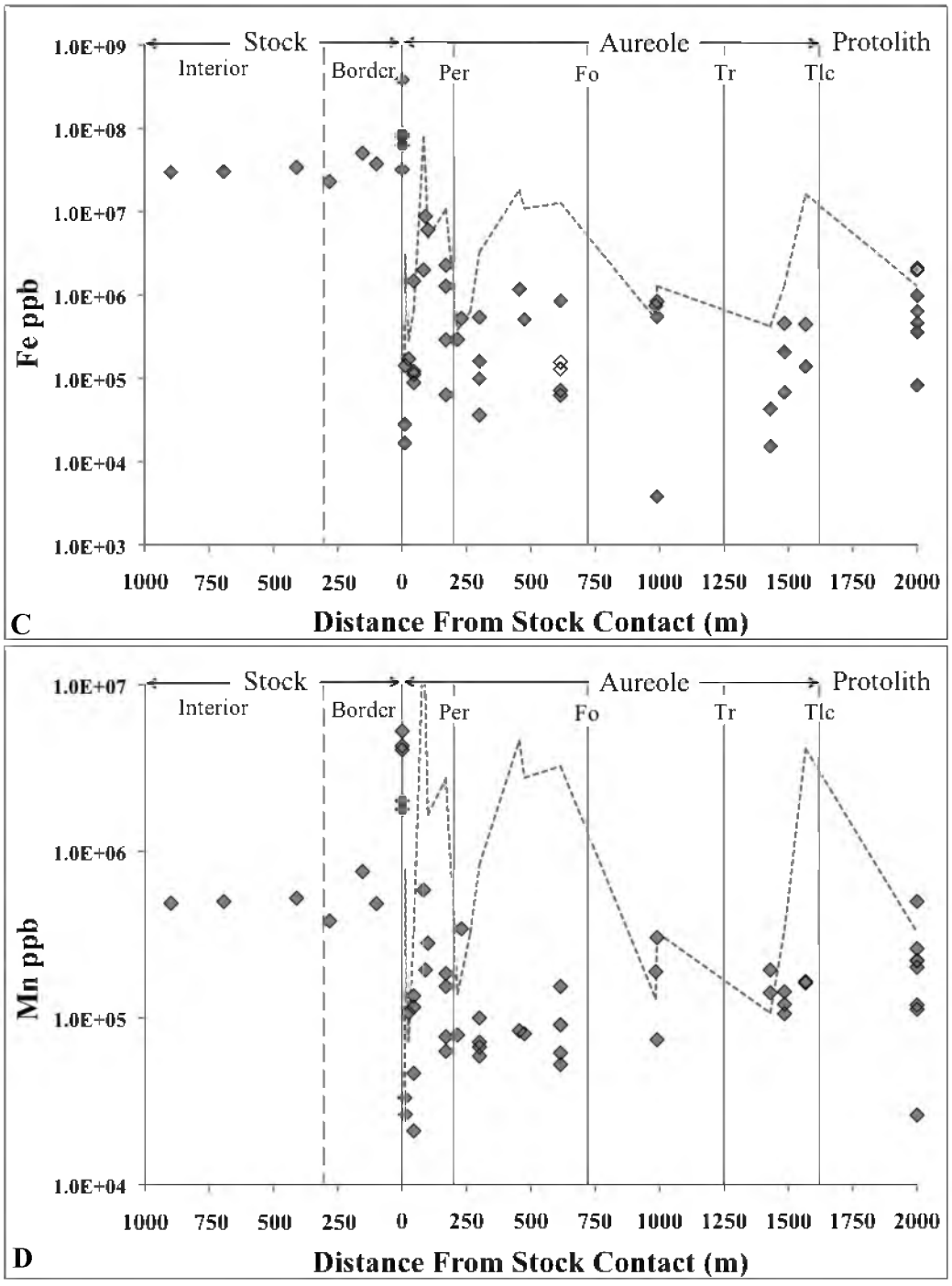

Figure 2-2 continued.

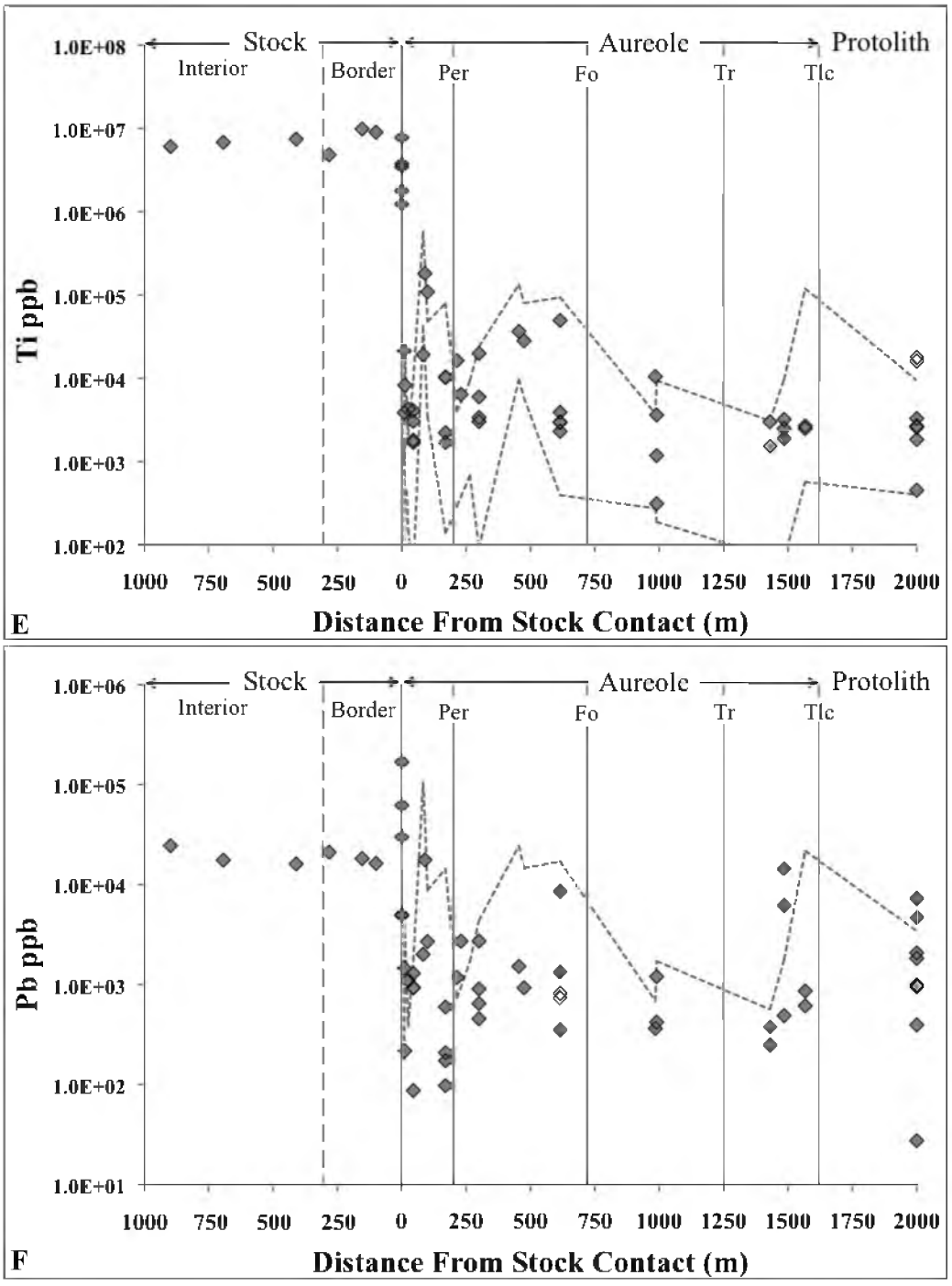

Figure 2-2 continued.

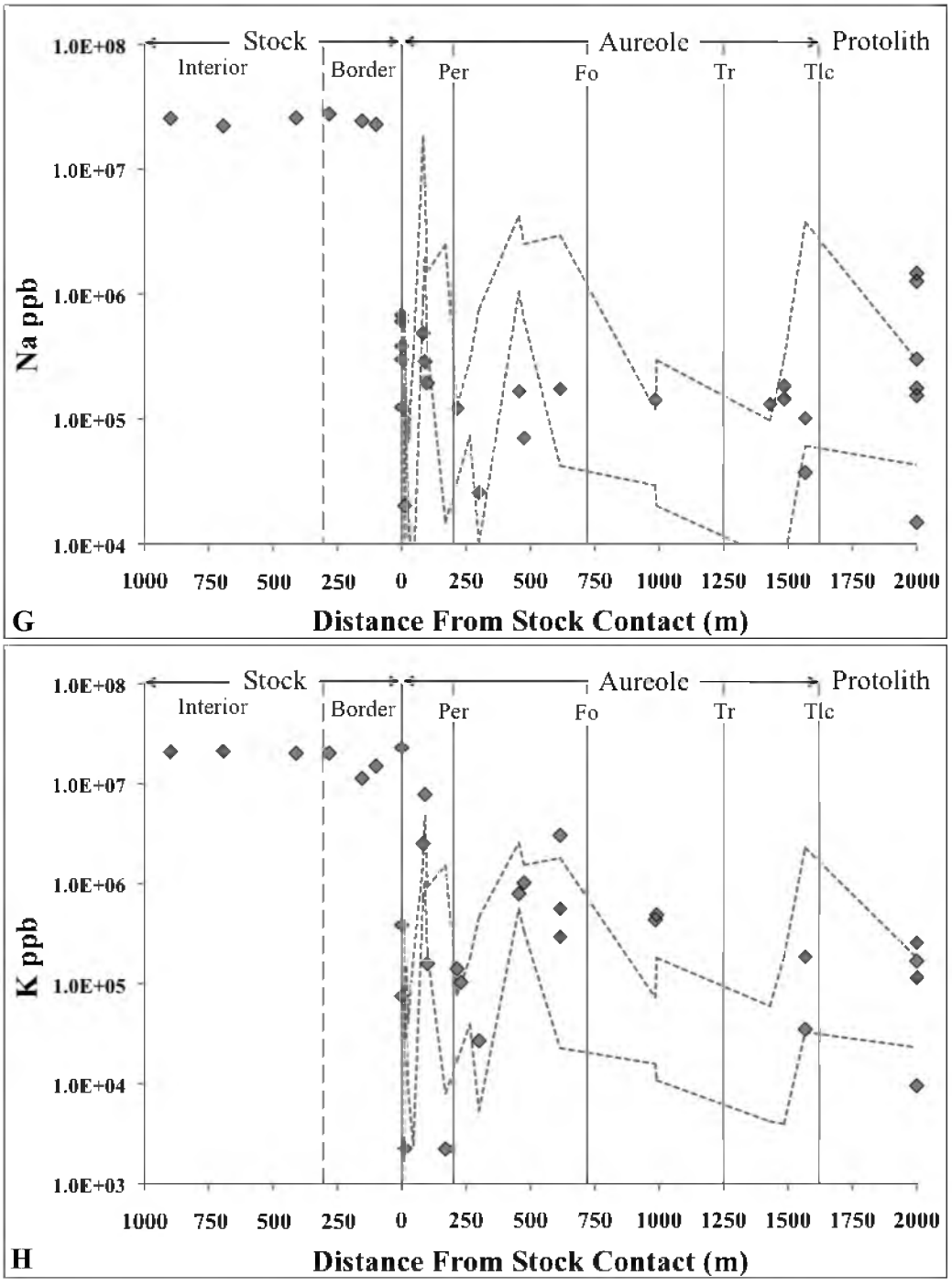

Figure 2-2 continued.

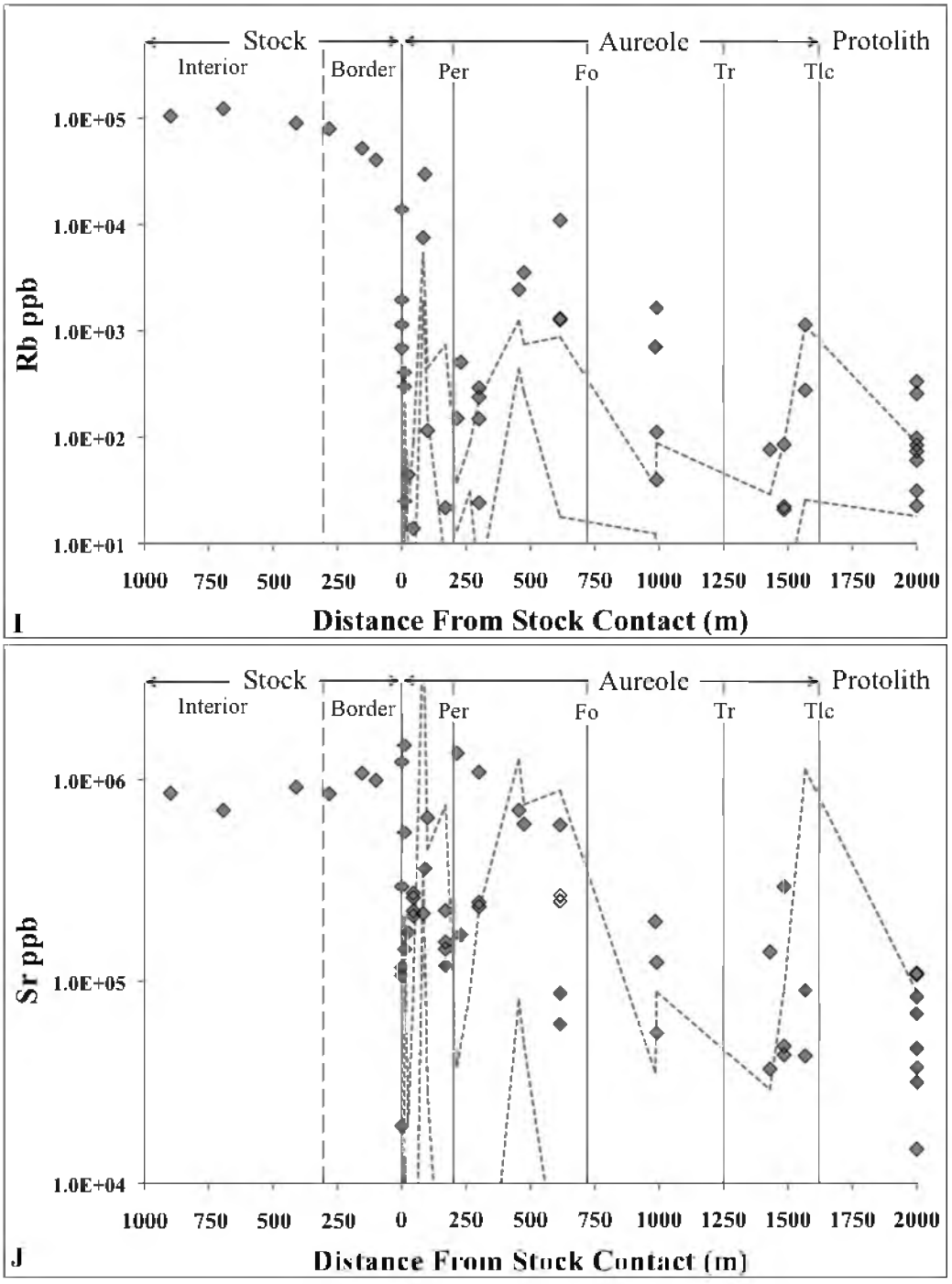

Figure 2-2 continued.

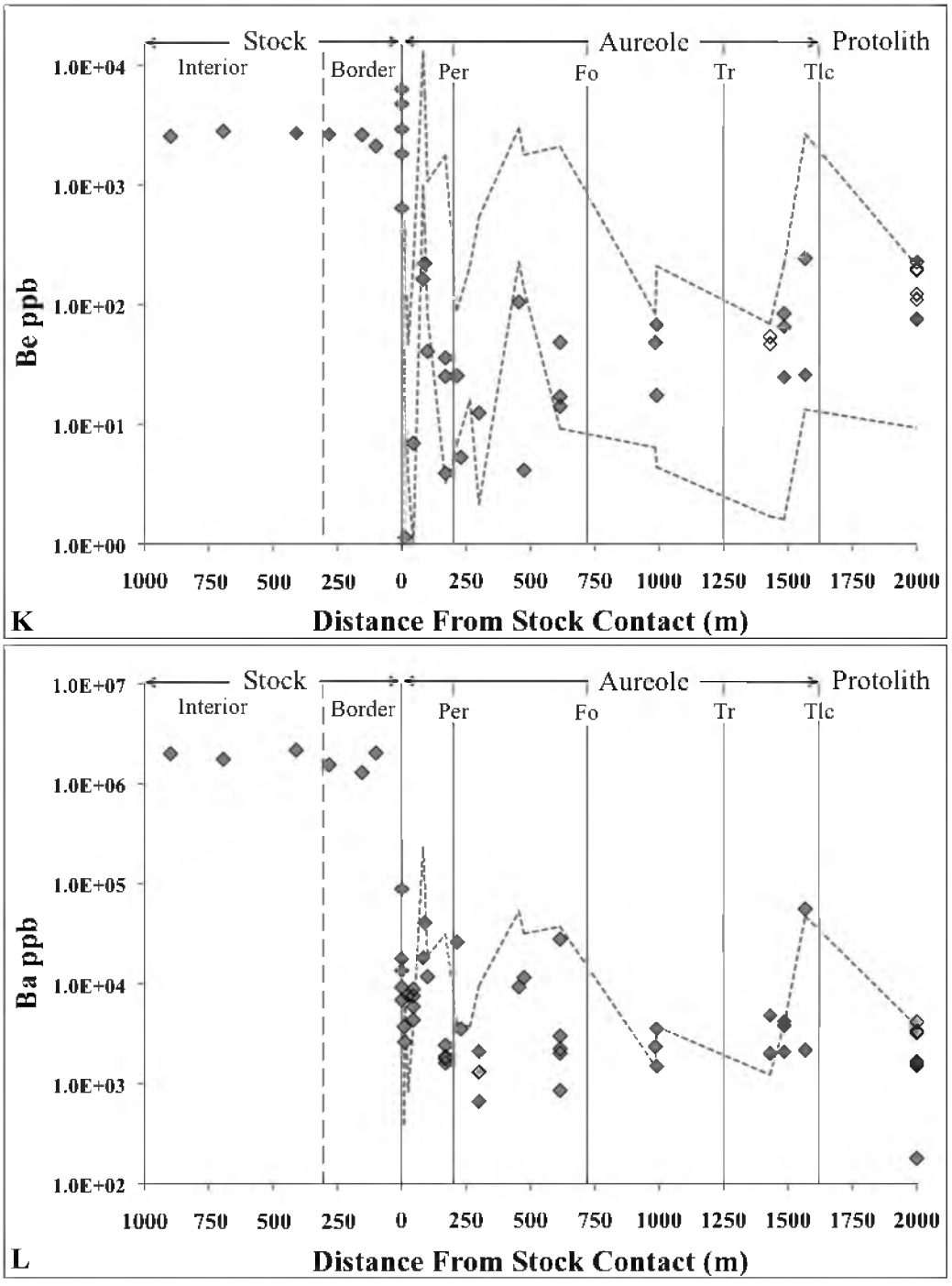

Figure 2-2 continued.

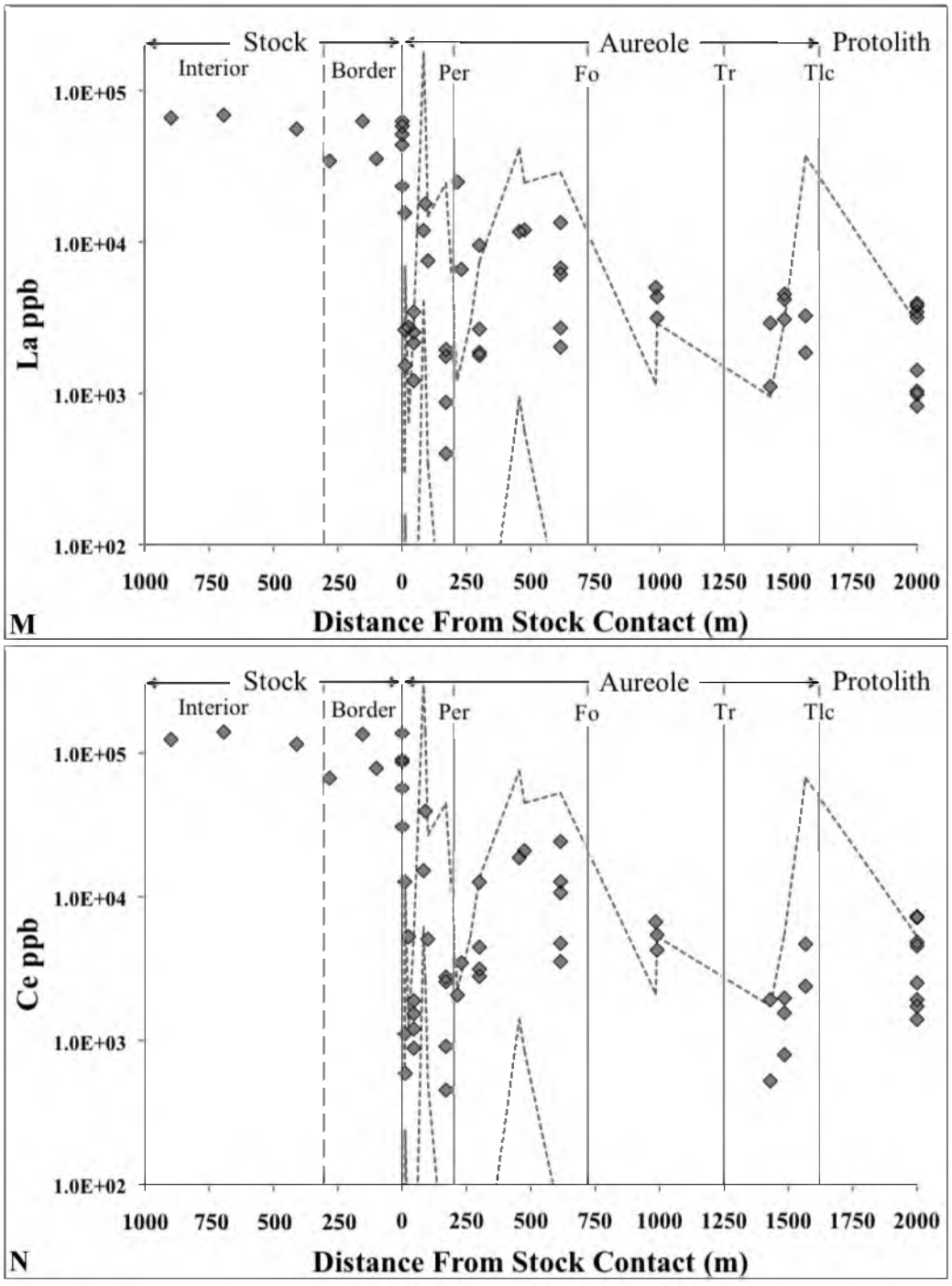

Figure 2-2 continued.

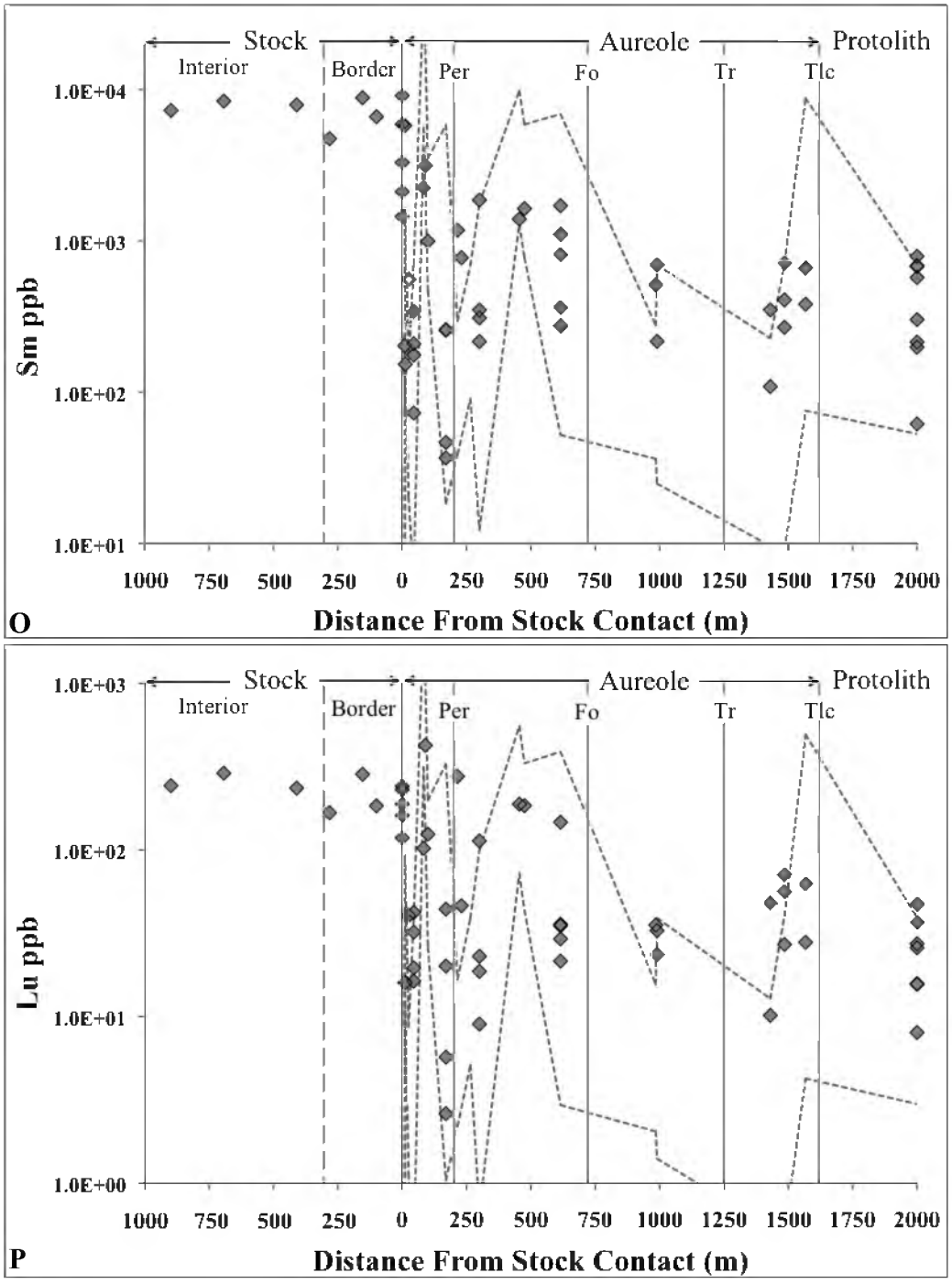

Figure 2-2 continued.

based on concentration variations throughout the system; while all analyzed elements are more abundant in the Alta Stock than in the non-metamorphosed protolith, concentration-distance profiles differ substantially between elemental groups.

Transition metal and Pb concentrations are shown in Figures 2-2a through 2-2f. These elements are generally characterized by an increase in concentration in the border phase of the Alta Stock relative to the central phase, with peak concentrations occurring in the skarns at the intrusive contact. Samples enriched in the metals Cu, Pb, and Zn over threshold values are found as far as 230 m and 100 m from the igneous contact for Cu and Pb, and for Zn, respectively. While the Cu anomaly is defined by a relatively high number of analyses registering concentration values above the threshold value, the Pb and Zn anomalies are more ambiguous, with a relatively small number of values above the threshold range. Beyond these distances, the concentrations of Cu, Pb, and Zn are at values within the threshold range. In contrast, concentrations of Fe, Mn, and Ti (Figure 2-2c and 2-2d) nearly always lie within the threshold range throughout the aureole (these elements are not enriched in the marbles of the aureole), and are only enriched in the skarns developed in marbles at the igneous contact. Since Al is implemented as a least mobile element, its threshold range cannot be defined and a concentration-distance profile for Al was not generated.

Alkali metals and alkaline earth metals (Figure 2-2) show more variable behavior than the transition metals and Pb, and three distinct patterns can be described for these elements. First, samples enriched in K, Rb, and Sr above threshold values are found as far as 1000, 1430, and 1480 m from the igneous contact, respectively. Sr concentrations reach a maximum in contact skarns relative to the Alta Stock and aureole, while the highest measured concentrations of Rb and K occur in the interior phase of the stock.

Neither Na nor Be are enriched in the aureole, and the greatest measured concentrations of these elements occur in the Alta Stock and in contact skarns, respectively. Ba is somewhat unique when compared to other alkaline earth elements. Ba concentrations in skarns are markedly lower than in the stock, but Ba is well above the threshold range in the marbles of the innermost aureole, and enrichment is observed up to a distance of approximately 40 m from the contact with the Alta Stock.

Rare earth element (REE) concentration-distance profiles are shown in Figure 2-2m through 2-2p. REE concentrations are elevated throughout the Alta Stock and contact skarns relative to the carbonate protolith, and the marbles are generally not enriched. La, however, is an exception in that samples with anomalous La enrichment are observed up to nearly 1000 m into the aureole.

2.3.4 Comparisons with Oxygen Isotope Data

Samples from the periclase and inner forsterite zones analyzed for both oxygen isotope ($\delta^{18}O_{Carbonate}$) and element concentration data are plotted in Figures 2-3a to 2-3p. In order to account for variations in un-metamorphosed protolith composition, the measured concentration value for a given element in each sample is normalized to the upper threshold value (median + 2MAD) for that element in the sample (i.e., measured concentration/upper threshold concentration). A grey dashed line is used to indicate where the measured concentration value is equal to the upper threshold concentration value (measured ppb/upper threshold ppb =1) in Figures 2-3a through 2-3p. Oxygen isotope analyses used for these plots are compiled in Appendix D. As a result of down-temperature fluid flow in the Alta aureole (Bowman et al., 1994; Cook et al., 1997), an oxygen isotope exchange front is developed 300-400 m from the igneous contact

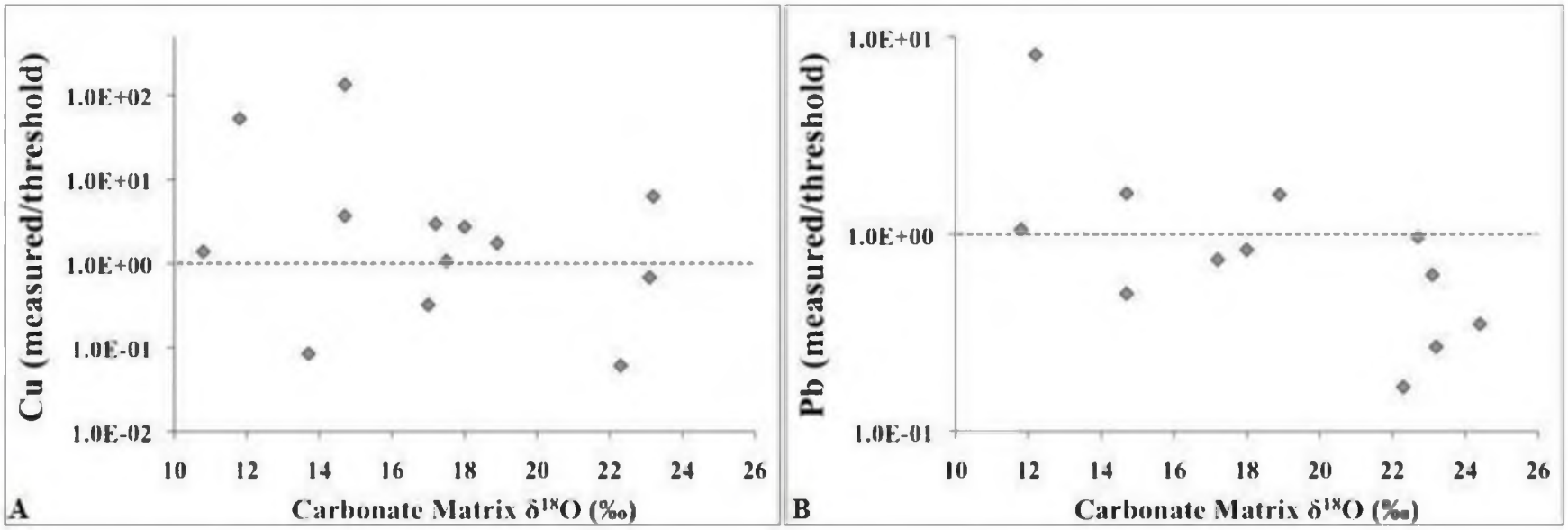

Figure 2-3. Ratios of measured concentration/upper threshold concentration (median protolith concentration + 2MAD) for trace elements plotted against $\delta^{18}O$ values for bulk carbonate in the samples. Only samples from the $^{18}O/^{16}O$-depleted zone (inner Fo zone and Per zone) are plotted. Samples beyond 400 m from the intrusive contact are not plotted because $\delta^{18}O$ values are not reliable monitors for fluid flux beyond this distance in the aureole. The dashed line at measured ppb/upper threshold ppb = 1 indicates the value at which the upper threshold value is equal to the measured value. Plots show $\delta^{18}O_{Carbonate}$ vs. **(A)** Cu, **(B)** Pb, **(C)** Fe, **(D)** Ti, **(E)** Mn, **(F)** Zn, **(G)** Na, **(H)** K, **(I)** Rb, **(J)** Be, **(K)** La, **(L)** Sm, **(M)** Ce, **(N)** Lu, **(O)** Sr, and **(P)** Ba.

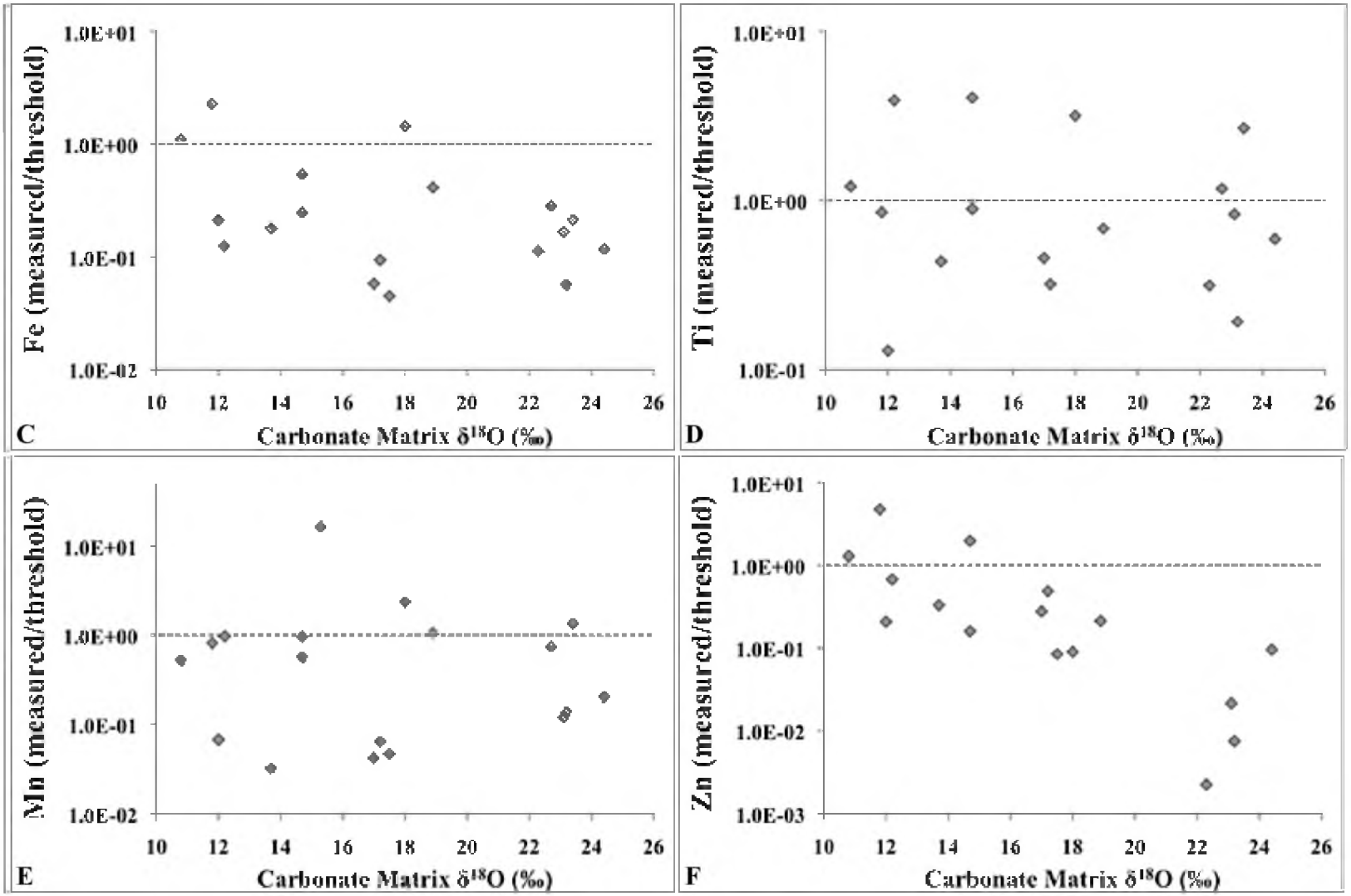

Figure 2-3 continued.

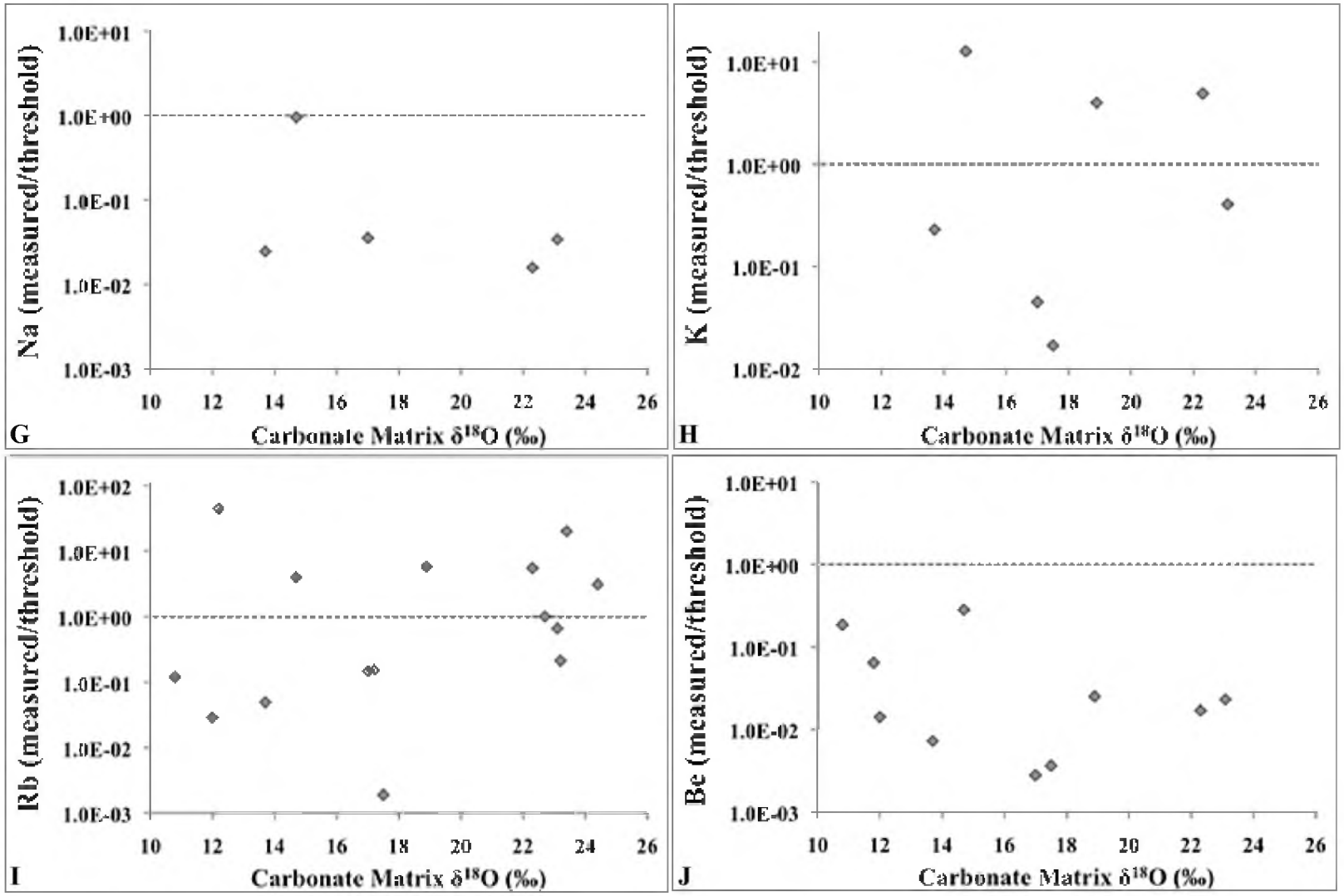

Figure 2-3 continued.

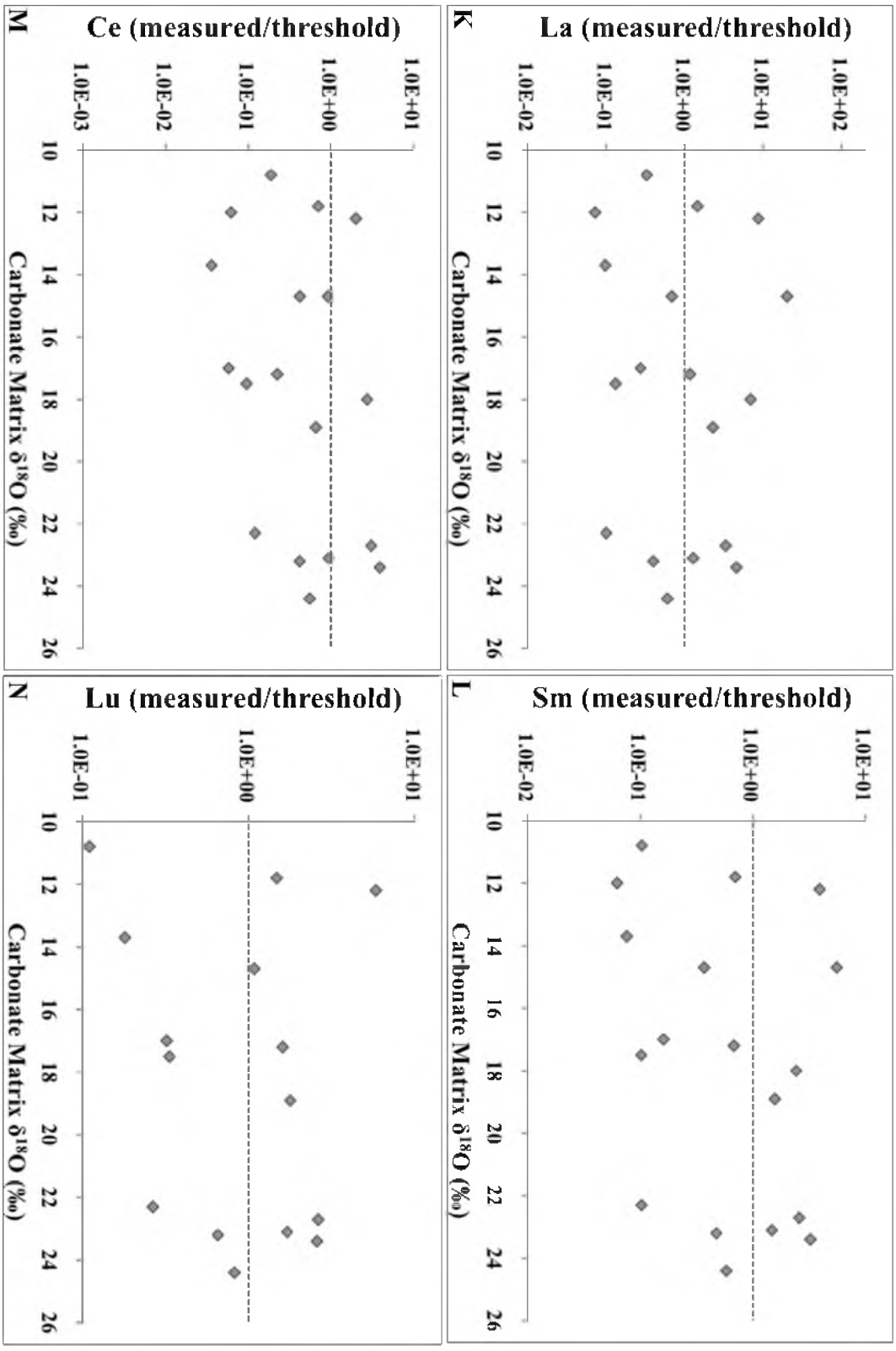

Figure 2-3 continued.

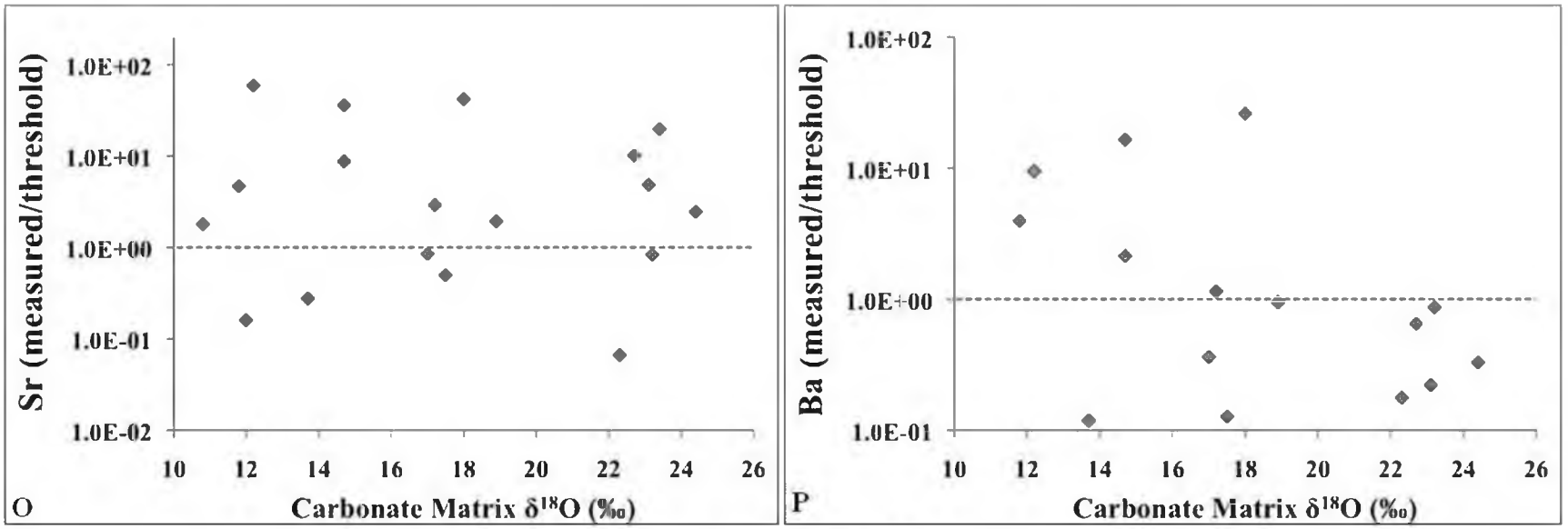

Figure 2-3 continued.

(Bowman et al., 1994). Alta aureole samples taken from the outer forsterite zone, tremolite zone, and talc zone are located well beyond (i.e., downstream from) this zone of $^{18}O/^{16}O$ depletion. These samples are therefore not plotted in Figures 2-3a through 2-3p because the $\delta^{18}O$ value of the carbonate matrix is no longer a reliable monitor for fluid flux beyond the oxygen isotope exchange front.

Transition metals showing positive anomalies in the marbles of the Alta aureole (Cu, Zn, and Pb) are generally characterized by a moderately strong negative correlation between the measured value/threshold value ratios and bulk carbonate $\delta^{18}O$ values (Figure 2-3a, 2-2b, and 2-2f) within the zone of $^{18}O/^{16}O$ depletion. The measured/threshold ratios for Fe, Mn, and Ti do not show significant correlation with $\delta^{18}O$ values (Figure 2-3c and 2-3e), but rather are fairly consistent regardless of the $\delta^{18}O$ value of the carbonate matrix. The measured/threshold ratios for alkali and alkaline earth metals are shown in Figures 2-3g through 2-3j and 2-3o through 2-3p. Barium, an element enriched in many of the marble samples from the inner aureole, is characterized by a modest negative correlation between the measured/threshold value ratios and the $\delta^{18}O_{carbonate}$ value. Conversely, while measured Sr, Rb, and K values are often greater than upper protolith threshold values, the concentrations of these elements do not correlate with $\delta^{18}O_{carbonate}$ values. Many Na analyses were below the detection limit, resulting in a relatively small number of data points, so it is uncertain if there is a correlation of Na with $\delta^{18}O_{carbonate}$. Be values do not correlate with $\delta^{18}O_{carbonate}$ in the inner aureole.

REE values are shown in Figure 2-3k through 2-3n. In every case, REE values do not correlate with the measured $\delta^{18}O_{carbonate}$ values in the forsterite and periclase zones of the Alta aureole.

2.4 Discussion

Mineralogical, geochemical, and isotopic alteration associated with contact skarn systems often delineates concentric zonation patterns in element concentrations around important hydrothermal fluid conduits (Meinert et al., 2005). Fluids derived from these conduits may be associated with the endowment of economically significant elements, and the integrated use of trace element and isotope data can therefore be useful in vectoring toward mineralized skarn deposits. Distal indicators of fluid-rock interaction are particularly useful in the exploration for mineralized skarn systems because they often define a substantially larger exploration target than the specific ore or calc-silicate zones, with many of these features reaching distances of more than 1,000 m from proximal skarn zones (Meinert et al., 2005). Such is the case for the aureole surrounding the small Cu-Pb-Zn skarns on the southern margin of the Alta Stock, with geochemical, oxygen isotope, and thermal alteration defining a zoning sequence surrounding the intrusive body.

The largest scale indicator of high-temperature fluid-rock interaction surrounding the Alta Stock is the mineralogic response of the siliceous dolomites to prograde metamorphism (heating). The extent of the thermal aureole, as indicated by the first appearance of talc (Tlc), extends to about 1600 m from the intrusive contact, and marks the limit of alteration (visible or otherwise) associated with the intrusion. Furthermore, phase equilibria show that the observed prograde metamorphic sequence of talc-tremolite-forsterite-periclase toward the igneous contact is a product of both increased temperature and infiltration of reactive (e.g., H_2O-rich) fluids (Moore and Kerrick, 1976). This spatial sequence of mineral zonation is therefore a vector of increasing temperature that points to the Alta Stock as the source of both heat and fluids in the Alta system (see

Cook and Bowman, 1994; 2000).

The infiltration of these H_2O-rich and low $\delta^{18}O$ fluids from the Alta Stock has also produced an extensive zone of $^{18}O/^{16}O$ depletion in the carbonate wallrocks up to approximately 400 m from the intrusive contact with the Alta Stock (Bowman et al., 1994; Cook et al., 1997). The spatial patterns of this $^{18}O/^{16}O$ depletion at the aureole scale and within single outcrops in the periclase zone demonstrate that fluid flow was laterally away from the Alta Stock and largely bedding-concordant (Bowman, et al., 1994; Cook et al., 1997). Within the upflow, $^{18}O/^{16}O$ depleted zone (the H_2O-dominated segment of the flowpath), equivalent to the Per and inner Fo zones (the inner Alta aureole), the $\delta^{18}O$ value of the carbonate matrix reflects relative fluid flux, with lower $\delta^{18}O$ marbles resulting from greater fluid flux (Bowman et al., 1994, 2009). Therefore, the concentration of elements that are mobile in these hydrothermal fluids (those showing concentration anomalies in the marbles of the aureole) should maintain a systematic relationship with the degree of $^{18}O/^{16}O$ depletion in marbles within the zone of $^{18}O/^{16}O$ depletion (oxygen isotope alteration). This, in fact, is the case for the Alta aureole, where the normalized concentrations (element/Al ratio) of many elements show negative correlations with $\delta^{18}O$ values of the carbonate host rock.

Cu, Pb, Zn, and Ba, are all enriched in samples at varying distances within the Alta aureole (Figure 2-2) and are all negatively correlated with $\delta^{18}O$ values of the carbonate matrix for samples located within the zone of $^{18}O/^{16}O$ depletion (Figure 2-3). The correlation between high measured value/upper threshold value ratios and lower $\delta^{18}O$ values of carbonate matrix supports the interpretation that the measured Cu, Zn, Pb, and Ba values are above the protolith threshold range and define true positive concentration anomalies. This relationship between the extent of fluid infiltration based on $^{18}O/^{16}O$

depletion and anomalous metal concentrations suggests that mineralizing fluids are the source for the measured metal enrichments rather than false positive anomalies resulting from passive enrichment of these metals. This observation is particularly important for Pb and Zn because their positive concentration anomalies are less extensive (a smaller number of analyses fall above the protolith threshold range) than those observed for Cu, Ba, and Sr. The combined use of oxygen isotope and element concentration data therefore provides stronger evidence supporting Pb and Zn additions to aureole rocks than the use of concentration data alone.

Fe and Mn are concentrated in the border phase of the Alta Stock and particularly in contact skarns relative to the central phase of the Alta Stock granodiorite and marbles of the aureole. The elevated concentration of these elements at the intrusive contact suggests that they, like Cu, Pb, and Zn, were mobilized through fluid-rock interaction at high temperatures within the border phase of the Alta Stock (John, 1989; Bowman et al., 1994; Cook et al., 1997) and incorporated into the skarn-forming fluids. However, neither Fe nor Mn show elevated concentrations in marbles of the inner aureole, and there is no correlation between measured oxygen isotope values and the Fe and Mn concentrations in the marble samples. This observation may be explained by the mineralogy of the skarns. The dominant skarn minerals, which readily incorporate Fe and Mn, are grandite series garnet, pyroxene, actinolite, epidote, magnetite, and pyrite (Cook, 1982). Crystallization of skarn minerals may have effectively exhausted the Fe and Mn supply of the skarn fluids before these fluids infiltrated to any significant distance into the marbles of the aureole. Furthermore, Root et al. (2012) show that skarn garnet and pyroxene (and ludwigite in Per marbles) become progressively depleted in Fe away from the igneous contact. This zoning supports strong partitioning of Fe into

minerals relative to fluid, therefore providing an effective means (formation of skarn minerals) of removing Fe from the fluid.

Samples enriched in K, Sr, and Rb over threshold values are found as far as 1000, 1480, and 1430 m from the intrusive contact with the Alta Stock, respectively. However, concentration values for these elements do not correlate with $\delta^{18}O$ values of carbonate matrix. Sr concentrations increase from the interior of the stock toward the intrusive contact and reach a maximum in contact skarns relative to the Alta Stock and aureole. This enrichment suggests that Sr was preferentially incorporated into skarn forming fluids relative to igneous mineralogy, and this interpretation is further supported by the presence of marble samples enriched in Sr within the aureole.

In contrast to Sr, K and Rb concentrations in skarn samples are generally low when compared to the border phase of the stock, and are also low relative to many marble samples throughout the aureole. The dominant skarn minerals (garnet and pyroxene) do not readily accept alkali metals, and the low measured concentrations of K and Rb in skarn samples reflect this behavior. However, K and Rb are often enriched in the marble samples of the aureole, where the dominant mineralogy (carbonate) similarly does not accept large amounts of alkali metals. This observation may be partly explained by the behavior of these elements in the border phase of the Alta Stock.

K and Rb concentrations decrease from the peaks observed in the central phase of the Alta Stock as the contact with the carbonate wallrock is approached (in the border phase of the stock). This suggests that these elements are removed (leached) from the border phase by the infiltration of H_2O-rich hydrothermal fluids at high temperatures. In this case, the infiltrating fluid would become increasingly enriched in these elements as the contact with the carbonate wallrock is approached. As the crystallizing skarn

minerals are largely ineffective in removing these elements from infiltrating fluids, it is likely that the fluid would retain its high K and Rb concentrations as it infiltrated into the aureole. This process could ultimately result in K and Rb enrichments in the aureole, where lower temperatures (compared to the stock and the intrusive contact) would promote partitioning of these elements into the solid phases (carbonate and accessory phlogopite).

Na is characterized by low concentrations in contact skarn samples. However, in contrast to other alkali metals (K and Rb), Na is not enriched in the marbles of the Alta aureole and Na concentrations remain relatively constant across both the central and border phases of the Alta Stock. The high concentrations of Na in the Alta Stock suggest that it is likely to be abundant in skarn/metamorphic fluids. However, the lack of Na enrichment in marble samples confirms that the carbonate and phlogopite minerals do not accept Na to a significant degree. This is in contrast to the measured enrichment of other alkali metals (K and Rb) in many marble samples.

Rare earth elements (REE) (excluding La) and Ti are largely homogeneous in concentration throughout the aureole, exhibit no measureable enrichment above threshold values and are not correlated with $\delta^{18}O$ values of carbonate matrix within the zone of $^{18}O/^{16}O$ depletion. While this lack of aureole enrichment is similar to that seen for Fe and Mn, the behavior of REE's (excluding La) and Ti in the Alta Stock and its associated skarns is distinct. Unlike Fe and Mn, REEs and Ti tend to be fairly consistent in concentration between both phases of the intrusion and in the contact skarns, which suggests that these elements were not mobilized to any significant degree by the skarn forming fluids. This interpretation is further supported by their lack of enrichment in either skarns or marbles in the aureole.

La, however, is an exception to the other REEs. La is enriched over protolith values in marble samples up to nearly 1000 m from the intrusive contact. This La behavior is in contrast to that described by Escalante et al. (2010) for the Antamina skarn system, where La is demonstrated to be an immobile element in limestone and marble host rocks. The correlation between La and Al in the Alta system is substantially weaker than that observed between Al and other low-solubility elements (Ti, Ce, and Lu, for example). Because enrichment is demonstrated for La in the Alta aureole (Figure 2-2e), Al was considered to be a preferable choice when considering the least mobile element used for threshold determinations in this study.

The results presented in this study demonstrate that integrated isotopic, mineralogical, and trace element data have potential applications in the exploration for economically significant skarn deposits and other intrusion-centered, carbonate-hosted metallic deposits. This approach may be particularly useful when considering a blind deposit, in which visible indicators of fluid-rock interaction may not show surface expressions. The identification of geochemical anomalies using threshold ranges defined by the median host rock ± 2MAD value normalized to a least mobile element (Al) has been demonstrated to be effective both in this study and by Escalante et al. (2010). Furthermore, combined trace element and oxygen isotope data may increase confidence in identifying anomalies where trace element data alone is somewhat ambiguous, as the correlation of $^{18}O/^{16}O$ depletion and increased metal concentration suggests the presence of true positive outliers resulting from fluid infiltration into the carbonate host rock. Although the utility of isotopic data in exploration has been suggested by numerous studies, stable isotope data is not generally collected in mineral exploration due to the high cost of analyses and relatively slow speed of data collection (Barker et al., 2013).

However, with continually advancing analytical techniques, it is likely that future oxygen isotope data will be collected more rapidly and inexpensively than at present, and therefore, the integration of trace element and isotopic data will likely become increasingly important in the exploration for mineral deposits in the future.

APPENDIX A

QEMSCAN PROCEDURES AND SCAN IMAGES

Forsterite textures were measured in two-dimensions (2-D) using the QEMSCAN (Quantitative Evaluation of Minerals by Scanning electron microscopy) instrument in the Department of Geology and Geophysics at the University of Utah. All forsterite textural data were collected using the field image analysis tool in the QEMSCAN iMeasure 4.3 software. To evaluate the resolution required for accurate determination of Fo textural characteristics, sample 11-III-A-1-1 was measured in three trial runs at varying resolutions (10, 20, and 30 μm analysis spacing), and the data were compared across runs. From the comparison, the 20 μm field spacing was determined to be sufficiently accurate in representing the forsterite abundance and textural data because it yielded nearly identical results to the 10 μm field spacing, and was therefore implemented for all analyses. This scan step interval allows for reliable inventory of Fo grains 20μm in diameter or larger; smaller grains may not be reliably detected with this field spacing. Scan areas were typically 10 mm x 10 mm areas, although rectangular scans were implemented when advantageous (i.e., in situations where a square scan would incorporate vein material or part of another domain). All field images are included in this appendix. Each field image was subjected to a series of processors in the QEMSCAN iDiscover 4.3 software package before quantitative Fo data were gathered. First, a field

stitch was applied to generate one continuous image from the individual segments generated by the field image surface analysis. The boundary phase processor was then implemented. This processor is particularly useful in resolving edge effects, where a single pixel spanning the boundary between two phases is mistakenly identified as a mineral with an intermediate composition between the two phases. In these cases, the boundary phase processor will assign the individual pixel to one of the surrounding minerals, depending on which has the greatest area of contact with the pixel. In order to separate touching grains of the same composition, the touching particles processor was applied. This processor is necessary because the iDiscover image analysis will otherwise identify touching but distinct grains as one single crystal, thus resulting in an inaccurate calculation of number of Fo grains, average Fo grain size, and average Fo grain area. The final resulting image was then compared with the original thin section using a petrographic microscope to verify results of the QEMSCAN analyses and to correct by hand touching, but distinct grains not separated by the touching particles processor.

Some outer Fo zone samples contain relatively small numbers of large grains characterized by skeletal margins consisting of optically continuous but physically isolated (in 2D) grains (Sample 88-20, for example). Additional corrections were required to connect these optically continuous, but nontouching grain segments or to separate touching sets of grains not corrected by the touching particles processor. To perform these additional corrections, QEMSCAN images were converted to binary black and white images (with all phases other than Fo appearing as white) using NIH Image software. Fo grains were separated or connected as necessary in the image by comparison with the same area in thin section using the petrographic microscope. The corrected image was then analyzed using *NIH Image* to obtain final quantitative textural

data. *NIH Image* is a public domain program developed by the U.S. National Institute of Heath and is available online at http:/rsb.info.gov/nih-image.

Corrected field images were used to determine the average Fo grain size and grain length, and number of forsterite crystals per unit area (N_A) in each sample with the QEMSCAN software. The N_A value was used to calculate the number of Fo crystals per unit volume (cm^3), N_V, of the sample using equation A-1 (after Wagner, 1961; Kirkpatrick, 1977; Cashman and Ferry, 1988).

$$N_v = (N_A)^{1.5} \tag{A-1}$$

While more elaborate conversions have been proposed to calculate N_V (Saltykov, 1967; DeHoff, 1986), Cashman and Ferry (1988) found that these methods accumulate errors in samples dominated by either large or small crystal size classes. Qualitative analysis of samples in this study showed that many samples are dominated by either many small crystals or few large grains. As a result, the Wagner (1961) method (equation A-1) was selected for the calculation of N_V. N_V was then used to calculate the Fo crystals/mol Fo value by equation A-2, where X_{Fo}^{vol} is the modal abundance (volume %) of Fo in the sample determined by QEMSCAN analysis, w_{Fo} is the molecular weight of Fo (140.69 g/mol), and ρ_{Fo} is the density of Fo (3.25 g/cm^3):

$$\frac{\text{Crystals}_{Fo}}{\text{mol}_{Fo}} = N_v \frac{1}{\left(\frac{\rho_{Fo}}{w_{Fo}}\right) X_{Fo}^{Vol}} \tag{A-2}$$

Sample: 12-1b

QEMSCAN Field Image Location(s):

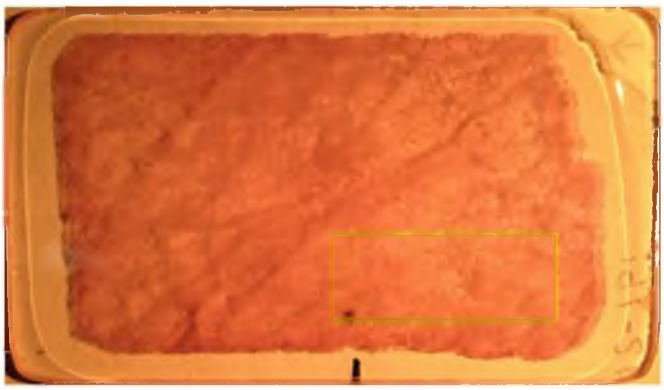

QEMSCAN Field Image(s):

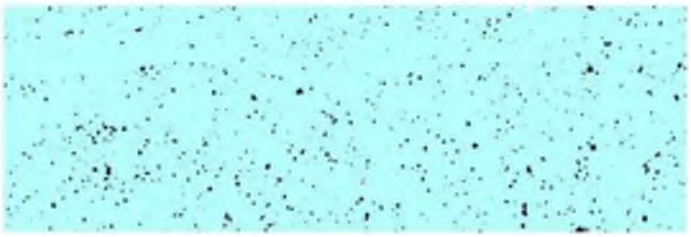

1 cm

Scan 1 Mineralogy:
Calcite: 97.6%
Dolomite: 0.6%
Forsterite: 1.7%
Pyrite: 0.01%
Micas: 0.00%

Sample: 23-Bii

QEMSCAN Field Image Location(s):

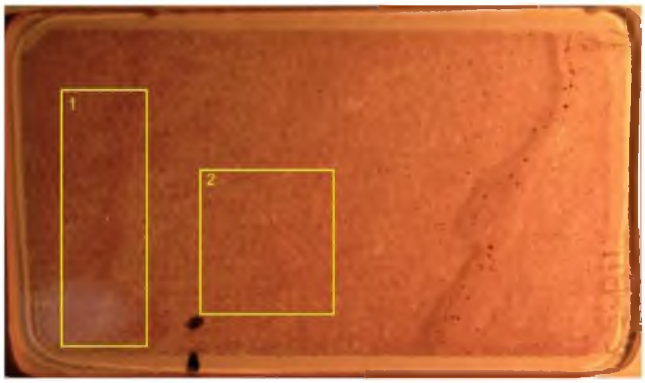

QEMSCAN Field Image(s):

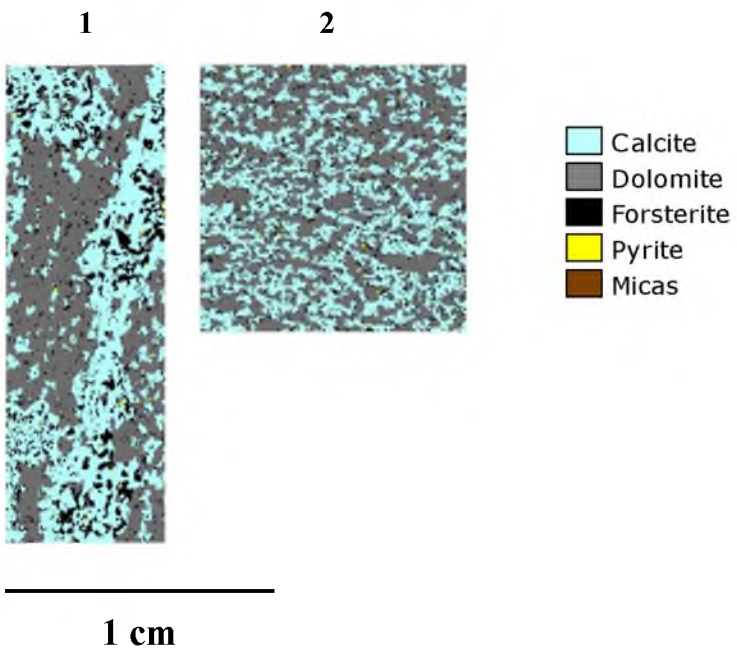

Scan 1 Mineralogy:
Calcite: 43.1%
Dolomite: 43.5%
Forsterite: 12.9%
Pyrite: 0.18%
Micas: 0.00%

Scan 2 Mineralogy:
Calcite: 41.5%
Dolomite: 49.3%
Forsterite: 8.7%
Pyrite: 0.18%
Micas: 0.00%

Sample: 88-8

QEMSCAN Field Image Location(s):

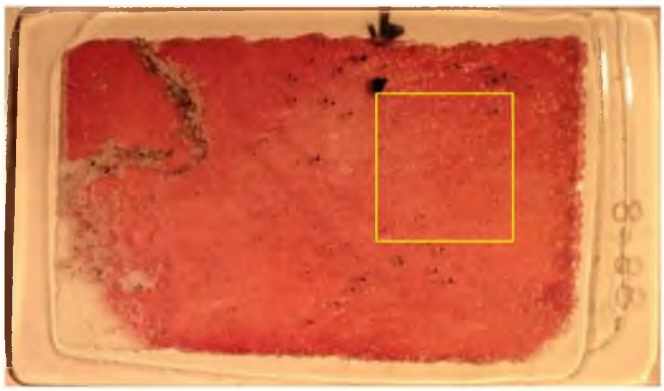

QEMSCAN Field Image(s):

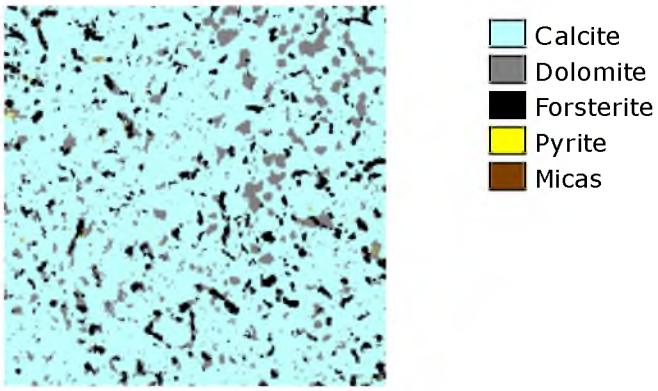

1 cm

Scan 1 Mineralogy:
Calcite: 81.5%
Dolomite: 10.2%
Forsterite: 7.2%
Pyrite: 0.06%
Micas: 0.08%

Sample: 88-20

QEMSCAN Field Image Location(s):

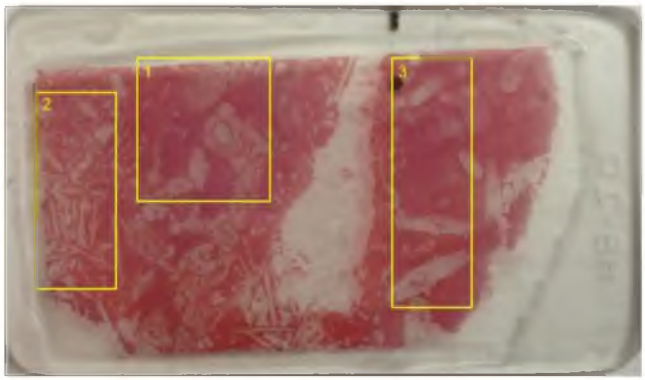

QEMSCAN Field Image(s):

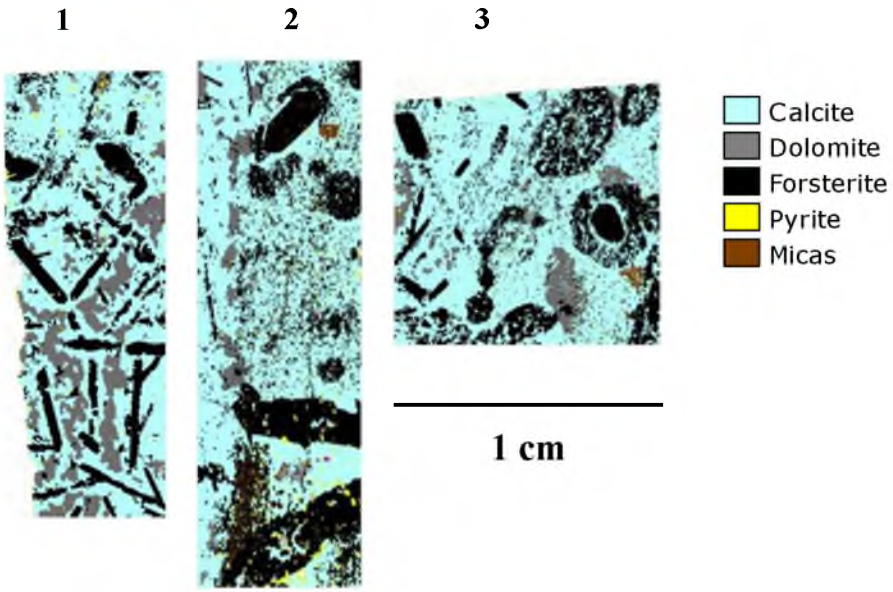

Sample: 88-60

Scan 1 Mineralogy:	**Scan 2 Mineralogy:**	**Scan 3 Mineralogy:**
Calcite: 61.2%	Calcite: 56.3%	Calcite: 58.3%
Dolomite: 6.0%	Dolomite: 16.0%	Dolomite: 4.4%
Forsterite: 29.6%	Forsterite: 23.6%	Forsterite: 32.2%
Pyrite: 0.73%	Pyrite: 2.1%	Pyrite: 2.0%
Micas: 1.1%	Micas: 0.12%	Micas: 2.4%

QEMSCAN Field Image Location(s):

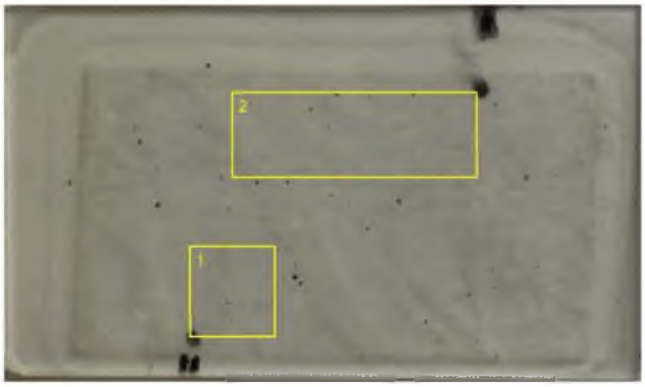

QEMSCAN Field Image(s):

1 **2**

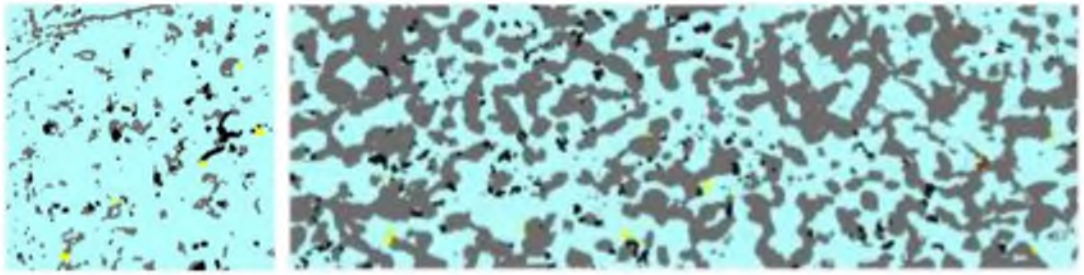

1 cm

Calcite
Dolomite
Forsterite
Pyrite
Micas

Scan 1 Mineralogy:
Calcite: 86.8%
Dolomite: 9.5%
Forsterite: 2.9%
Pyrite: 0.30%
Micas: 0.20%

Scan 2 Mineralogy:
Calcite: 53.0%
Dolomite: 43.9%
Forsterite: 2.6%
Pyrite: 0.20%
Micas: 0.11%

Sample: 88-C5

QEMSCAN Field Image Location(s):

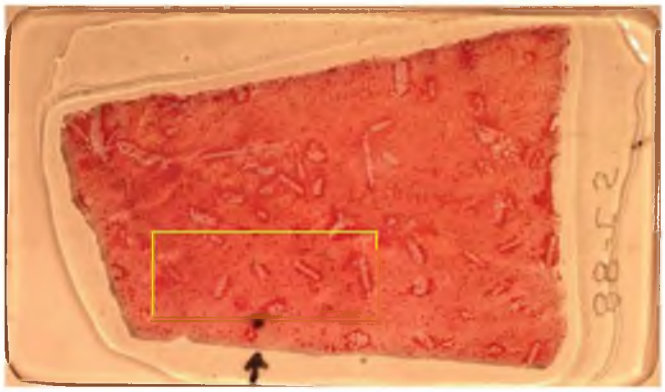

QEMSCAN Field Image(s):

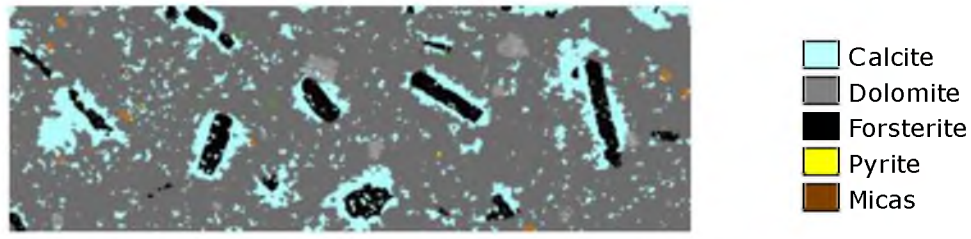

1 cm

Scan 1 Mineralogy:
Calcite: 15.7%
Dolomite: 76.1%
Forsterite: 5.3%
Pyrite: 0.03%
Micas: 0.46%

Sample: 94I-9-2-4

QEMSCAN Field Image Location(s):

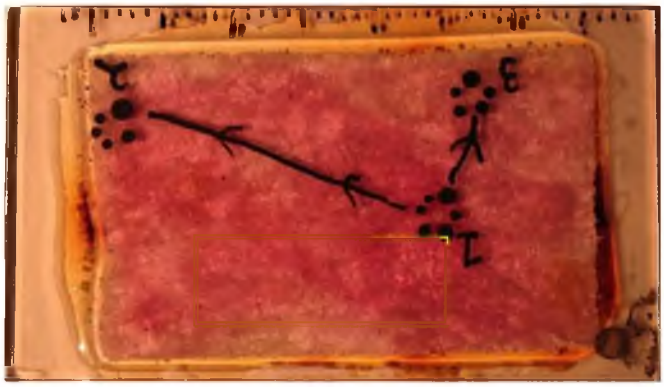

QEMSCAN Field Image(s):

1 cm

Scan 1 Mineralogy:
Calcite: 95.2%
Dolomite: 0.0%
Forsterite: 4.7%
Pyrite: 0.0%
Micas: 0.0%

Sample: 94I-9-2-a

QEMSCAN Field Image Location(s):

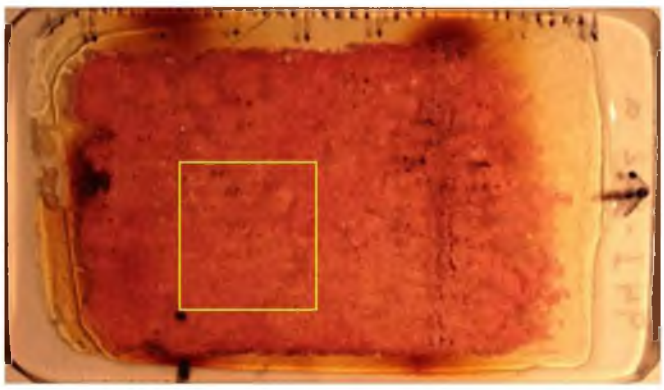

QEMSCAN Field Image(s):

1

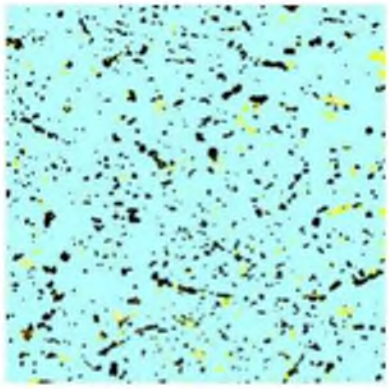

Calcite
Dolomite
Forsterite
Pyrite
Micas

1 cm

Scan 1 Mineralogy:
Calcite: 91.0%
Dolomite: 0.0%
Forsterite: 7.1%
Pyrite: 1.6%
Micas: 0.32%

Sample: 99V-3

QEMSCAN Field Image Location(s):

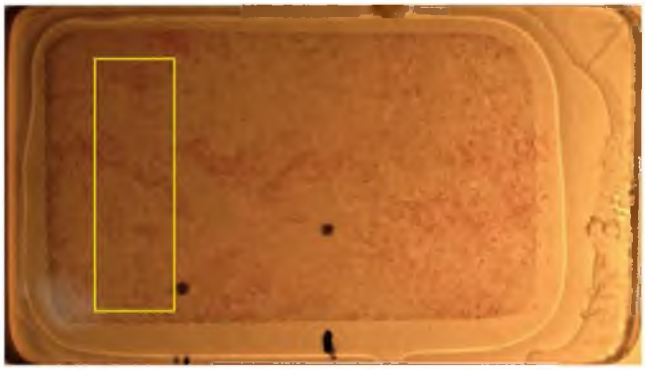

QEMSCAN Field Image(s):

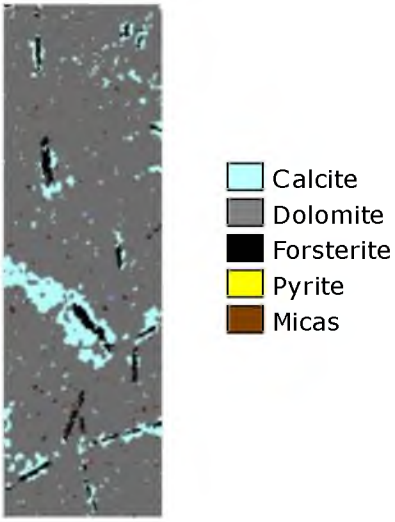

1 cm

Scan 1 Mineralogy:
Calcite: 9.6%
Dolomite: 86.4%
Forsterite: 2.7%
Pyrite: 0.01%
Micas: 0.62%

Sample: 11-III-A-1-1

QEMSCAN Field Image Location(s):

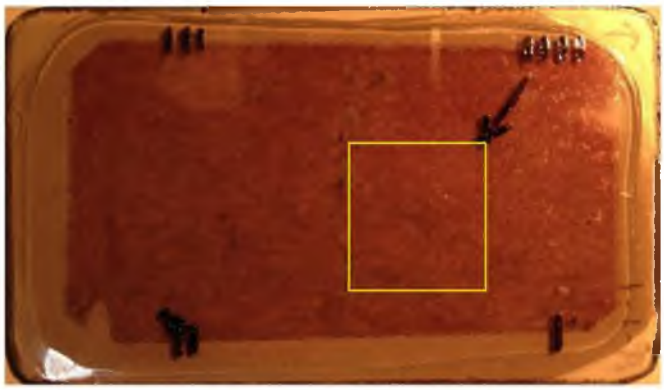

QEMSCAN Field Image(s):

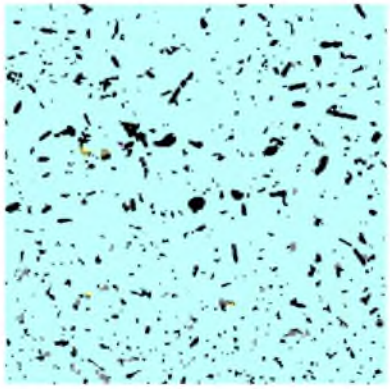

1 cm

Scan 1 Mineralogy:
Calcite: 92.7%
Dolomite: 1.1%
Forsterite: 5.7%
Pyrite: 0.05%
Micas: 0.00%

Sample: 11-III-A-3-1

QEMSCAN Field Image Location(s):

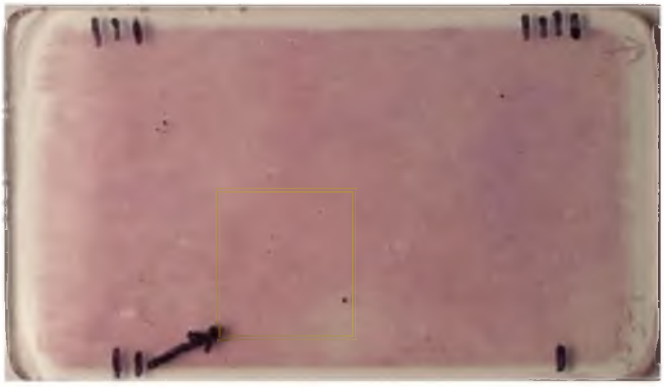

QEMSCAN Field Image(s):

1

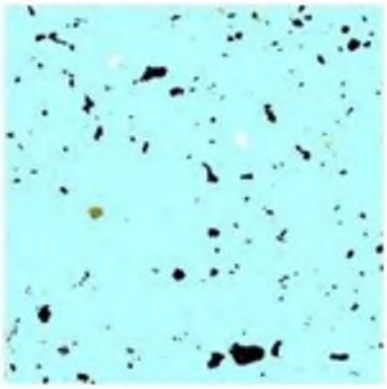

1 cm

Scan 1 Mineralogy:
Calcite: 96.7%
Dolomite: 0.3%
Forsterite: 2.7%
Pyrite: 0.02%
Micas: 0.02%

Sample: 11-III-B-8-3A

QEMSCAN Field Image Location(s):

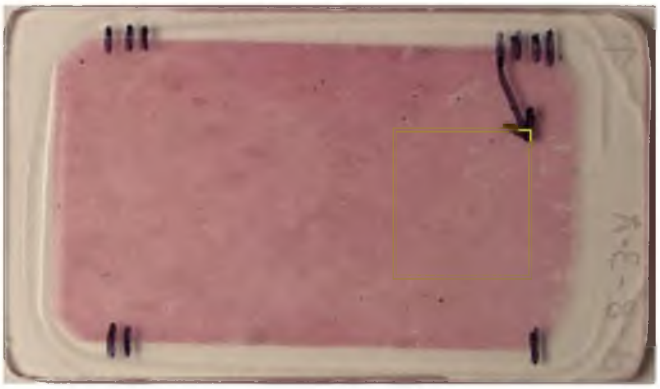

QEMSCAN Field Image(s):

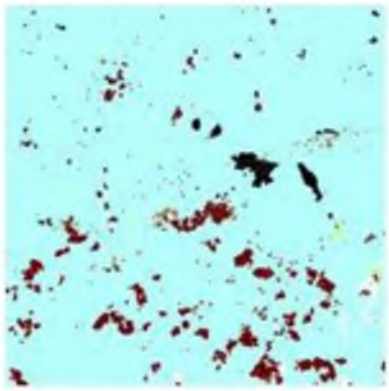

1 cm

Scan 1 Mineralogy:
Calcite: 93.4%
Dolomite: 0.06%
Forsterite: 1.1%
Pyrite: 0.10%
Micas: 4.7%

Sample: 02-FZ9-18

QEMSCAN Field Image Location(s):

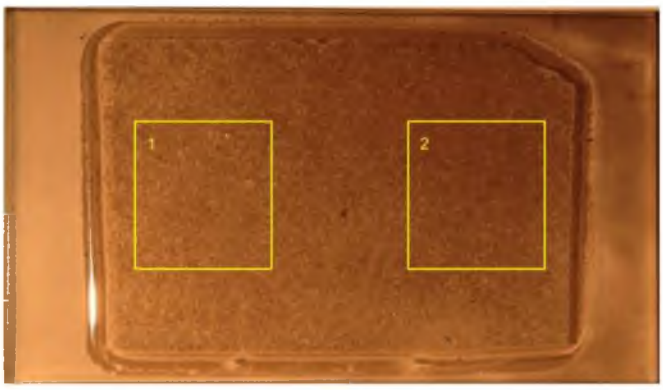

QEMSCAN Field Image(s):

1 **2**

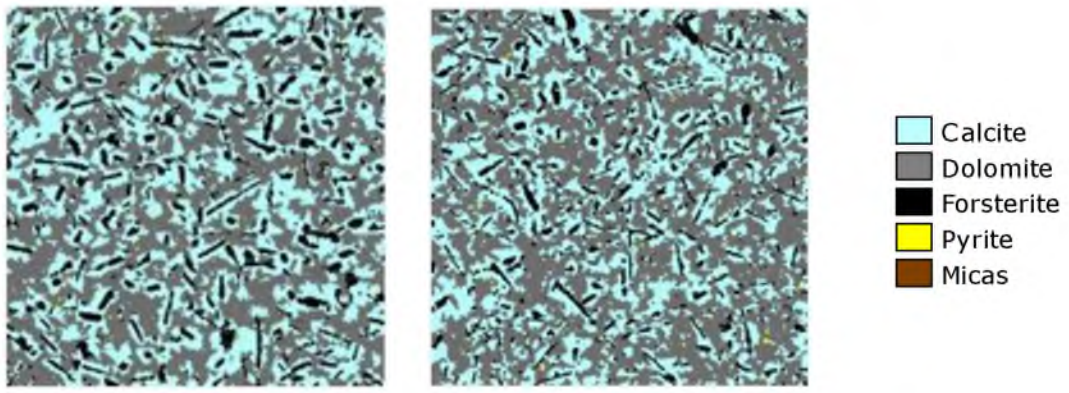

1 cm

Scan 1 Mineralogy:	**Scan 2 Mineralogy:**
Calcite: 41.7%	Calcite: 37.6%
Dolomite: 45.0%	Dolomite: 51.3%
Forsterite: 11.6%	Forsterite: 9.4%
Pyrite: 0.27%	Pyrite: 0.32%
Micas: 0.18%	Micas: 0.11%

APPENDIX B

PREPARATION OF FORSTERITE SEPARATES FOR ANALYSES

Additional slabs were cut from each sample and divided into 3-5 cm^3 cubes, which were then treated with a 1M HCl solution to dissolve the carbonate matrix. The insoluble material (mostly Fo with minor but variable amounts of sulfide and phlogopite) was cleaned and sieved into five different crystal size fractions (>853 μm, 853-420 μm, 420-178 μm, 178-106 μm, and 106-75 μm). Sulfide minerals were removed by hand-picking in most cases, particularly in samples were sulfides were abundant.

Olivine is vulnerable to replacement by serpentine (Srp) during retrograde hydrothermal alteration, especially along fractures (Wicks et al., 1977). Care was taken to collect minimally weathered samples in the field and to avoid areas within samples affected by retrograde alteration when selecting material for the preparation of Fo separates. Nevertheless, some degree of serpentinization was present in nearly every sample. As serpentine is likely a result of the interaction of olivine with retrograde, potentially isotopically distinct fluids, it is necessary to remove Srp by HF treatment to obtain an accurate $\delta^{18}O$ analysis of forsterite.

As Srp tends to be preferentially associated with fractures within forsterite grains in these samples, it was first necessary to fragment the olivine grains into individual, fracture-absent domains in order to increase the Srp surface area available for reaction

with HF. To accomplish this, the coarser-grained size fractions (> 106 μm) were subjected to a gentle grinding process using an agate mortar and pestle and were then sieved to 106-75 μm. Inspection of this size fraction under polarized light revealed that few of the grains contained internal, serpentine-bearing fractures.

To determine the length of time for HF treatment necessary to remove Srp, the 106-75 μm fraction of sample 11-III-A-1-1 was divided into several aliquots, each of which were reacted with reagent grade (48%) HF for varying time intervals (2, 4, 6, 8, and 10 minutes). The optimal time interval was considered to be the time at which the serpentine is almost entirely dissolved without the occurrence of significant Fo loss, and was determined to be 6 minutes according to the visual inspection of grains after each treatment. As a result, all Fo samples were treated with HF for 6 minutes. Commonly, the HF treatment resulted in the occurrence of low-relief material (possibly MgF_2) rimming forsterite grains, and these low-relief rims were largely removed through a short (~1 minute) soft grind using an agate mortar and pestle. This ground material was then re-sieved and grains smaller than 75 μm were discarded. Finally, the residual 106-75 μm material was cleaned thoroughly using a sequential ultrasonic treatment in de-ionized water, ethanol, and finally acetone.

APPENDIX C

CARBONATE MATRIX ANALYSES FOR $\delta^{13}C$ AND $\delta^{18}O$

Traverse 11-IIIA/B

Sample[1]	$\delta^{13}C$ (‰) (VPDB)	$\delta^{18}O$ (‰) (VSMOW)
A-1-I	5.2	23.1
A-1-I	5.2	23.4
A-1-I	5.3	23.3
A-1-2-I	5.4	23.3
A-1-2-II	5.3	23.4
A-1-2-II	5.2	23.2
A-1-3	5.9	24.2
A-1-4-I	5.5	23.9
A-1-4-II	5.6	24.5
A-1-4-III	4.2	12.7
A-2-1-I	5.8	24.6
A-2-1-II	5.7	24.3
A-2-1-III	5.5	23.8
A-3-1-I	5.9	22.7
A-3-1-I	6.0	23.1
A-3-1-II	5.9	22.8
A-3-2	6.2	23.7
A-4-1-I	6.0	23.9
A-4-1-II	6.1	23.9
A-4-1-II	6.1	24.6
B-5-1-I	5.9	23.3
B-5-1-II	5.7	23.0
B-7-1-I	5.9	24.4
B-7-1-II	5.9	23.4
B-7-2	5.7	24.2
B-8-1-I	5.1	22.4
B-8-1-I	5.1	22.3
B-8-1-II	5.1	22.5
B-8-1-III	5.0	22.5
B-8-2-I	5.1	24.2
B-8-2-II	5.3	24.7
B-8-2-III	5.4	24.6
B-8-3-A-1	5.5	24.7
B-8-3-A-2	5.3	24.5
B-8-3-I	5.3	23.5
B-8-3-II	5.4	24.7
B-9-1-I	5.5	23.8
B-9-1-II	5.5	20.1

Traverse 11-IIIC/D

Sample[1]	$\delta^{13}C$ (‰) (VPDB)	$\delta^{18}O$ (‰) (VSMOW)
C-1-A	5.8	24.2
C-1-B-I	5.4	24.9
C-1-B-II	6.0	24.3
C-2-I	5.6	24.9
C-2-II	5.8	24.5
C-3	5.5	23.2
C-4	5.8	23.6
C-5-I	5.8	24.0
C-5-II	5.6	23.7
C-5-III	5.7	23.9
D-0-B-I	5.4	21.9
D-0-B-II	5.5	21.7
D-1-I	5.2	20.2
D-1-II	5.4	20.6
D-2	5.5	22.3
D-3-I	5.4	19.6
D-3-II	5.5	19.7
D-4-I	5.4	19.1
D-5-I	5.0	19.9
D-5-II	4.7	19.6
D-6-A-I	5.4	19.6
D-6-A-II	4.5	10.9
D-6-A-III	4.9	19.8
D-6-A-IV	4.8	19.3
D-6-B-I	5.2	20.0
D-6-B-I	5.2	20.5
D-6-B-II	5.1	19.4
D-7-A-I	5.4	22.9
D-7-A-II	5.6	23.5

Traverse 01-III

Sample[1]	$\delta^{13}C$ (‰) (VPDB)	$\delta^{18}O$ (‰) (VSMOW)
1	1.1	15.9
1-x	1.5	17.5
1-x	1.4	17.3
1/2-a-I	1.3	17.2
1/2-a-II	0.4	17.3
1/2-a-III	-0.4	16.7
2/3-a	-4.4	11.8
3/4-a-I	1.5	17.7
3/4-a-II	0.2	17.0
3/4-b-I	1.1	18.0
3/4-b-II	0.5	17.0
3/4-b-III	1.0	16.6
3/4-b-IV	0.1	15.7
4/5-a-I	2.7	19.0
4/5-a-III	2.7	18.4
4/5a-II	2.2	18.0

Traverse 99V

Sample[1]	$\delta^{13}C$ (‰) (VPDB)	$\delta^{18}O$ (‰) (VSMOW)
11	4.4	23.1
12C	4.8	24.1
3 bulk	5.4	25.4
3 bulk	5.3	25.4
3 bulk	5.3	25.3
3 dol	5.4	26.2
3-xz	5.4	27.0
5a	4.4	24.0

All other samples

Sample[1]	$\delta^{13}C$ (‰) (VPDB)	$\delta^{18}O$ (‰) (VSMOW)
02-DCF-1	3.2	28.8
02-DCG-1	6.1	30.1
02-DCM-1	0.2	30.4
12-1a-I	0.8	15.1
12-1b-I	-1.0	15.2
12-1b-II	1.2	15.4
12-1b-III	0.8	9.0
12-2	2.4	12.2
23-A	5.4	23.6
23-B	4.0	23.1
23-B-I	4.0	23.2
23-B-II	4.0	23.7
24-1a-I	-1.1	18.9
24-1a-II	-1.1	17.8
24-1b-1	-0.9	14.4
24-1b-II	1.5	15.3
27-1c-1	3.8	25.7
4-1a-1	1.0	34.3
89-10	-0.4	21.7
89-16b	4.2	28.6
FZ4-4a	4.6	25.3
FZ4-5a	4.2	26.6
FZ4-5b dark	4.3	26.4
FZ4-5b (I) bulk	4.4	26.2
FZ4-5b (I) bulk	4.5	26.4
FZ4-5b (I) bulk	4.5	25.8
FZ4-5b (I) bulk	4.4	25.5
FZ4-5b (I) dol I	4.4	26.6
FZ4-5b (I) dol II	4.5	26.5
FZ7-4 coarse	5.9	23.4
FZ7-4 fine	6.1	23.7
FZ7-6	5.7	22.3
FZ9-18	4.3	24.4
FZ9-18 (I)	4.5	24.8
MBL std JRB	3.1	26.8
Rz-1-2a-a	2.0	19.4
Rz-1-2a-b	1.8	19.7
Rz-1-2b-c	2.2	24.4
Rz-1-2b-d	2.3	23.3
Rz-1-2b-e	2.1	22.8
Rz-1-2b-f	2.0	20.4

[1]Roman numerals following sample numbers indicate a distinct domain within a slab (drillholes are labeled on each slab).

APPENDIX D

DETAILED ICP-MS METHODS, DATA, AND CALCULATIONS

D.1 Sample Selection

Forty-eight carbonate samples from the Alta aureole and unaltered protolith were selected for trace element analysis with roughly equal representation of each metamorphic zone and the unaltered protolith. Five contact-skarns and six granodiorite samples from the Alta Stock were selected for analysis as well, with an equal representation of the central and border phases of the stock. This provides a comprehensive suite of rocks that document the major and trace element characteristics from the innermost stock to the non-metamorphosed protolith (Figure 2-1), and therefore allows for identification of systematic trends in elemental concentration as a function of distance from the intrusive contact. The metamorphic zone, lithology, distance from the intrusive contact, $\delta^{18}O$ value of the carbonate matrix, and measured element concentrations for each sample are compiled in this appendix.

D.2 Carbonate Sample Preparation

Once carbonate samples were selected, a representative, approximately 200 mg cube was extracted from each sample slab with a Craftsman Dremmel diamond saw tool, with special care being taken to avoid areas that displayed veining and/or high sulfide

content. This approach was necessary in order to avoid the nugget effect, in which a small concentration of sulfide minerals or vein phases would result in an inaccurate representation of the trace element content of the sample. All samples were thoroughly cleaned with distilled water after they had been extracted from the slab, and were carefully weighed after a 24-hour drying period. Each sample cube was dissolved using the methods described below.

In preparation for carbonate dissolutions, low density polyethylene (LDPE) sample tubes were subjected to a 24 hour heated, 10% HCl leach treatment in order to remove impurities within the tubes. A solution was then prepared by adding approximately 10 mL of 5% trace metal grade (TMG) HNO_3 to the carbonate sample. Once reaction had ceased, the solution was centrifuged, isolating any residual solid material at the bottom of the sample tube, and this residual solid would later be weighed after a 24 hour drying period in order to calculate the proportion of dissolved material. A primary dilution was prepared by adding ~9 mL of 5% TMG HNO_3 to approximately 1 mL of the original centrifuged solution and a final (secondary) dilution was then prepared by diluting the primary dilution with 5% TMG HNO_3 by a factor of 40. One hunderd μg In (25 ppm solution) was added to each final dilution as an internal standard.

D.3 Stock and Skarn Sample Preparation

Once stock and skarn samples were selected, several small cubes (~500 mg) were removed from each sample slab, and were powdered using a Tungsten-carbide shatter box. The powder was then thoroughly mixed, and an approximately 200 mg aliquot was removed for dissolution. Teflon sample tubes were subjected to a 24 hour heated, 10% HCl leach treatment in order to remove impurities that could potentially affect results. A

solution was then prepared in the Teflon sample tube by combining the powdered sample and a mixture of TMG HNO_3, HCl, and HF. The tube containing the solution was then placed on a heat source until the dissolution ran to completion. A primary dilution was then prepared by combining approximately 0.5 mL of the solution with ~10 mL 5% TMG HNO_3 in an LDPE sample tube. Since a wide range in concentration was expected for the suite of elements to be analyzed, two separate final dilutions were prepared for each sample. Primary dilutions prepared for the analysis of the most concentrated elements (Na, Al, K, Fe, Mn) were diluted by a factor of ~100 to produce the final dilution, and primary dilutions prepared for the analysis of all other elements were diluted by a factor of ~10. One hundred μg In (25 ppm solution) was added to each final dilution as an internal standard.

D.4 Analytical Methods and Element Concentration Calculations

All final dilutions were analyzed for Li, Be, Na, Al, K, Ti, Mn, Fe, Cu, Zn, Rb, Sr, Ba, La, Ce, Sm, Lu, and Pb using an Agilent 7500ce Inductively Coupled Plasma Mass Spectrometer (ICP-MS) at the University of Utah. The Agilent-recommended mass number was used for each element, and the collision cell (4 $mL \cdot min^{-1}$ He) was employed for elements with potential interferences (Na, Al, K, Fe, and Mn). Integration times of 0.1 seconds per point and 0.3 seconds per mass were used for all elements. To account for measurement drift, five samples were measured in sequence and were bracketed by two blank measurements (i.e., 2 blanks - 5 samples - 2 blanks). Concentrations were measured in counts per second (cps), and were blank-corrected by subtracting the mean value of the four bracketing blank measurements. The blank-corrected values were then converted to parts per billion (ppb) using the following process.

A 6-point calibration curve was constructed for each element using varying concentrations of the USGS-T REE standard solution (dilutions used are detailed in Table D-1). The known concentrations of each USGS-T REE dilution were plotted against the ratio of the measured counts per second value for a given element to the counts per second value for the Indium internal standard for each dilution, and the concentration of the element in the sample was determined using equation D-1 (copper is used as an example element):

$$Cu_{ppb} = \left(\frac{\frac{Cu^{sm}_{cps}}{In^{sm}_{cps}} - b_{cc}}{m_{cc}} - Cu^{blk}_{ppb} \right) \times DF \qquad \text{(D-1)}$$

where *cps* is the ICP-MS-measured counts per second for the given element, Cu^{sm}_{cps} is the measured cps value for Cu in the sample, In^{sm}_{cps} is the measured cps value for In in the sample, b_{cc} is the intercept of the calibration curve, m_{cc} is the slope of the calibration curve, Cu^{blk}_{ppb} is the average measured Cu concentration in the four sample-bracketing blank measurements, and DF is the sample dilution factor. All concentration data and oxygen isotope values used to create Figures 2-2a through 2-2e and 2-3a through 2-3e are present in Tables D-2 to D-4 and D-5.

D.5 Evaluation of Uncertainty

Three major sources of error were identified and considered in the total error calculations for the concentration values for each element in each sample as determined

Table D-1. Calibration curve concentration values by element (ppb).

Element	USGS-T REE initial	Calibration Point 1	2	3	4	5	6
Li	50.18	10.04	2.509	1.255	0.502	0.251	0.125
Be	59.26	11.85	2.963	1.481	0.593	0.296	0.148
Ti	125.13	25.03	6.257	3.128	1.251	0.626	0.313
Cu	37.61	7.521	1.880	0.940	0.376	0.188	0.094
Zn	612.77	122.6	30.64	15.32	6.128	3.064	1.532
Rb	52.62	10.52	2.631	1.316	0.526	0.263	0.132
Sr	2354.70	470.9	117.7	58.87	23.55	11.77	5.887
Ba	910.53	182.1	45.53	22.76	9.105	4.553	2.276
La	6.54	1.309	0.327	0.164	0.065	0.033	0.016
Ce	8.70	1.739	0.435	0.217	0.087	0.043	0.022
Sm	0.89	0.178	0.044	0.022	0.009	0.004	0.002
Lu	0.44	0.089	0.022	0.011	0.004	0.002	0.001
Pb	16.98	3.396	0.849	0.425	0.170	0.085	0.042
Na	63579.45	12715	3179	1589	635.8	317.9	158.9
Al	800.24	160.0	40.01	20.01	8.002	4.001	2.001
K	111441.53	22288	5572	2786	1114	557.2	278.6
Mn	327.05	65.41	16.35	8.176	3.271	1.635	0.818
Fe	2325.38	465.1	116.3	58.13	23.25	11.63	5.813
Dilution Factor	0	5	20	40	100	200	400

by equation D-1. The first and most significant error source is associated with the relative standard deviation of the cps (RSD_{cps}) values for a given element, and was given as a percentage value in a report produced by the Agilent 7500ce software. Second, the background error was determined by equation D-2:

$$RSD_{BG}^{sm}(\%) = 100\left(\frac{\sigma_{Cu(cps)}^{blk}}{\overline{Cu}_{cps}^{sm}}\right) \qquad \text{(D-2)}$$

where RSD_{BG}^{sm} is the relative standard deviation of the background (BG) for an individual sample (sm), derived from the standard deviation of the blank (blk) measurements and the calculated cps value of Cu in the sample. Equation D-2 considers the total average cps values for a given element across all measurements of the blank as compared to the cps measurement of that element in a given sample. The error associated with

Table D-2. Transition metal and Pb concentrations used in creating Figure 2-2. Values below the limit of detection are not listed.

Zone/ Lithology	Sample	D (m)	Transition Metals and Post Transition Metals (ppb)						
			Ti	Cu	Zn	Pb	Al	Mn	Fe
Stock	C-4	-898	6061243	22873	84691	24522	63684457	487146	29707054
	H6C1	-693	6819196	6456	70778	17547	54431900	499085	30162206
	C-5	-410	7450745	40283	80202	16110	59790326	523002	34125220
	B-4	-282	4824304	20820	57699	21079	60458342	381689	23006238
	D2B3b	-154	9842073	445139	119038	18219	58709721	755196	50445975
	88-I9	-100	8997491	75389	68932	16308	44847683	484888	37549388
Skarn	As-18-6	0	1228748	609004	330965	29938	14721605	5266317	384188504
	As9-5,6,1	0	7771094	5566	189318	4887	24901590	4067818	32070556
	As-4e-3	0	3750702	117997	295792	61945	36062116	1786315	85585468
	As-11e-1a	0	1782909	1352602	6776958	168513	13364939	4290259	62449583
	As-18a-9	0	3463129	41219	160933	4987	17065773	2009304	79028744
Periclase Zone	40148	10	3853		2186	1456	12501	33081	16592
	12-1b	10	21297	2070	8778		84	3739	27889
	88-40	12	8257	258	16443	217	229592	26316	141910
	23-B(1)	25	4272	6218	548	1092	283083	107452	170891
	01-III-2/3-2	45	1699	1680	10641	934	26425	116054	88667
	01-III-1-x	45	3049	1255	15240	1292	121002	20954	121002
	01-III-4/5-a	45	1813	69	169	87	7254	46446	111547
	01-III-2/3-3	45	4084	11239	74871	923	60851	135489	1472652
	32-1	83	19164	743	10751	2004	553567	585845	1999807
	88-20	90	181495	1559	4229	17694	7329726	193932	8778113
	88-B6	100	108889	933	270465	2693	3170783	280792	6081565
	941-9-2-8	170	2221	2273	13221	596	606096	76969	290208
	941-9-2-9	170	10210	101	53864	208	1003494	184335	2281546
	94I-2-2	170	1692	11331	993	173	24087	63000	63471
	94I-3-2	170	10407	527	36477	97	109033	154425	1279200
Forsterite Zone	88-53	215	16297	656	26026	1178	50959	78827	292944
	88-8	230	6399	728	6546	2714	119005	342287	524428
	A-3-1	300	3025			454	32678	66774	99032
	B-7-1 coarse	300	3385			903	16044	58903	36168
	B-7-1 fine	300	5968		3155	645	128126	71488	159447
	A-1-1	300	19875	726	1681	2721	304095	99857	541097
	02-FZ9-18	455	36473	463	15792	1520	1692778	83736	1169762
	FZ4-4a	475	28180	397	13924	928	1012256	80171	507600
	88-18	485							
	99V-11	615	2989	96	754	1337	174431	61536	128370
	99V-12C	615	49588	417	6008	8568	1083833	154222	847836
	99V-3	615	3911		38	353	71098	90932	156861
	99V-10	615	2302		193	736	1186430	52433	71311
	99V-5a	615	2936		659	814	68458	90675	62532
Tremolite Zone	89-20	985	10470	205	4698	364	47583	189358	744799
	89-10	990	3620	65	6775	420	119169	303239	837132
	89-16b	990	1182	151	2093	1201	32626	73915	545059
	89-16a	990	312			5		4	3807
	1-1-2-1	1430	1540		51	248	39152	141396	15269
	1-1-2-2	1430	3004		38769	377	12622	193748	42727
Talc Zone	4-1a-1	1485	2498	167	3982	6165	123156	143341	207789
	4-1a-2	1485	1895	310	9400	14325	11963	105792	68168
	35523	1485	3203		1567	489	70499	120676	457335
	27-1c-1	1567	2685	212	1390	862	1510389	162077	445178
	27-1c-2	1567	2483	207	864	611	98911	165262	138130
Protolith	02-DCG-1-i	2000	17833	558	34969	2076	736650	221448	639714
	02-DCG-1-ii	2000	1838	258	7954	950	91893	112444	981018
	02-DCM-1	2000	2581	398	14933	4705	69485	260270	2084033
	02-DCMF-1	2000	2671	197	16187	993	119376	201165	462390
	02-DCF-1	2000	2605		20334	395	79402	119418	358236
	02-DCG-3-ii	2000	452		324	27	46011	26077	82238
	02-DCMF-1	2000	3291		16619	7311	79435	499600	1966906
	02-DCG-3-iii	2000	16074	591	47582	1826	703267	219899	636801

Table D-3. Alkali metal and Alkaline earth metal concentrations used in creating Figure 2-2. Values below the limit of detection are not listed.

Zone/ Lithology	Sample	D (m)	Alkali Metals and Alkaline Earth Metals (ppb)						
			Li	Be	Rb	Sr	Ba	Na	K
Stock	C-4	-898	19638	2552	104886	856303	1997610	25534587	20873072
	H6C1	-693	16569	2815	123033	704665	1756706	22207921	21133398
	C-5	-410	16537	2706	89999	917210	2164186	25821511	20208780
	B-4	-282	14804	2647	79590	851534	1547404	27647962	20242341
	D2B3b	-154	9726	2630	52245	1075729	1293403	24326160	11324769
	88-I9	-100	11214	2120	40594	992343	2028920	22848438	15055698
Skarn	As-18-6	0	22176	6303	1143	107308	17685	602812	75637
	As9-5,6,1	0	2696	2924	692	117365	13513	299870	
	As-4e-3	0	14197	641	219102	1223808	88493	679276	22951957
	As-11e-1a	0	12090	4754	13897	294935	6854	384354	385023
	As-18a-9	0	1196	1822	1962	19140	9188	124192	
Periclase Zone	40148	10			407	547546	3703		
	12-1b	10			299	1480473			
	88-40	12		1	25	144851	2601	20250	2241
	23-B(l)	25			45	174760	7670		
	01-III-2/3-2	45	65		9	273693	8804		
	01-III-1-x	45	44		14	260244	4338		
	01-III-4/5-a	45	1013			223531	5899		
	01-III-2/3-3	45		7		211168	7541		
	32-1	83	7679	163	7544	217159	18205	487058	2535275
	88-20	90	9260	220	29784	361923	40651	287939	7809409
	88-B6	100	661	41	116	646984	11747	193854	158284
	941-9-2-8	170	72	4	1	224328	2416		2215
	941-9-2-9	170	1143	25	22	119772	1766		
	941-2-2	170	98			156697	1607		
	941-3-2	170		36	10	144663	1864		
Forsterite Zone	88-53	215	130	26	151	1352499	26268	121070	140683
	88-8	230	231	5	507	170043	3522		103182
	A-3-1	300			24	246396	665		
	B-7-1 coarse	300			238	234704	1295		
	B-7-1 fine	300			292	234446	1316		
	A-1-1	300		12	149	1089708	2107	25762	26810
	02-FZ9-18	455	2710	105	2449	704067	9261	166386	794578
	FZ4-4a	475	614	4	3538	602540	11511	70276	1019546
	88-18	485							
	99V-11	615	124		6	266992	851		
	99V-12C	615	1932	48	10978	596141	27821	173188	3048631
	99V-3	615		14	1270	61443	2010		293624
	99V-10	615		17		248951	2993		
	99V-5a	615			1305	87359	2228		562710
Tremolite Zone	89-20	985	1014	48	706	197824	2348	142453	436145
	89-10	990	266	17	1645	124222	3555		488677
	89-16b	990	185	68	112	55638	1499		
	89-16a	990	2076		40				
	1-1-2-1	1430	1917	47		36765	2005	131065	
	1-1-2-2	1430	64	54	77	139837	4790		
Talc Zone	4-1a-1	1485	2542	65	22	43217	3841	183101	
	4-1a-2	1485	147	25	21	294471	4197		
	35523	1485		84	85	47712	2078	144776	
	27-1c-1	1567	1230	243	1139	90367	55809	37313	185479
	27-1c-2	1567	1481	26	277	42716	2169	101521	34910
Protolith	02-DCG-1-i	2000	2816	228	334	107952	4149	1470615	257691
	02-DCG-1-ii	2000	447	123	74	46474	1584	176574	
	02-DCM-1	2000	1388	192	84	84030	3355	14884	9519
	02-DCMF-1	2000	991	75	61	31626	1515	302017	168565
	02-DCF-1	2000		75	31	37403	1662	154364	
	02-DCG-3-ii	2000			23	14735	179		
	02-DCMF-1	2000	898	110	98	69193	3239		
	02-DCG-3-iii	2000	1478	199	257	109853	4144	1266512	115134

Table D-4. Rare earth element concentrations used in creating Figure 2-2. Values below the limit of detection are not listed.

Zone/ Lithology	Sample	D (m)	Rare Earth Elements (ppb)			
			La	Ce	Sm	Lu
Stock	C-4	-898	66089	124567	7271	243
	H6C1	-693	68987	140293	8384	289
	C-5	-410	55773	115453	7916	235
	B-4	-282	34306	66994	4733	167
	D2B3b	-154	62818	135457	8824	285
	88-I9	-100	35481	78409	6612	184
Skarn	As-18-6	0	62777	57001	1448	161
	As9-5,6,1	0	58299	137545	9100	189
	As-4c-3	0	51449	90271	3297	118
	As-11e-1a	0	23356	30763	2112	241
	As-18a-9	0	43798	86752	5900	230
Periclase Zone	12-2	10	2631	1111	203	16
	12-1b	10	15578	12728	5776	1104
	88-40	12	1526	591	153	16
	23-B(l)	25	2743	5280	555	40
	01-III-2/3-2	45	2530	1538	209	32
	01-III-1-x	45	3452	1203	341	42
	01-III-4/5-a	45	1213	884	73	16
	01-III-2/3-3	45	2156	1892	176	20
	32-1	83	11927	15229	2236	102
	88-20	90	17875	39424	3115	425
	88-B6	100	7515	5076	995	124
	94I-9-2-8	170	1948	2566	256	44
	94I-9-2-9	170	1756	2764	259	20
	94I-2-2	170	400	452	37	6
	94I-3-2	170	874	911	47	3
Forsterite Zone	88-53	215	24915	2072	1175	277
	88-8	230	6599	3473	774	46
	A-3-1	300	2658	4467	350	19
	B-7-1 coarse	300	1782	2793	216	9
	B-7-1 fine	300	1866	3144	310	23
	A-1-1	300	9519	12662	1861	113
	02-FZ9-18	455	11695	18737	1393	188
	FZ4-4a	475	12011	20961	1634	184
	88-18	485				
	99V-11	615	6739	12765	1102	29
	99V-12C	615	13457	24256	1708	147
	99V-3	615	2704	4749	362	22
	99V-10	615	6118	10698	810	35
	99V-5a	615	2025	3544	275	36
Tremolite Zone	89-20	985	5009	6694	511	35
	89-10	990	4346	5443	693	33
	89-16b	990	3151	4266	217	24
	89-16a	990	8	3		0
	1-1-2-1	1430	1109	524	109	10
	1-1-2-2	1430	2911	1927	351	48
Talc Zone	4-1a-1	1485	3083	797	268	27
	4-1a-2	1485	4523	1554	408	71
	35523	1485	4181	1975	712	56
	27-1c-1	1567	3256	4689	661	63
	27-1c-2	1567	1856	2389	382	28
Protolith	02-DCG-1-i	2000	3451	4843	790	47
	02-DCG-1-ii	2000	985	1732	302	16
	02-DCM-1	2000	3933	7161	572	26
	02-DCMF-1	2000	1420	2517	214	16
	02-DCF-1	2000	1034	1926	199	8
	02-DCG-3-ii	2000	826	1401	62	0
	02-DCMF-1	2000	3772	7302	686	27
	02-DCG-3-iii	2000	3183	4559	677	37

Table D-5. Oxygen isotope data used to create Figure 2-3.

Zone	Sample	D (m)	$\delta^{18}O_{Carbonate}$ (‰)
Per	12-2	10	12.2
Per	12-1b	10	17.3
Per	88-40	12	17.0
Per	23-B(1)	25	23.2
Per	01-III-1-x	45	17.2
Per	01-III-4/5-a	45	18.4
Per	01-III-2/3-3	45	11.8
Per	88-20	90	22.3
Per	88-B6	100	13.7
Per	94I-9-2-8	170	17.5
Per	94I-9-2-9	170	12.0
Per	94I-2-2	170	14.7
Per	94I-3-2	170	10.8
Fo	88-53	215	14.7
Fo	88-8	230	18.9
Fo	A-3-1	300	22.7
Fo	B-7-1 coarse	300	23.4
Fo	B-7-1 fine	300	24.4
Fo	A-1-1	300	23.1

interpolation of sample concentration values from the calibration curve is determined with equations D-3a and D-3b:

$$s_{x_0}(\text{ppb}) = \frac{s_{y/x}}{b}\sqrt{1+\frac{1}{n}+\frac{(y_0-\bar{y})^2}{b^2\sum(x_i-\bar{x})^2}} \qquad \text{(D-3a)}$$

$$s_{y/x} = \sqrt{\frac{\sum\left(y_i-\hat{y}\right)^2}{n-2}} \qquad \text{(D-3b)}$$

where y and x represent the values used to create the calibration curve, b is the slope of the calibration curve, and n is the number of measurements used in creating the calibration curve. Finally, the total combined error is given by Equation D-4:

$$\text{RSD}_{\text{tot}}^{\text{sm}}(\%) = \sqrt{\left(\text{RSD}_{\text{cps}}^{\text{sm}}\right)^2+\left(\text{RSD}_{\text{BG}}^{\text{sm}}\right)^2+\left(100\left(\frac{s_{x_0}}{\text{Cu}_{\text{ppb}}^{\text{sm}}}\right)\right)^2} \qquad \text{(D-4)}$$

where Cu_{ppb}^{sm} represents the concentration value of Cu in the sample as determined through the slope and intercept of the calibration curve. It is important to note that because neither the raw concentration values of elements within samples nor the total dilution factor (DF) remain constant, the total combined error must be calculated for each individual sample, and will differ based on the sample's location on the calibration curve (i.e., the average measured cps value of the measured element), the background value of the element within the measured blanks, and the consistency of the measurements

(RSD_{cps}). Mean uncertainty values (RSD %) for each element are listed in Table D-6.

D.6 Calculation of Threshold Values

Threshold values for a given element in the Alta aureole are determined by normalizing the concentration of that element to Al concentration in the unaltered protolith. The relatively consistent ratios of Al to Ti and most Lanthanides (Figure D-1) require that either the concentrations of these low-solubility elements were altered in the same ratio at which they were originally present in the host carbonate, or that these elements were essentially conserved during geochemical alteration of the protolith. The normalization of element concentrations based on Al content therefore identifies false positive anomalies that may result from passive enrichment of trace elements, which often occurs as a result of volume loss through carbonate dissolution (Escalante et al., 2010).

For each carbonate protolith sample, the element:Al value was calculated, and the median protolith value was determined for each element analyzed. Upper and lower threshold values were then calculated by equations D-5a and D-5b, respectively:

$$Cu_{ppb} = Al^{sm}_{ppb} \times \left[\tilde{x}_{ppbCuppbAl} + 2MAD_{ppbCuppbAl}\right]^{pt} \quad \text{(D-5a)}$$

$$Cu_{ppb} = Al^{sm}_{ppb} \times \left[\tilde{x}_{ppbCuppbAl} - 2MAD_{ppbCuppbAl}\right]^{pt} \quad \text{(D-5b)}$$

where sm denotes Al concentration in the sample, and pt denotes the median Cu:Al ratio in the protolith ± 2MAD. These equations define the range in element:Al values for each

Table D-6. Mean total uncertainty (RSD_{tot}) for each element as determined through equation D-4. Samples below the detection limit are not plotted in concentration-distance profiles and are therefore not considered in the average uncertainty calculations.

Alkali Metals/Alkaline Earth Metals	Li	Be	Rb	Sr	Ba	Na	K
	28.53%	26.89%	12.60%	2.28%	3.32%	31.13%	22.66%
Transition Metals/Post Transition Metals	Ti	Cu	Zn	Pb	Al	Mn	Fe
	8.92%	21.76%	7.36%	5.27%	5.32%	1.82%	13.96%
Rare Earth Elements	La	Ce	Sm	Lu			
	3.47%	3.60%	12.07%	13.58%			

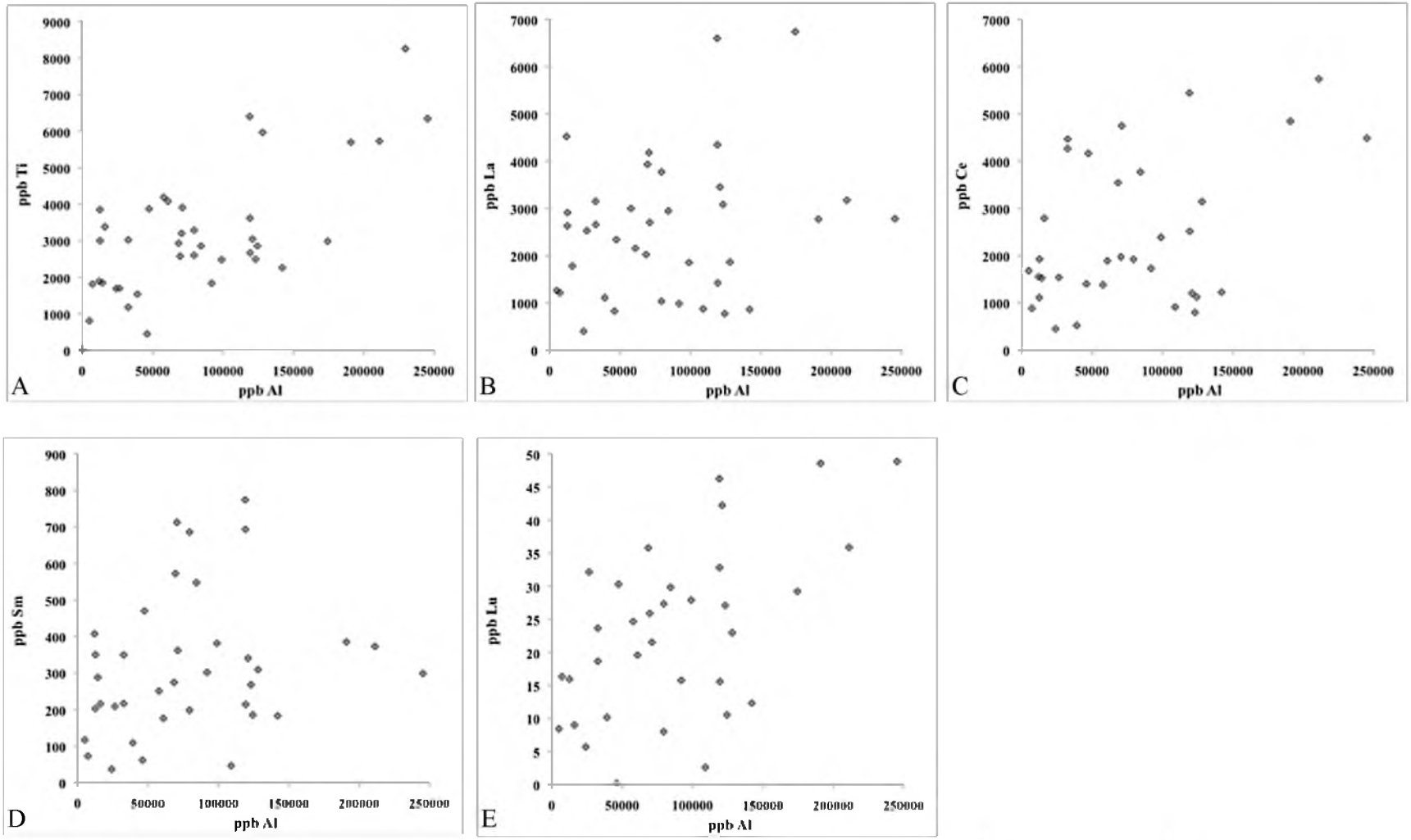

Figure D-1. ICP-MS analysis of Alta aureole samples (marble and limestone protolith) showing Al concentration and other low solubility element concentrations. Elements shown are **(A)** Ti, **(B)** La, **(C)** Ce, **(D)** Sm, and **(E)** Lu. Generally, elevated Al concentrations correspond to elevated Ti and Lanthanide concentrations (particularly for Ce and Lu).

sample using the median value ± 2 median absolute deviations (MAD) for the host rock samples (Cu is used as an example element). Median and MAD values were implemented because these values are more resistant to outliers than mean and standard deviation, and therefore identify the largest number of true anomalies (Reimann et al., 2005). Aureole concentrations were only considered anomalous if the standard error range on the measurement did not overlap with the threshold range (methods for error calculation are detailed elsewhere in Appendix D). Threshold ranges cannot be defined for skarn samples because Al immobility cannot be assumed for the conditions responsible for skarn formation at the intrusive contact with the Alta Stock.

REFERENCES

Baker, A.A., Calkins, F.C., Crittenden, M.D., and Bromfield, C.S., 1966, Geologic map of the Brighton quadrangle, Utah: US Geological Survey Map GQ-535, 7'5".

Barker, S.L.L., Dipple, G.M., Hickey, K.A., Lepore, W.A., and Vaughan, J.R., 2013, Applying stable isotopes to mineral exploration: teaching an old dog new tricks: Economic Geology, v. 108, p. 1-9.

Bartley, J.M., Bowman, J.R., Coleman, D.S., and Didericksen, B.D., 2007, The rate problem of emplacement of the Alta Stock, Wasatch Mountains: Geological Society of America Abstracts with Programs, v. 39, no. 5, p. 5.

Bartley, J.M., Coleman, D.S., and Glazner, A.F., 2008, Incremental emplacement of plutons by magmatic crack-seal: in Petford, N., & Sparks, S. (eds.), Plutons and Batholiths. Transactions of the Royal Society of Edinburgh (Wallace Pitcher Memorial Issue), v. 97, in press.

Baumgartner, L.P. and Valley, J.W., 2001, Stable isotope transport and contact metamorphic fluid flow: in Stable Isotope Geochemistry: Reviews in Mineralogy and Geochemistry, v. 43, 661 p.

Bowman, J.R., 1998, Stable-isotope systematics of skarns: Mineralogical Association of Canada Short Course Series, v. 26, p. 99-145.

Bowman, J.R., Valley, J.W., and Kita, N.T., 2009, Mechanisms of oxygen isotopic exchange and isotopic evolution of $^{18}O/^{16}O$-depleted periclase zone marbles in the Alta aureole, Utah – Insights from ion microprobe analysis of calcite: Contributions to Mineralogy and Petrology, v. 157, p. 77-93.

Bowman, J.R., Willett, S.D., and Cook, S.J., 1994, Oxygen isotopic transport and exchange during fluid flow: one-dimensional models and applications: Amer. J. Sci., v. 294, p. 1-55.

Boyle, R.W., 1967, Geochemical prospecting – retrospect and prospect: Transactions of the Canadian Institute of Mining and Metallurgy, v. 70, p. 1-6.

Breitenbach, S.F.M. and Bernasconi, S.M., 2011, Carbon and oxygen isotope analysis of small carbonate samples (20 to 100μg) with a GasBench II preparation device: Rapid Communications in Mass Spectrometry, v. 25, p. 1910-1914.

Chadwell, L.M. and Bowman, J.R., 2005, Crystal size distribution analysis of forsterite in the Alta aureole, Utah: Geological Society of America Abstracts with Programs, v. 37, p. 227.

Chako, T., Cole, D.R., and Horita, J., 2001, Equilibrium oxygen, hydrogen, and carbon isotope fractionation factors applicable to geologic systems: Reviews in Mineralogy and Geochemistry, v. 43, p. 1-81.

Chiba, H., Chacko, T., Clayton, R.N., and Goldsmith, J.R., 1989, Oxygen isotope fractionations involving diopside, forsterite, magnetite, and calcite: application to geothermometry: Geochimica et Cosmochimica Acta, v. 53, p. 2985-2995.

Cole, D.R. and Chakraborty, S., 2001, Rates and mechanisms of isotopic exchange: in Stable Isotope Geochemistry: Reviews in Mineralogy and Geochemistry, v. 43, 661 p.

Cook, S.J., 1982, The physical-chemical conditions of contact skarn formation at Alta, UT, MS thesis, University of Utah, Salt Lake City, 338 p.

Cook, S.J. and Bowman, J.R., 1994, Contact metamorphism surrounding the Alta Stock: Thermal constraints and evidence of advective heat transport from calcite + dolomite geothermometry: American Mineralogist, v. 79, p. 513-525.

Cook, S.J., Bowman, J.R., and Forster, C.B., 1997, Contact metamorphism surrounding the Alta Stock: finite element model simulation of heat- and $^{18}O/^{16}O$ mass-transport during prograde metamorphism: American Journal of Science, v. 297, p. 1-55.

Cook, S.J. and Bowman, J.R., 2000, Contact metamorphism surrounding the Alta stock--Fluid-rock interaction accompanying metamorphism of siliceous dolomites: Journal of Petrology, v. 41, p. 739-757.

Crittenden, M.D, 1965, Geology of the Dromedary Peak Quadrangle, Utah: Geologic Quadrangle Map – U. S. Geological Survey, Report: GQ-0378.

Crittenden, M.D., Stuckless, J.S., Jr., Kistler, R.W., and Stern, T.W., 1973, Radiometric dating of intrusive rocks in the Cottonwood area, Utah: U.S. Geological Survey Journal of Research, v. 1, p. 173-178.

Crowe, D.E., Valley, J.W., and Baker, K.L., 1990, Micro-analysis of sulfur-isotope ratios and zonation by laser microprobe: Geochim Cosmochim Acta, v. 54, p. 2075-2092.

Davis, S.R. and Ferry, J.M., 1993, Fluid infiltration during contact metamorphism of interbedded marble and calc-silicate hornfels, Twin Lakes area, central Sierra Nevada, California: Journal of Metamorphic Geology, v. 11, p. 71-88.

Escalante, A., Dipple, G.M., Barker, S.L.L, and Tosdal, R., 2010, Defining trace-element alteration halos to skarn deposits hosted in heterogeneous carbonate rocks: case study

from the Cu-Zn Antamina skarn deposit, Peru: Journal of Geochemical Exploration, v. 105, p. 117-136.

Ferry, J.M.,1996, Prograde and retrograde fluid flow during contact metamorphism of siliceous carbonate rocks from the Ballachulish aureole, Scotland: Contributions to Mineralogy and Petrology v. 124, 235–254.

Ferry, J.M. and Rumble, D., 1997, Formation and destruction of periclase by fluid flow in two contact aureoles: Contributions to Mineralogy and Petrology, v. 130, p. 358-378.

Ferry, J.M., Sorensen, S.S., and Rumble, D., 1998, Structurally controlled fluid flow during contact metamorphism in the Ritter Range pendant, California, USA: Contributions to Minealogy and Petrology v. 130, p. 358-378.

Ferry, J.M., Ushikubo, T., Kita, N.T., and Valley, J.W., 2010, Assessment of grain-scale homogeneity of carbon and oxygen isotope compositions of minerals in carbonate-bearing metamorphic rocks by ion microprobe: Geochim Cosmochim Acta, v. 74, p. 6517-6540.

Ferry, J.M., Ushikubo, T., and Valley, J.W., 2011, Formation of forsterite by silicification of dolomite during contact metamorphism: Journal of Petrology, v. 52, p. 1619-1640.

Ferry, J.M., Wing, B.A., Penniston-Dorland, S.C., and Rumble, D., 2002, The direction of fluid flow during contact metamorphism of siliceous carbonate rocks: new data for the Monzoni and Predazzo aureoles, northern Italy, and a global review: Contributions to Mineralogy and Petrology, v. 142, p. 679-699.

Hanson, S.L., 1995, Mineralogy, petrology, geochemistry and crystal size distribution of Tertiary plutons of the central Wasatch Mountains, Utah: Ph.D. thesis, University of Utah, Salt Lake City, Utah, 371 p.

John, D.A. 1989, Geologic setting, depths of emplacement, and regional distribution of fluid inclusions in intrusions of the central Wasatch Mountains, Utah: Economic Geology, v.84, p. 386-409.

Johnson, B.W., 2009, Oxygen isotope, cathodoluminescence, and titanium in quartz geothermometry in the Alta Stock, UT: geochemical insights into pluton assembly and early cooling history, MS thesis, University of Utah, Salt Lake City, Utah, 95 p.

Kelley, D.L., Kelley, K.D., Coker, W.B., Caughlin, B., and Doherty, M.E., 2006, Beyond the obvious limits of ore deposits: the use of mineralogical, geochemical, and biological features for the remote detection of mineralization: Economic Geology, v. 101, p. 729-752.

Kemp, W.M., III, 1985, A stable isotope and fluid inclusion study of the contact Al(Fe)-Ca-Mg-Si skarns in the Alta aureole, Alta, Utah. MS thesis, University of Utah, Salt Lake City, Utah, 65 p.

Kesler, S., Vennemann, T., Vazquez, R., Stenger, D.P., and Frederickson, G.C., 1995, Application of large-scale oxygen isotope haloes to exploration for chimney-manto Pb-Zn-Cu-Ag deposits: geology and ore deposits of the American Cordillera: Geological Society of Nevada Conference, Reno/Sparks, 1995, Proceedings, p. 1383-1396.

Korzhinskii, D.S., 1970, Theory of metasomatic zoning: Clarendon, Oxford, 162 p.

MacLean, W.H. and Barrett, T.J., 1993, Lithogeochemical techniques using immobile elements: Journal of Geochemical Exploration, v. 48, p. 109–133.

Megaw, P.K.M., 1990, Geology and geochemistry of the Santa Eulalia mining district, Chihuahua, Mexico: University of Arizona, Tuscon, Arizona, 461 p.

Meinert, L.D., Brooks, J.W. and Myers, G.L., 1991, Whole rock geochemistry and contrast among skarn types: in Buffa, R.H., and Coyner, A.R., eds., Geology and Ore Deposits of the Great Basin: Reno, Nevada: Geological Society of Nevada, Fieldtrip Guidebook Compendium, v. 1, p. 72-80.

Meinert, L.D., Dipple, G.M., and Nicolescu, S., 2005, World Skarn Deposits: in Economic Geology 100th Anniversary Volume, pp. 299-336.

Moore, J.N., and Kerrick, D.M., 1976, Equilibria in siliceous dolomites of the Alta Aureole, Utah. American Journal of Science, 276, 502-524.

Müller, T., Baumgartner, L.P., Foster, C.T., Jr., and Bowman, J.R., 2009, Crystal size distribution of periclase in contact metamorphic dolomite marbles from the southern Adamello Massif, Italy: Journal of Petrology, v. 50, p. 451-465.

Müller, T., Baumgartner, L.P., Foster, C.T., Jr., and Vennemann, T.W., 2004, Metastable prograde mineral reactions in contact aureoles: Geology, v. 32, p. 821-824.

Naito, K., Fukahori, Y., He, P.M., Sakurai, W., Shimazaki, H., and Matsuhisa, Y., 1995, Oxygen and carbon isotope zonations of wall rocks around the Kamioka Pb-Zn skarn deposits, central Japan: application to prospecting: Journal of Geochemical Exploration, v. 54, p. 199-211.

Reimann, C., Filzmoser, P., and Garrett, R., 2005, Background and threshold: critical comparison of methods of determination: Science of the Total Environment, v. 346, p. 1–16.

Ridley, J., and Thompson, A.B., 1986, The role of mineral kinetics in the development of metamorphic microtextures: in Walther, J. V., and Wood, B. J.,eds., Fluid-rock interactions during metamorphism: New York, Springer-Verlag, p. 154–193.

Rose, A.W., Hawkes, H.E., and Webb, J.S., 1979, Geochemistry in mineral exploration: San Diego, Academic Press Inc, 657 p.

Roselle, G.T., Baumgartner, L.P., and Chapman, J.A., 1997, Nucleation-dominated crystallization of forsterite in the Ubehebe Peak contact aureole, Death Valley National Park, California, Ph.D. thesis, University of Wisconsin, Madison, Wisconsin, 355 p.

Sharp, Z.D., 1990, A laser-based microanalytical method for the in situ determination of oxygen isotope ratios of silicates and oxides: Geochim Cosmochim Acta, v. 54, p. 1353-1357.

Sheppard, S.M.F. and Schwarcz, H.P., 1970, Fractionation of carbon and oxygen isotopes and magnesium between coexisting metamorphic calcite and dolomite: Contributions to Mineralogy and Petrology, v. 26, p. 161-198.

Smith, R.K., 1972, The mineralogy and petrology of the contact metamorphic aureole around the Alta Stock, Utah. Ph.D. thesis, University of Iowa, Iowa City, Iowa, p. 362.

Valley, J.W., Kitchen, N., Kohn, M.J., Niendorf, C.R., and Spicuzza, M.J., 1995, UWG-2, a garnet standard for oxygen isotope ratios: strategies for high precision and accuracy with laser heating: Geochim Cosmochim Acta, v. 59, p. 5223-5231.

Vázquez, R., Vennemann, T.W., Kesler, S.E., and Russell, N., 1998, Carbon and oxygen isotope halos in the host limestone, El Mochito Zn-Pb-(Ag) skarn massive sulfide-oxide deposit, Honduras: Economic Geology, v. 93, p. 15-31.

Vogel, T.A., Cambray, F.W., and Constenius, K.N., 2001, Origin and emplacement of igneous rocks in the central Wasatch Mountains, Utah: Rocky Mountain Geology, v. 36, p. 119-162.

Wicks, F.J., Whittaker, E.J.W., and Zussman, J., 1997, An idealized model for serpentine textures after olivine: Canadian Mineralogist, v. 15, p. 446-458.

Wilson, J.W., 1961, Geology of the Alta stock, Utah. Ph.D. thesis, California Institute of Technology, Pasadena, 254 p.

Zeng, Y.-F., Metz, P., Satir, M., and Sharp, Z.D., 1994, An experimental calibration of oxygen isotope fractionation between calcite and forsterite in the presence of a CO_2-H_2O fluid: Chemical Geology, v. 116, p. 17-27.

Zhang, X.C., Fredrich, J.M., Nearing, M.A., and Norton, L.D., 2001, Potential use of rare earth oxides as tracers for soil erosion and aggregation studies: Soil Science Society of America Journal, v. 65, p. 1508-1515.